UNIVERSIDAD AUTÓNOMA DE MADRID

FACULTAD DE CIENCIAS

DEPARTAMENTO DE BIOLOGÍA MOLECULAR

Biophysical characterization of a chaperone complex involved in macroautophagy

TESIS DOCTORAL

Marcos Gragera Cabezudo

Madrid, 2019

UNIVERSIDAD AUTÓNOMA DE MADRID

FACULTAD DE CIENCIAS

DEPARTAMENTO DE BIOLOGÍA MOLECULAR

Biophysical characterization of a chaperone complex involved in macroautophagy

Marcos Gragera Cabezudo

Graduado en Biología

Para optar al grado de Doctor en Biociencias Moleculares por la Universidad Autónoma de Madrid

Director:	**Co-directora:**	**Tutor:**
Prof. Jose María Valpuesta Moralejo	**Dr. María del Rosario Fernández Fernández**	**Dr. Ricardo Escalante Hernández**

CENTRO NACIONAL DE BIOTECNOLOGÍA – CSIC

MADRID, 2019

El trabajo presentado en esta memoria ha sido realizado en el Departamento de Estructura de Macromoléculas del Centro Nacional de Biotecnología bajo la dirección del Prof. Jose María Valpuesta Moralejo y la Dra. María del Rosario Fernández Fernández.

Marcos Gragera Cabezudo ha sido beneficiario de una beca de la Fundación La Caixa 2015 concedida por Obra Social la Caixa, dentro del programa de Excelencia Severo Ochoa.

INDEX

ABSTRACT

Eukaryotic cells have developed regulated pathways to maintain a fine balance between protein synthesis, folding, trafficking and degradation (proteostasis). Disruption of this homeostasis network may lead to the onset of pathologies such as cancer or neurodegenerative disorders. Therefore, cells count on several pathways to remove and prevent accumulation and aggregation of potentially toxic proteins, namely the ubiquitin-proteasome system (UPS) and autophagy. Three types of autophagy have been described so far: chaperone-mediated autophagy (CMA), microautophagy and macroautophagy. The chaperone Hsp70 has a central role in all of them. In macroautophagy, Hsp70, in collaboration with other partners (CHIP, Bag3, HspB8), forms a complex that recognizes, ubiquitinates and delivers aggregate-prone proteins towards special locations in cells (aggresomes), for further degradation. This project focuses on the biophysical characterization of the HspB8:Bag3:Hsp70 complex and its components. HspB8, Bag3 and Hsp70 form a stable ternary complex *in vitro*, which we have studied by different biophysical techniques and also by standard electron microscopy (negative staining) and cryoelectron microscopy (cryoEM). Using cryoelectron tomography, we have analyzed the distribution of the ternary complex in the specimen grids, and have found a tendency of the complex not to distribute evenly within the ice layer, but in a single stratum probably the air-water interface. Using single particle analysis, a low-resolution map has been obtained by negative staining, which combined with crosslinking-mass spectrometry data, has allowed us to build a pseudo-atomic model of the ternary complex. Additionally, we have obtained by cryoEM a low-resolution 3D map where only the atomic models of $Hsp70_{SBD}$ and $BAG{:}Hsp70_{NBD}$ could be accommodated. The model supports the previously described bimodal character of the Bag3:Hsp70 interaction.

RESUMEN

Las células eucariotas han desarrollado estrategias para mantener un equilibrio entre síntesis, plegamiento, tráfico y degradación de proteínas, capacidad conocida como proteostasis. La alteración de la proteostasis puede desencadenar en la aparición de patologías como el cáncer o enfermedades neurodegenerativas. Por ello, las células cuentan con varias estrategias para eliminar y prevenir la acumulación de proteínas y agregados potencialmente tóxicos, como son el sistema ubiquitina-proteasoma y la autofagia. Se conocen tres tipos de autofagia: autofagia mediada por chaperonas, microautofagia y macroautofagia. En todas ellas, la chaperona Hsp70 tiene un papel central. En macroautofagia, Hsp70 colabora con otras proteínas (CHIP, Bag3, HspB8) para formar un complejo que reconoce, ubiquitina y transporta proteínas proclives a agregar hacia localizaciones específicas dentro de la célula (agresomas), donde son posteriormente degradadas. Este proyecto se centra en la caracterización biofísica del complejo HspB8:Bag3:Hsp70 y de sus componentes. HspB8, Bag3 y Hsp70 forman un complejo ternario estable *in vitro*, que hemos estudiado utilizando distintas técnicas biofísicas y también mediante microscopía electrónica estándar (tinción negativa) y criomicroscopía electrónica. Hemos analizado por criotomografía electrónica la distribución del complejo en las rejillas de microscopía, y hemos observado una tendencia de este a distribuirse en una única capa, probablemente adherido a la interfaz líquido-aire. Hemos realizado un mapa tridimensional a baja resolución del complejo por tinción negativa que, combinado con datos de espectrometría de masas, nos ha permitido elaborar un modelo pseudoatómico del complejo ternario. Finalmente, hemos obtenido un mapa tridimensional a baja resolución por criomicroscopía electrónica donde solamente podemos alojar los modelos atómicos de $\mathrm{Hsp70_{SBD}}$ y $\mathrm{BAG{:}Hsp70_{NBD}}$ y que apoya el carácter bimodal de la interacción Bag3:Hsp70 descrito previamente.

PRESENTACIÓN

PRESENTACIÓN

Esta tesis doctoral se basa en la caracterización biofísica y estructural de un complejo compuesto por las chaperonas HspB8 y Hsp70, y la co-chaperona Bag3, implicado en la degradación de proteínas por macroautofagia.

Las chaperonas moleculares son proteínas cuya función ha estado tradicionalmente ligada al plegamiento de proteínas. Sin embargo, su implicación en proteostasis se extiende más allá de esta función. Las chaperonas intervienen también en la síntesis, transporte y degradación de proteínas. Las células cuentan con dos vías principales de degradación de proteínas: el sistema ubiquitin-proteasoma y la autofagia. Esta se subdivide en tres tipos: autofagia mediada por chaperonas, microautofagia y macroautofagia. En la macroautofagia, las proteínas objeto de degradación son secuestradas en regiones cercanas al núcleo celular, el agresoma, y encerradas en una vesícula de doble membrana, el autofagosoma. El autofagosoma se fusiona posteriormente con el lisosoma para la degradación de su contenido. El complejo HspB8:Bag3:Hsp70 tiene un papel principal en la detección de proteínas desplegadas o con tendencia a agregar, su ubiquitinación y posterior transporte al agresoma para su degradación por macroautofagia. Entre las proteínas cliente de este complejo están mutantes de la huntingtina, de la superóxido dismutasa, o de la filamina, esencial para mantener la integridad de los sarcómeros en músculo esquelético y otras células sometidas a estrés mecánico (Klimek et al., 2017).

El trabajo se llevó a cabo en el laboratorio del Prof. José María Valpuesta, que cuenta con una larga trayectoria abordando el estudio estructural de chaperonas moleculares mediante microscopía electrónica. Algunos de los trabajos relacionados con chaperonas publicados por este laboratorio incluyen, por ejemplo, a la chaperonina CCT y cómo esta reconoce y asiste en el plegamiento de la actina (Llorca et al., 1999) o de mLST8 (Cuéllar et al., 2019), o los mecanismos mediante los cuales Hsp70 presenta proteínas a CCT para su plegamiento (Cuéllar et al., 2008). Otros trabajos del laboratorio se han centrado en los mecanismos de transferencia de sustrato entre Hsp70 y Hsp90 (Alvira et al., 2014), o en los mecanismos mediante los cuales la co-chaperona CHIP, en colaboración con Hsp70 o Hsp90, ubiquitina proteínas cliente para su degradación por el proteasoma (Quintana-Gallardo et al., 2019). Siguiendo con la implicación de las chaperonas en degradación de proteínas, comenzamos este proyecto, cuyo objetivo era la caracterización biofísica y estructural del complejo HspB8:Bag3:Hsp70. Dado el interés biológico de las chaperonas moleculares, el conocimiento de su mecanismo de acción a nivel estructural es esencial para entender y modular su función.

Al comienzo de esta tesis doctoral, solo una de las tres proteínas, Hsp70, estaba disponible en el laboratorio. Amplificamos las secuencias codificantes para las proteínas HspB8 y Bag3 a partir de librerías de cDNA de origen humano. Generamos el DNA recombinante que codifica para la secuencia de las proteínas de interés con una secuencia de histidinas en el extremo N-terminal para su purificación por cromatografía de afinidad.

Dada la importancia del grado de pureza del espécimen para su estudio estructural por microscopía electrónica, dedicamos una parte considerable del proyecto a la optimización de los protocolos de purificación de las tres proteínas. Cuando éstas fueron obtenidas rutinariamente con el grado de pureza deseado, dimos paso a su caracterización estructural, tanto individualmente como a nivel de los distintos complejos que se pueden formar. La formación del complejo ternario HspB8:Bag3:Hsp70, así como los binarios HspB8:Bag3 y Bag3:Hsp70 se estudió y verificó mediante cromatografía de exclusión molecular y ultracentrifugación analítica.

De manera complementaria, caracterizamos con más detalle la interacción entre HspB8 y Bag3. Nuestros resultados apoyan que la interacción sigue una estequiometría de 2 moléculas de HspB8 por cada molécula de Bag3, y que la interacción conlleva la adquisición de estructura secundaria de tipo β. Estudiamos también la dimerización de HspB8 por cromatografía de exclusión molecular y centrifugación analítica, y concluimos que HspB8 se encuentra fundamentalmente como monómero en solución, y que los dímeros comienzan a aparecen a concentraciones superiores a 9 μM.

Seguidamente a la caracterización biofísica del complejo, procedimos a su estudio estructural por criomicroscopía electrónica. Previamente, obtuvimos una reconstrucción tridimensional del complejo a baja resolución por tinción negativa. La obtención de muestras vitrificadas donde el complejo se muestre estable es uno de los principales cuellos de botella dentro de la criomicroscopía electrónica. Se probaron numerosos tipos de rejilla, tratamientos, condiciones de vitrificación y formas de estabilizar el complejo, y nos apoyamos en la criotomografía electrónica para extraer conclusiones acerca del comportamiento de la muestra en rejillas vitrificadas. Finalmente, obtuvimos varias rejillas de las que se adquirieron datos para la reconstrucción tridimensional del complejo.

Combinando los mapas a baja resolución obtenidos por tinción negativa con datos de espectrometría de masas, generamos un modelo pseudoatómico a partir de los modelos atómicos publicados de algunos componentes del complejo.

El trabajo desarrollado durante esta tesis nos ha permitido obtener información estructural relevante del complejo HspB8:Bag3:Hsp70 y entender el comportamiento de complejos que contienen Hsp70 en criomicroscopía, lo que contribuirá a trabajos futuros que se hagan con otros complejos que contengan Hsp70.

LIST OF ABBREVIATIONS

LIST OF ABBREVIATIONS

2D: Two-dimension(al)

3D: Three-dimension(al)

ACD: α-crystallin central domain

AD: Alzheimer's disease

ADA: N-(2-acetamido)iminodiacetic acid

ADP: Adenosine diphosphate

AIM: Auto-induction medium

ALS: Amyotrophic lateral sclerosis

ATP: Adenosine triphosphate

AUC: Analytical ultracentrifugation

AWI: Air-water interface

BAG: Bcl-2-associated athanogene

β-ME: β-mercaptoethanol

BS3: Bis(sulfosuccinimidyl)suberate

CAEMI: Chaperone-assisted endosomal microautophagy

CAMA: Chaperone-assisted macroautophagy

CCD: Charge-coupled device

CFTR: Cystic fibrosis transmembrane conductance regulator

CHAPS: 3-((3-cholamidopropyl) dimethylammonio)-1-propanesulfonate

CHAPSO: 3-([3-Cholamidopropyl]dimethylammonio)-2-hydroxy-1-propanesulfonate

CHIP: Carboxy terminus of Hsp70-interacting protein

CID: Collision-induced dissociation

(Cm^R): Chloramphenicol resistance

CMA: Chaperone-mediated autophagy

CMC: Critical micelle concentration

cryoEM: Cryoelectron microscopy

cryoET: Cryoelectron tomography

CTD: C-terminal domain

CTF: Contrast transfer function

CUPS: Chaperone-assisted ubiquitin-proteasome system

CV: Column volume

DCM: Dilated cardiomyopathy

DDM: Dodecyl β-D-maltoside

DED: Direct electron detector

dHMN: Distal hereditary motor neuropathy

DQE: Detective quantum efficiency

DRiP: Defective ribosomal products

DTT: Dithiothreitol

EDTA: Ethylenediaminetetraacetic acid

EEO: Electroendosmosis

EThcD: Electron-Transfer/Higher-Energy Collision Dissociation

FSC: Fourier shell correlation

FT: Flow-through

FTD: Frontotemporal dementia

FUS: Fused in sarcoma

GO: Graphene oxide

HCD: Higher-energy collisional dissociation

HD: Huntington’s disease

HEPES: 4-(2-hydroxyethyl)-1-piperazineethanesulfonic acid

Hsp-: Heat shock protein

IDP: Intrinsically disordered protein

IEX: Ion exchange chromatography

IMAC: Immobilized metal ion affinity chromatography

IPTG: Isopropyl 1-thio-β-D-galactopyranoside

ITC: Isothermal titration calorimetry

LAMP2A: Lysosome-associated membrane glycoprotein 2

LB: Luria-Bertani medium

LMNG: Lauryl maltose neopentyl glycol

MFM: Myofibrillar myopathy

MS: Mass spectrometry

MW: Molecular weight

MW_W: Weight-average molecular weight

NBD: Nucleotide binding domain

NEF: Nucleotide exchange factor

NMR: Nuclear magnetic resonance

NTD: N-terminal domain

O.D.$_{600}$: Optical density at 600 nm

OG: Octyl α-D-glucopyranoside

o/n: Overnight

OPMD: Oculopharyngeal muscular dystrophy

PCD: Protein conformational disorders

PD: Parkinson’s disease

PDB: Protein Data Bank

PMSF: Phenylmethylsulfonyl fluoride

PXXP: Proline-rich repeat

RBP: RNA-binding proteins

rpm: Revolutions per minute

RT: Room temperature

SBD: Substrate binding domain

SBMA: Spinal bulbar muscular atrophy

SDS-PAGE: Sodium dodecylsulfate polyacrylamide gel electrophoresis

SE-AUC: Sedimentation equilibrium analytical ultracentrifugation

SEC: Size exclusion chromatography

SG: Stress granule

SGD: Stochastic gradient descent

sHsp: Small heat shock protein

SOD: Superoxide dismutase

SPA: Single particle analysis

SPG: Succinic acid, sodium phosphate monobasic monohydrate, glycine

SV-AUC: Sedimentation velocity analytical ultracentrifugation

TCEP: Tris(2-carboxyethyl)phosphine

TEV: Tobacco Etch Virus

Ubl: Ubiquitin-like domain

UPS: Ubiquitin-proteasome system

WB: Western blot

XL-MS: Crosslinking coupled to mass spectrometry

LIST OF BUFFERS

LIST OF BUFFERS

DNA Loading Buffer

10 mM Tris-HCl pH 7.6, 60 mM EDTA, 60% (v/v) glycerol, 0.03% bromophenol blue, 0.03% xylene cyanol FF.

TAE Buffer

40 mM Tris-HCl pH 7.6, 20 mM acetic acid, 1 mM EDTA.

Blue-Native loading buffer

40 mM Tris-HCl pH7, 4% glycerol (v/v), 0.01% bromophenol blue, 0.5% brilliant blue G-250.

Buffer A IMAC-Hsp70

20 mM HEPES pH 7.4, 500 mM KCl, 20 mM imidazole, 1 mM DTT, 1 mM PMSF, 15% glycerol.

Buffer B IMAC-Hsp70

20 mM HEPES pH 7.4, 500 mM KCl, 500 mM imidazole, 1 mM DTT, 1 mM PMSF, 15% glycerol.

Buffer A IEX-Hsp70

5 mM imidazole pH 6.5, 1 mM EDTA, 5% glycerol, 1 mM DTT, 1 mM PMSF.

Buffer B IEX-Hsp70

5 mM imidazole pH 6.5, 1 mM EDTA, 500 mM NaCl, 5% glycerol, 1 mM DTT, 1 mM PMSF.

Buffer SEC-Hsp70

20 mM HEPES pH 7.4, 100 mM KCl, 5 mM $MgCl_2$, 0.1 mM DTT, 5% glycerol.

Buffer A IMAC-Bag3

100 mM sodium phosphate buffer pH 7.4, 500 mM NaCl, 20 mM imidazole, 10% glycerol, 1 mM DTT, 1 mM PMSF.

Buffer B IMAC-Bag3

100 mM sodium phosphate buffer pH 7.4, 500 mM NaCl, 500 mM imidazole, 10% glycerol, 1 mM DTT, 1 mM PMSF.

Buffer A IEX-Bag3

20 mM HEPES 7.4, 20 mM NaCl, 10% glycerol, 1 mM DTT, 1 mM PMSF.

Buffer B IEX-Bag3

20 mM HEPES 7.4, 1 M NaCl, 10% glycerol, 1 mM DTT, 1 mM PMSF.

Buffer A IMAC-HspB8

100 mM sodium phosphate buffer pH 7.4, 500 mM NaCl, 20 mM imidazole, 10 mM β-mercaptoethanol, 1 mM PMSF.

Buffer B IMAC-HspB8

100 mM sodium phosphate buffer pH 7.4, 500 mM NaCl, 250 mM imidazole, 10 mM β-mercaptoethanol, 1 mM PMSF.

Buffer A IEX-HspB8

10 mM imidazole pH 6.5, 20 mM NaCl, 10 mM β-mercaptoethanol, 1 mM PMSF.

Buffer A IMAC-TEV

50 mM sodium phosphate buffer pH 8.0, 500 mM NaCl, 20 mM imidazole, 10% glycerol (v/v), 1 mM DTT.

Buffer B IMAC-TEV

50 mM sodium phosphate buffer pH 8.0 500 mM NaCl, 500 mM imidazole, 10% glycerol (v/v), 1 mM DTT.

Buffer B IEX-HspB8

10 mM imidazole pH 6.5, 1 M NaCl, 10 mM β-mercaptoethanol, 1 mM PMSF.

Buffer SEC-HspB8

20 mM HEPES pH 7.4, 100 mM KCl, 5 mM $MgCl_2$, 2.5 mM DTT, 5% glycerol.

Buffer Complex

20 mM HEPES pH 7.4, 100 mM KCl, 5 mM $MgCl_2$, 0.1 mM DTT.

Top buffer

20 mM HEPES pH 7.4, 100 mM KCl, 5 mM $MgCl_2$, 0.1 mM DTT, 10% sucrose.

Bottom buffer

20 mM HEPES pH 7.4, 100 mM KCl, 5 mM $MgCl_2$, 0.1 mM DTT, 25% sucrose, 0.15% glutaraldehyde.

Native running buffer

25 mM Tris pH 8.3, 200 mM glycine.

SDS-PAGE Loading buffer

50 mM Tris-HCl pH 7.6, 0.2 mM EDTA, 2% SDS (w/v), 25% glycerol, 0.01% bromophenol blue (w/v) and 5% (v/v) β-mercaptoethanol.

SDS-Running buffer

25 mM Tris pH 8.3, 200 mM glycine, SDS 0.01% (w/v).

Buffer CD

20 mM potassium phosphate 7.4, 100 mM KF, 1 mM $MgCl_2$, 0.25 mM TCEP.

Fixation solution

40% ethanol, 10% acetic acid.

Thiosulfate solution

0.02% (w/v) $Na_2S_2O_3$-$5H_2O$.

Staining solution

0.25% (w/v) $AgNO_3$, 0.033% (v/v) formaldehyde.

Developing solution

2% (v/v) Thiosulfate solution, 6% (w/v) Na_2CO_3, 0.037% (v/v) formaldehyde.

INTRODUCTION

INTRODUCTION

The relevance of proteostasis for cell survival

Cellular homeostasis is the capacity of maintaining a functional state upon influences from either internal or external sources. Given the variety of functions performed by proteins, proteostasis, or the preservation of protein homeostasis, is essential for cell function and survival. This balance is supported by a protein quality control system that comprises an intricate network of proteins (800 proteins in human cells), including around 200 molecular chaperones and their regulators. Together, they assist protein folding and trafficking, and coordinate protein degradation to remove irreversibly misfolded or damaged proteins, granting adaptability in response to changes in the cellular environment (Hartl et al., 2011) **(Figure 1)**. The proteostasis network is sustained by signaling pathways that control the concentration, distribution and activity of the components, by operating at the transcriptional, translational and posttranslational levels (Powers et al., 2009).

Deficiencies in the proteostasis network are linked to the onset of pathologies, normally associated to aberrant protein folding and referred to as protein conformational disorders (PCD) (Carrell & Lomas, 1997). Examples of PCD are cystic fibrosis caused by the CFTR F508Δ mutant, where the defective misfolded protein fails at trafficking to the plasma membrane (Dechecchi et al., 2018). In other cases, affected proteins tend to form aggregates as those found in neurodegenerative conditions like Parkinson’s disease (PD), Alzheimer’s disease (AD), Huntington’s disease (HD) or amyotrophic lateral sclerosis (ALS) (Ciechanover & Kwon, 2015; Hartl et al., 2011). Therefore, maintaining an efficient degradation system is essential to remove aberrant proteins and to grant a normal cell function.

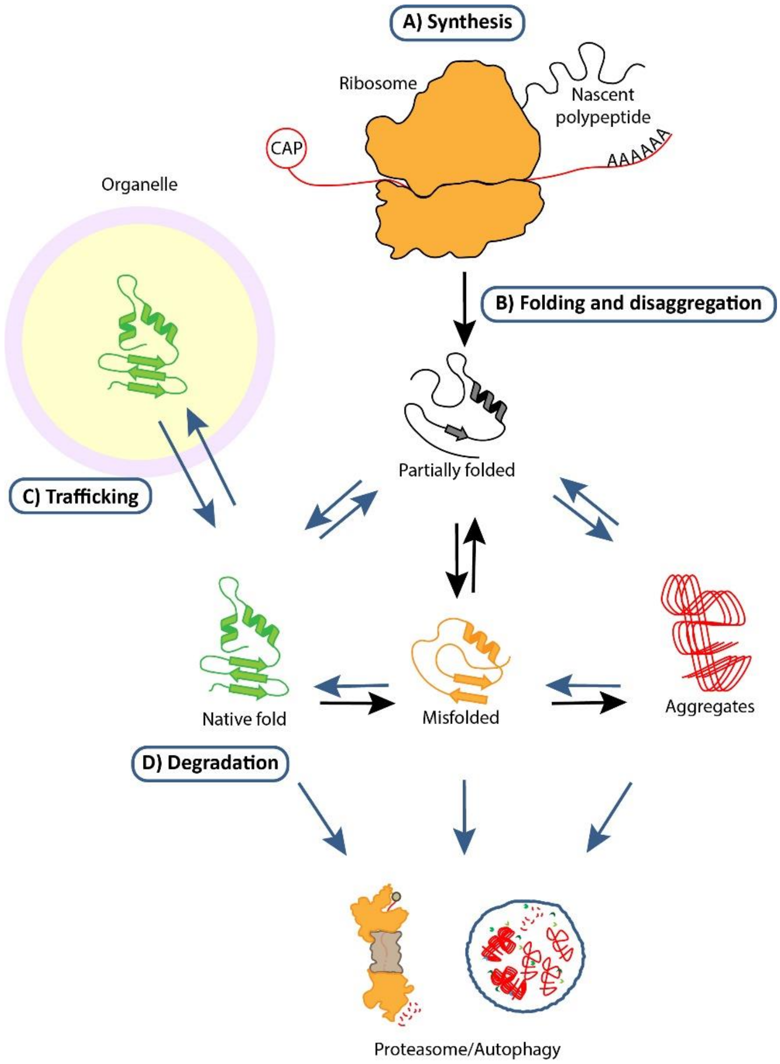

Figure 1. Role of molecular chaperones in proteostasis. *Proteostasis comprises protein synthesis* ***(A)****, folding and disaggregation* ***(B)****, trafficking* ***(C)*** *and degradation* ***(D)****. Molecular chaperones assist client proteins through all these stages. Blue arrows indicate processes in which chaperones are involved. Small polypeptides can fold properly by themselves. However, multidomain proteins often require the assistance of molecular chaperones to attain their native conformation and/or to deliver them to their final location in the cell. Mutations or cell stress might induce proteins to misfold or aggregate. In certain cases, chaperones can reverse these potentially toxic proteins to their native state. Finally, damaged, misfolded or irreversibly aggregated proteins are targeted to degradation pathways, through either the proteasome or the autophagy pathways.*

Protein degradation strategies in eukaryotic cells: the ubiquitin-proteasome system and autophagy

Eukaryotic cells count on several mechanisms for protein degradation. The major pathway for protein degradation is the ubiquitin-proteasome system (UPS). Ubiquitins are small proteins that covalently bind to other proteins, acting as a hallmark for protein degradation. The proteasome is a multiprotein assembly of approximately 2 MDa composed of a barrel-shape central core (named as 20S because of its sedimentation coefficient) with two 19S regulatory caps at both ends. The 20S core is a hollow cavity that bears protease activity. UPS client proteins are tagged with ubiquitins and targeted to the proteasome cavity, where they are finally degraded (Arndt et al., 2007). Autophagy is an alternative and often, complementary degradation pathway in eukaryotic cells. It was first described in glucagon-treated rat hepatocytes as cytoplasmic granules containing organelles and acid hydrolases (Ashford & Porter, 1962; de Duve et al., 1955). Three types of autophagy have been described so far: chaperone-mediated autophagy (CMA), microautophagy and macroautophagy.

CMA is activated during starvation, oxidative stress and other conditions that promote protein damage (Kaushik & Cuervo, 2012a). It involves the recognition of the cytosolic client protein by chaperones and its internalization inside the lysosome by the action of a transmembrane translocation complex. This complex contains the lysosome-associated membrane protein 2A (LAMP2A). However, the exact composition of the translocation complex, as well as the proteins collaborating in this process, are still poorly understood (Agarraberes & Dice, 2001).

Microautophagy involves the engulfment of cytosolic client proteins by invagination of either the lysosomal or endosomal membrane directly, with subsequent degradation (Marzella et al., 1981). Most microautophagy studies have been performed in yeast, whereas mammalian microautophagy is poorly understood (Kunzt et al., 2004).

Macroautophagy is conserved from yeast to humans. The cytosolic material is initially engulfed in a double membrane vesicle, the autophagosome. Then, the autophagosome fuses with a lysosome for cargo degradation by lysosomal hydrolases. The cargoes degraded through macroautophagy include organelles like mitochondria (mitophagy), ribosomes (ribophagy), bacteria and viruses (xenophagy) or aggregated proteins (aggrephagy) (Kaushik & Cuervo, 2012b).

The role of the molecular chaperone Hsp70 in protein degradation

Molecular chaperones are essential to keep other proteins in a functional state, preventing them from misfolding and aggregation when they face changes in the cellular environment (physical, metabolic, environmental stress) (Hartl et al., 2011). There are a large number of chaperones, many of them belonging to the following families: the small heat shock proteins (sHsp), Hsp40, Hsp60, Hsp70, Hsp90, Hsp100 and Hsp110. Their function in protein folding, assembly, trafficking and disaggregation has been widely studied (Doyle et al., 2013; Frydman, 2001).

The role of chaperones in protein degradation has attracted considerable attention over the last years (Kettern et al., 2010). Chaperones participate in degradation by interacting with components of the degradation systems, UPS and autophagy, for the disposal of non-native proteins to facilitate their degradation (Arndt et al., 2007, 2010; Carra et al., 2008a; Gamerdinger et al., 2009).

The Hsp70 family of chaperones has a special relevance in proteostasis because it participates in protein folding, disaggregation, trafficking and degradation, always assisted by other chaperones and co-chaperones. The latter can be defined as non-client proteins that interact with chaperones and regulate their activity (McCollum et al., 2010). The Hsp70 family includes 13 isoforms in the human proteome (Kampinga et al., 2009). Some of them are expressed constitutively (HspA5, HspA8, HspA9, generally known as Hsc70), whereas others are inducible upon cell stress (HspA1A/B). Most of the structural insights come from the study of HspA1A and HspA8, and the prokaryotic orthologue DnaK (Bertelsen et al., 2009; Fernández-Fernández et al., 2017).

The domain organization of Hsp70 consists of an N-terminal, nucleotide binding domain (Hsp70$_{NBD}$, 45 kDa) with ATPase activity, and a substrate-binding domain (Hsp70$_{SBD}$, 25 kDa) in the C-terminus, both connected by a flexible linker **(Figure 2.A)**. Hsp70$_{NBD}$ is composed of two lobes, named I and II, which in turn subdivide in Ia, Ib, IIa and IIb. The lobes form a V-shaped structure that hosts the ATPase activity. ATP molecules bind to the Hsp70$_{NBD}$ cleft, and the hydrolysis induces conformational changes in the SBD transmitted through the linker (Stricher et al., 2013). Hsp70$_{SBD}$ is divided in two subdomains, a β-sheet domain (SBDβ, 15kDa) and a α-helical or lid domain (SBDα, 10 kDa). The C-terminus contains the sequence EEVD, essential for the binding of the co-chaperone CHIP (Alvira et al., 2014; Zhang et al., 2015).

Hsp70 cycles between two functional states. In the ATP-bound state, Hsp70$_{SBD}$ adopts an open conformation, showing low affinity for its client proteins. In the ADP-bound state, Hsp70$_{SBD}$ changes to a close conformation, with high affinity for the client protein. The hydrolysis of ATP is promoted by the Hsp40 chaperones, which contain the Hsp70-interacting J-domain, while the nucleotide exchange factors like those of the Bag family, act as co-chaperones that induce the exchange of ADP for ATP (Bertelsen et al., 2009; Kityk et al., 2018, 2012; Qi et al., 2013; Zuiderweg et al., 2017) **(Figure 2.B)**.

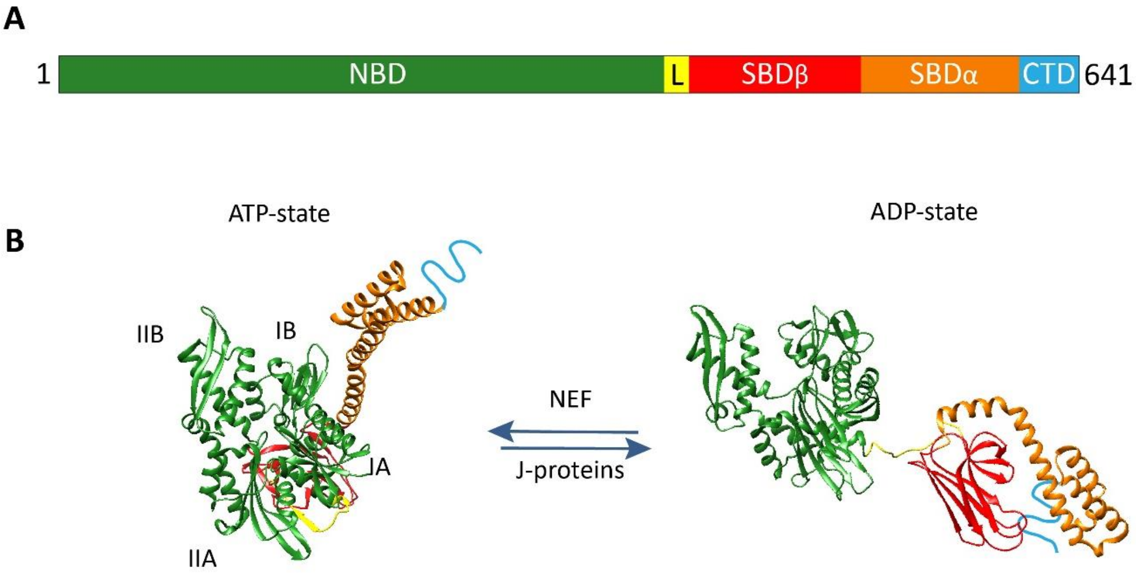

Figure 2. Domain organization of Hsp70 and conformational states. *(**A)** Domain scheme of Hsp70 isoform 1B (Human gen ID: 3304). **(B)** Atomic structure of Hsp70 in the close (PDB: 2KHO) and open (PDB: 4JNE) conformation, triggered upon nucleotide binding. Domains depicted with the same color code as in (A). L: linker; CTD: C-terminal domain. Adapted from (Fernández-Fernández & Valpuesta, 2018).*

Hsp70 is able to recognize a sequence present every 30-40 residues on average in its client proteins. This short motif consists of five hydrophobic amino acids flanked by two positively charged residues, and its exposure to the solvent is usually indicative of protein misfolding (Rüdiger et al., 1997). Hsp70 folds client proteins either alone or in collaboration with downstream chaperones like Hsp90 (Morán Luengo et al., 2018; Wegele et al., 2004). In bacteria, plants, fungi and metazoans, Hsp70 collaborates with the disaggregase Hsp100 to untangle protein aggregates in concert with Hsp40 and sHsp (Glover & Lindquist, 1998) (Glover & Lindquist, 1998; Mogk et al., 2018; Rosenzweig et al., 2013).

Other functions attributed to Hsp70 include the regulation of the assembly and disassembly of macromolecular complexes like clathrin (Sousa & Lafer, 2015), regulation of the activity of natively folded proteins in concert with other chaperones (Röhl et al., 2015) or assisting the cross-membrane trafficking in mitochondria and endoplasmic reticulum (Craig, 2018).

Concerning degradation, Hsp70, either in its constitutive or inducible isoforms, is involved in all the degradation pathways, trapping and targeting the client protein in collaboration with other chaperones and co-chaperones (Fernández-Fernández & Valpuesta, 2018). In chaperone-assisted UPS (CUPS), Hsp70 binds a client protein unable to attain a native conformation. Then, the ubiquitin ligase E3 CHIP binds to the C-terminal EEVD of Hsp70 with a double function. On the one hand, CHIP interaction inhibits Hsp70 folding activity (Ballinger et al., 1999) and, on the other hand, positions the bound client near the ubiquitin-conjugating enzyme E2 (Connell et al., 2001) to facilitate ubiquitination. The co-chaperone Bag1 interacts with $Hsp70_{NBD}$ and docks the complex to the proteasome through its ubiquitin-like (Ubl) domain (Arndt et al., 2007). The ubiquitinated client enters the proteasome and undergoes degradation **(Figure 3)**.

Hsp70 also participates in the three types of autophagy. The already described CMA specifically involves the constitutive Hsc70 isoform, which recognizes the KFERQ motif in the client protein and interacts with LAMP2A (Chiang et al., 1989; Rout et al., 2014). The client protein also binds to the cytosolic region of LAMP2A. Upon client binding, a CMA translocation complex of nearly 700 kDa is formed (Bandyopadhyay et al., 2008). Hsc70 forms complexes with other chaperones (Hsp90, Hsp40) and co-chaperones (Bag1, Hop, Hip) at the cytosolic side of the lysosomal membrane, but their exact role in CMA remains to be determined (Agarraberes & Dice, 2001). The translocation of the client protein inside the lysosome seems to require the presence of an intralysosomal Hsc70 (Lys-Hsc70) that pulls the client to the lumen for further degradation (Agarraberes et al., 1997).

Microautophagy, and a specific subtype of it involving late endosomes termed CAEMI (chaperone-assisted endosomal microautophagy), seem to rely also on Hsc70 (Fernández-Fernández et al., 2017; Horst et al., 1999). Hsc70 bends the endosomal membrane based on its ability to oligomerize, and interacts with acidic phospholipids through a cluster of positively charged residues in the lid domain (Morozova et al., 2016; Uytterhoeven et al., 2015). Client proteins, which also bear the KFERQ motif, are previously unfolded in order to be degraded by this pathway (Sahu et al., 2011). It is still unknown what determines whether a client protein is targeted to CMA or CAEMI.

A degradation pathway that relates macroautophagy and Hsp70 has been described (Arndt et al., 2010). In this process, Hsp70 forms a complex with the small heat shock protein HspB8 and the co-chaperones Bag3 and CHIP that recognizes and ubiquitinates misfolded or aggregated proteins and targets them to the autophagosome for degradation (Gamerdinger et al., 2011a). This degradation pathway has been termed chaperone-assisted macroautophagy (CAMA) (Fernández-Fernández et al., 2017) **(Figure 3)**.

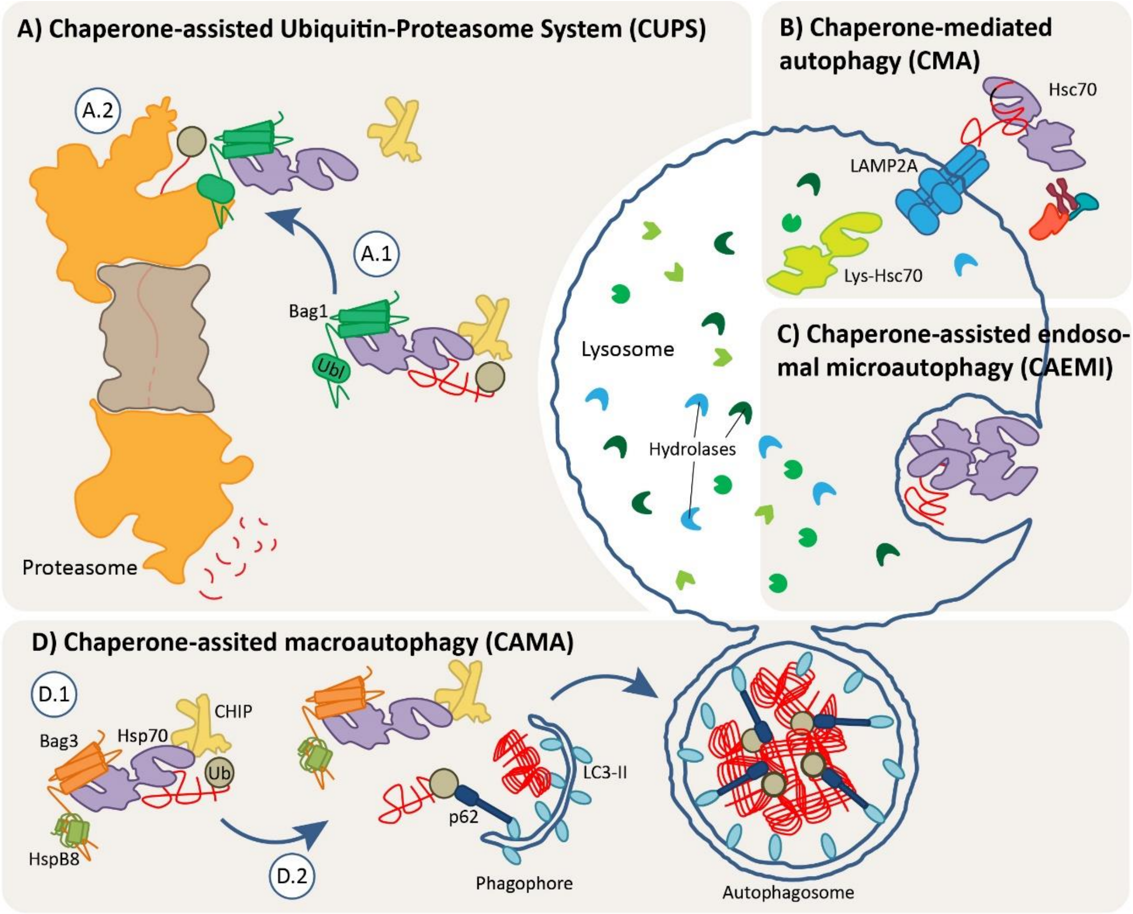

Figure 3. Molecular chaperones in the different degradation pathways. (A) *A complex formed by Hsp70, CHIP and Bag1 binds to the client protein and ubiquitinates it (A.1). The client protein is targeted to the proteasome for degradation (A.2).* ***(B)*** *CMA involves the transport of the misfolded client inside the lysosome through a translocation complex that includes LAMP2A.* ***(C)*** *In microautophagy, Hsc70-bound client proteins are directly engulfed by the lysosomal membrane.* ***(D)*** *In CAMA, the client protein is targeted for degradation by a multichaperone complex (D.1) towards a perinuclear region where misfolded and aggregated proteins are sequestered, the aggresome. A double membrane vesicle, the phagophore, envelops the aggresome to form the autophagosome. The autophagosome will then fuse with the lysosome for the degradation by hydrolases. Ub: Ubiquitin; Ubl: Bag1 ubiquitin-like domain; Lys-Hsc70: Lysosomal Hsc70.*

The versatility of Hsp70 is therefore explained by its ability to interact with a wide set of partners. Consequently, a role for Hsp70 as a multiple socket in proteostasis has been proposed, where the fate of a given client (folding, disaggregation, degradation) will depend on the interplay of chaperones and co-chaperones that interact with Hsp70 (Fernández-Fernández et al., 2017; Fernández-Fernández & Valpuesta, 2018; Zhang & Qian, 2011) **(Figure 4)**.

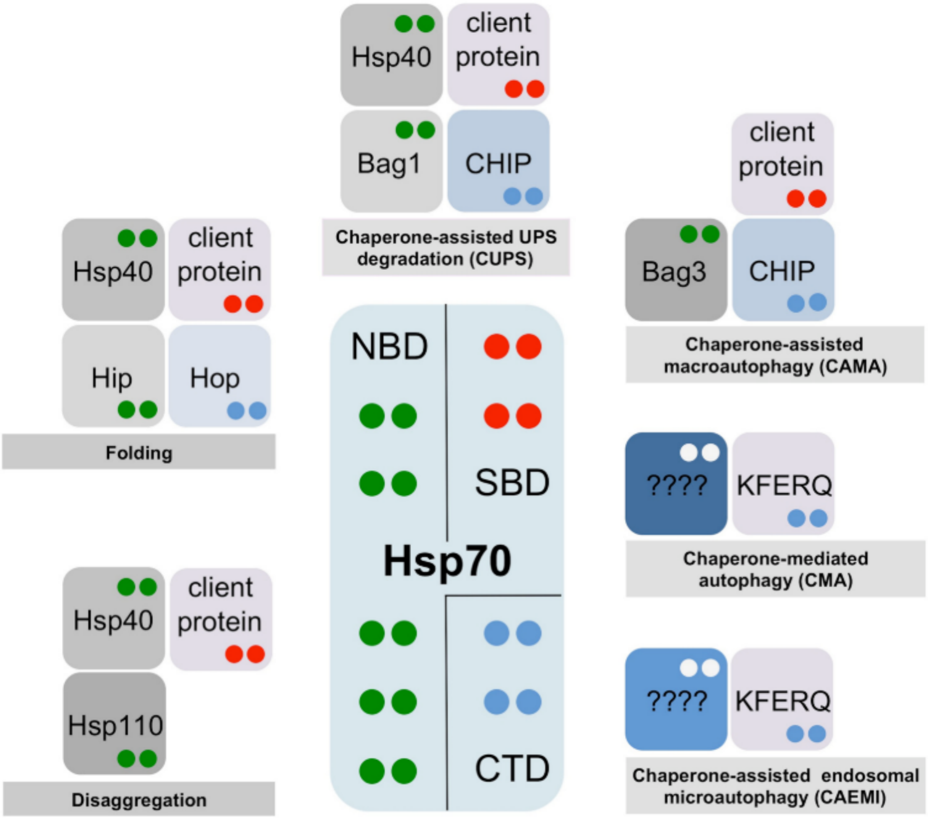

Figure 4. "Multiple socket" model for Hsp70 proteins. *Hsp70 provides a physical platform for the binding of client proteins and other chaperones and co-chaperones. The combination of binding partners will determine the fate of the client protein. The colored dots in interacting partners indicate their binding site to Hsp70. Green: NBD; red: SBD; blue: CTD. Taken from (Fernández-Fernández & Valpuesta, 2018).*

The HspB8:Bag3:Hsp70 complex in proteostasis

Macroautophagy was initially considered as a nonspecific bulk degradation of cytoplasm triggered upon starvation. However, since the discovery of autophagy receptors (p62/SQSTM1, NBR1, FYCO1, OPTN, among others), it has become clear that macroautophagy is also a specific process (Johansen & Lamark, 2011). Autophagy receptors link client proteins to autophagosome-membrane proteins, like LC3 **(Figure 3.D)**. Moreover, they polymerize to sequester their cargo, often ubiquitinated, in discrete regions of the cytoplasm. The list of cargoes degraded by selective macroautophagy include organelles like mitochondria, ribosomes, bacteria, viruses or aggregated proteins, and specific autophagy receptors have been identified for some of them (Feng et al., 2014; Shaid et al., 2013). Aggregopathies, such as HD, PD, AD and oculopharyngeal muscular dystrophy (OPMD) are characterized by the accumulation of misfolded proteins in aggregates. Therefore, aggrephagy, or selective degradation of aggregates through macroautophagy, has attracted the attention because of its implication in human disease (Ciechanover & Kwon, 2015). As introduced above, the heteromeric complex containing HspB8, Bag3 and Hsp70 has been found to have a pivotal role in the degradation of aggregates and misfolded proteins through macroautophagy, also known as CAMA.

Domain organization of HspB8

HspB8 is a member of the small heat shock proteins family, a group of ubiquitous chaperones present in all domains of life, with ten members (HspB1-10) in mammals (Kampinga et al., 2009). They prevent aggregation by binding to and stabilizing early unfolding intermediates in a ATP-independent manner, but they do not recover unfolded or aggregated client proteins (Mchaourab et al., 2002). HspB8 is mainly expressed in skeletal and smooth muscle, heart, brain and spinal cord, especially in motor and sensory neurons (Shemetov et al., 2008b).

HspB8 is a 22 kDa protein containing a central and highly conserved α-crystallin domain (ACD), flanked by N- and C- terminal domains (NTD and CTD, respectively), whose sequences differ among the members of the family **(Figure 5.A)**. The ACD consists of a β-sandwich of two antiparallel sheets of three and four β-strands, both connected by a short loop. Strands β4 and β8 in HspB8 contain hydrophobic amino acids that form a hydrophobic groove at one end of the ACD **(Figure 5.C)**. This groove is the binding site for Bag3 (Fuchs et al., 2010). The ACD mediates dimerization, which is the basic building block in HspB8, whereas NTD and CTD are involved in client recognition, together with part of the ACD (Haslbeck & Vierling, 2015).

The variability in the NTD and CTD confers the diversity in quaternary structure that sHsp can adopt, giving rise to oligomeric assemblies of different sizes (12 to 48-mers) and shapes (barrels, spheres, rings) (Delbecq & Klevit, 2013; Fernández-Fernández et al., 2016; Haslbeck & Vierling, 2015). The CTD usually contains a conserved motif, IXI/V (Ile-X-Ile/Val), where X is typically a proline residue (Caspers et al., 1995), responsible for high-oligomeric states. Since HspB8 lacks this triad (located in the missing β10 strand), it is mainly found in low-oligomeric states (Carra et al., 2008b), although it can form heteroligomers with other sHsp (Arrigo & Gibert, 2013; Fontaine et al., 2005; Sun et al., 2004). Interestingly, the hydrophobic groove of HspB8 interacts with two IPV motifs present in Bag3 (Fuchs et al., 2010).

The structure, chaperone activity and oligomeric state of HspB8 can be regulated by phosphorylation (Shemetov et al., 2008a, 2011). There are reports showing a certain degree of autophosphorylation activity, but it is controversial whether HspB8 is able to phosphorylate other proteins, as initially described (Kappé et al., 2001; Kim et al., 2004; Shemetov et al., 2008b).

Domain organization and function of Bag3

Bag3 is constitutively expressed in several tissues, with high levels in heart and skeletal muscle, brain and peripheral nervous system (Behl, 2016). In mammals, the Bag family is constituted by six members (Bag1-6). They share the C-terminal BAG domain, whose sequence is conserved not only among the family members, but also throughout the different kingdoms (Kabbage & Dickman, 2008; Rosati et al., 2011). The BAG domain consists of a bundle of 3 antiparallel α-helices of variable lengths across the majority of family members (Behl, 2016; Xu et al., 2008). The BAG domain interacts with $Hsp70_{NBD}$ to increase the nucleotide exchange rate (Brehmer et al., 2001; Sondermann et al., 2001) **(Figure 5.D)**. For this reason, Bag proteins form part of the family of NEF (nucleotide exchange factors). This activity regulates the affinity of Hsp70 for their client proteins by changing from ADP-bound (high affinity) to ATP-bound state (low affinity). Bag3 interacts with Hsp70 in a 1:1 ratio, with a K_d of 2-3 nM. The affinity is dependent on the nucleotide state, being highest in the apo-state, followed by ATP- and ADP-bound states.

The interaction of HspB8 and Bag3 has also been studied *in vitro*. They form a stable complex with a K_d of around 1 µM and a 2:1 stoichiometry (Rauch et al., 2016a). Other reports have suggested that the stoichiometry could vary from 1:1 to 4:1, depending on the relative concentration of HspB8 and Bag3 (Shemetov & Gusev, 2011).

Apart from the C-terminal BAG domain, Bag3 contains a PXXP (proline-rich repeat) region, two IPV (isoleucine-proline-valine) motifs that mediate interaction with HspB8 and HspB6 (Fuchs et al., 2010), a WW domain and two RSQS motifs for protein-protein interactions (Xu et al., 2013) **(Figure 5.B)**.

The modular composition of Bag3 allows a wide range of protein-protein interactions that make Bag3 to participate in numerous signaling pathways, in addition to macroautophagy (Behl, 2016; Chen et al., 2013b).

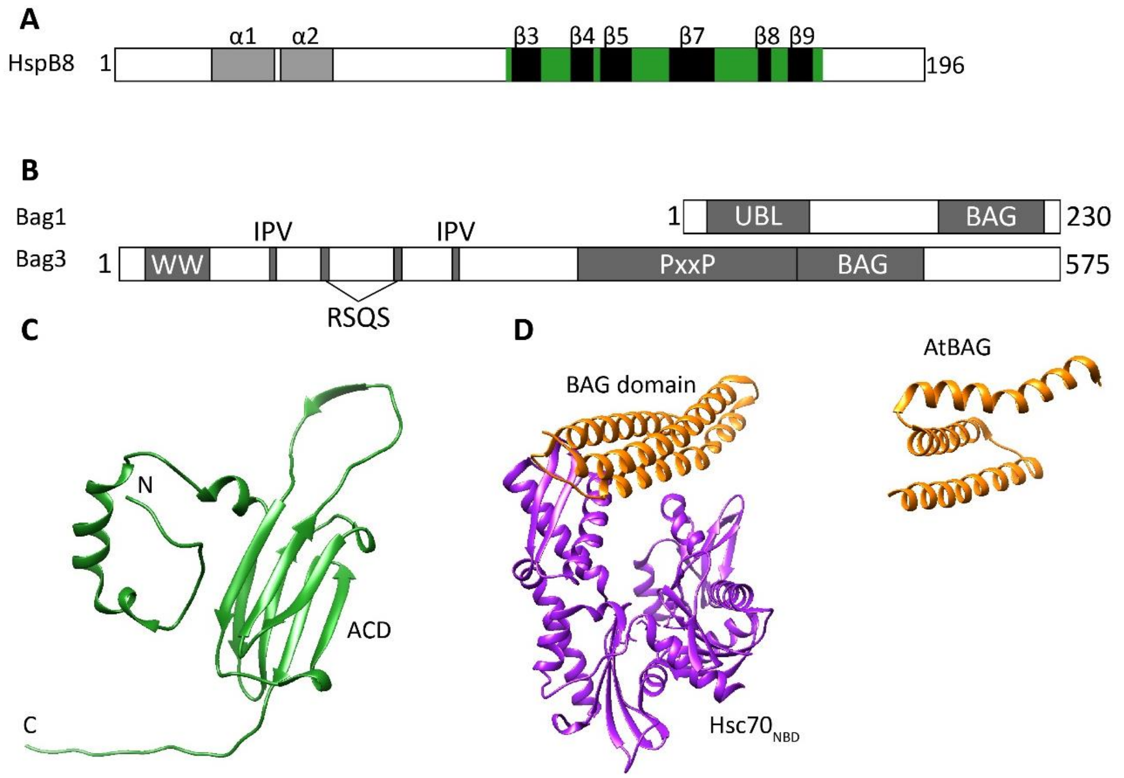

Figure 5. Structural comparison of HspB8 and Bag3. (A) *Diagram of the secondary structure features of HspB8. In green, the ACD.* ***(B)*** *Comparison of the domain composition of Bag1 and Bag3.* ***(C)*** *Crystal structure of a monomer of Triticum aestivum Hsp16.9 small heat shock protein (PDB: 1GME), where the N- and C- termini and ACD are indicated.* ***(D)*** *Crystal structure of Bag1 BAG domain bound to Hsc70*$_{NBD}$ *(1HX1) (left) and Bag3 BAG domain from Arabidopsis thaliana (4HWF) (right).*

The HpsB8:Bag3:Hsp70 complex in chaperone-assisted macroautophagy (CAMA)

Cells expressing model proteins with polyglutamine and polyalanine expansions, prone to aggregation, accumulated aggregates when treated with autophagy inhibitors at different stages of the pathway, whereas rapamycin, an autophagy stimulator, reduced the incidence of these aggregates and cell death (Ravikumar et al., 2002). HspB8 was found to block aggregation, maintaining polyglutamine proteins in a soluble state for rapid degradation (Carra et al., 2005).

This conclusion is in agreement with previous studies that described an anti-aggregation activity of HspB8 *in vitro* (Kim et al., 2004). HspB8 activity *in vivo* depends on its interaction with Bag3, and together they stimulate aggregate degradation through macroautophagy. Indeed, the levels of LC3-II, a macroautophagy marker, increase upon overexpression of HspB8 and Bag3 (Carra et al., 2008a).

A complex containing HspB8, Bag3, Hsp70 and CHIP (HspB8:Bag3:Hsp70:CHIP) was found to be essential for the physiological maintenance of muscle integrity operating at the Z-disks (Arndt et al., 2010). The complex is responsible for the disposal, through macroautophagy, of mechanically damaged filamin, an actin-crosslinking protein essential for sarcomere integrity. Unfolded filamin is extracted from Z-disks by the action of HspB8 and Hsp70, with Bag3 coordinating their activities. CHIP ubiquitinates the client protein that is then presented to the macroautophagy receptor p62. p62 binds simultaneously to ubiquitin moieties and to the lipidated form of LC3 (LC3-II), which is connected to the autophagosome membrane (Lippai & Low, 2014). Once the autophagosome entraps the sequestered filamin, the next step comprises the degradation in lysosomes. Filamin turnover by this mechanism was further confirmed in smooth muscle and non-muscle cells, where CAMA is induced upon tension strain (Ulbricht et al., 2013).

Besides filamin and huntingtin, the HspB8:Bag3:Hsp70 complex also promotes the removal of mutant SOD1 insoluble aggregates and the truncated version of TDP-43 through macroautophagy. Both proteins are linked to different forms of amyotrophic lateral sclerosis and fronto lateral temporal dementia (FLTD) (Crippa et al., 2016, 2010b).

Other studies have shed light on the molecular mechanisms of CAMA. The PXXP region in Bag3 is essential for macroautophagy stimulation, since its deletion abrogates Bag3 capacity to avoid accumulation of aggregated huntingtin (Carra et al., 2008b). Earlier, this region was found to interact with the SH3-containing protein PLCγ (Doong et al., 2000). The PXXP region interacts with the dynein motor complex, so Bag3 selectively directs Hsp70 misfolded clients to the aggresome through microtubule transport for further degradation. Interestingly, in this study the ubiquitination of the client did not seem to be necessary for protein degradation (Gamerdinger et al., 2011b). The adaptor protein 14-3-3 interacts with the two RSQS motifs in Bag3 **(Figure 5.B)** and contributes to the association with the dynein motor.

The WW domain in the N-terminus of Bag3 interacts with a proline-rich region in SYNPO2, which in turn interacts with an autophagosome fusion complex. Through these interactions, Bag3 links the CAMA machinery to phagophore fusion and autophagosome formation. Additionally, the

Bag3 WW domain interacts with inhibitors of the YAP/TAZ pathway to upregulate the YAP/TAZ-mediated filamin transcription (Ulbricht et al., 2013). Through the same domain, Bag3 exerts an spatial regulation of mTORC1 to coordinate autophagy induction and protein synthesis (Kathage et al., 2017). Therefore, the HspB8:Bag3:Hsp70 complex is essential in mechanotransduction by integrating tension sensing, filamin degradation and transcription and autophagosome formation in cells subjected to mechanical stress.

In aged cells, the degradative capacity of the UPS decreases as the risk of accumulation of aggregates increases. At the same time, both transcription and translation levels of Bag3 are upregulated, while Bag1 is downregulated. Thus, CAMA emerges as a compensatory mechanism of protein degradation in aged and oxidation-stressed cells (Gamerdinger et al., 2009). When the degradation capacity of the proteasome is overcome, Bag3 coordinates the re-routing of proteasomal ubiquitinated-clients to macroautophagy (Minoia et al., 2014). Conversely, when the misfolded proteins cannot be efficiently transported for their degradation by macroautophagy, due to inhibition of dynein-mediated retrograde transport, Bag1 expression is upregulated. Under these circumstances, Bag1 targets misfolded proteins to the proteasome for their degradation (Cristofani et al., 2017).

Recently, a connection between cell division and autophagy involving HspB8:Bag3 was described (Varlet et al., 2017). Here, this complex regulates actin dynamics in cytokinesis, with HspB8-depleted cells showing a disorganized intercellular bridge.

Altogether, the HspB8:Bag3:Hsp70 multimeric complex stands as an essential hub for proteostasis in several tissues. Their components activate the macroautophagy machinery to eliminate misfolded or aggregated proteins. At the same time, it coordinates client sequestration, ubiquitination, transport and autophagosome formation, as well as transcription and translation to replenish the disposed proteins (Klimek et al., 2017).

The HspB8:Bag3:Hsp70 complex in granulostasis

Stress granules (SG) are membrane-less compartments containing RBP (RNA-binding proteins), ribosomal subunits, translation factors and sequestered mRNA. SG are induced in the cytoplasm by proteotoxic stress (Kedersha & Anderson, 2002). This protective mechanism temporarily stops translation of housekeeping genes to give priority to those proteins required to confront the stress conditions. By these means, SG keep mRNA and RBP protected from degradation until the stress is released (Alberti et al., 2017). Some of these RBP are TIA-1, hnRNPA1 or FUS, that harbor RNA-binding domains and intrinsically disorder domains that promote assembly into SGs (Gilks et al., 2004). *In vitro*, hnRNPA1 and FUS form dynamic structures that undergo liquid-liquid phase transition. However, these liquid structures eventually evolve into solid bodies like hydrogels or fibers, especially in mutated variants of these proteins associated to ALS (Molliex et al., 2015; Murakami et al., 2015; Patel et al., 2015). These solid bodies are similar in their appearance to the inclusions observed in ALS and fronto temporal dementia (FTD) (Robberecht & Philips, 2013).

As the stress diminishes, SG normally disassemble to restore translation. However, in ALS, aberrant SG do not disassemble and as a consequence, they are eliminated by autophagy. This aberrant transition is promoted by the accumulation of misfolded proteins during stress. Defective ribosomal products (DRiP), which are prematurely terminated polypeptides from disassembled polysomes constitute the main source of misfolded proteins in living cells (Schubert et al., 2000; Yewdell, 2002). DRiP accumulate in SG, affecting their dynamics and promoting the transition to an aberrant state (Seguin et al., 2014). A fraction of aberrant SG are degraded through autophagy, but a majority disassembles with the help of the HspB8:Bag3:Hsp70 complex. Moreover, the complex also targets the DRiP for degradation (Ganassi et al., 2016). A similar phenomenon was observed for the ALS-linked variant of SOD, with Hsp70 having a prominent role in SG dynamics (Mateju et al., 2017).

Therefore, the control by the HspB8:Bag3:Hsp70 complex of SG dynamics and composition, also known as granulostasis, ensures a proper translation restoration when the stress subsides. This chaperone-mediated regulation of SG may play an important role in ALS. Indeed, there is a protocol for a phase II clinical trial for the treatment of ALS, based on the enhancement of HspB8 expression by colchicine (Crippa et al., 2016; Mandrioli et al., 2019).

Diseases associated to mutations in HspB8 and Bag3

HspB8:Bag3:Hsp70 participates in the degradation of aggregating proteins linked to neurodegenerative diseases, including pathological variants of huntingtin (Carra et al., 2008b), the ALS-related mutant SOD1 and misfolded TDP-43 (Crippa et al., 2016; Gamerdinger et al., 2011b) or the androgen receptor mutant (PolyQ-AR), that leads to spinal bulbar muscular atrophy (SBMA). Indeed, upregulated levels of HspB8 and Bag3 were observed in astrocytes from human brains affected by different neurodegenerative diseases associated to protein aggregation (Seidel et al., 2012).

Three disease-related mutations in HspB8 (K141E, K141N and K141T) have been reported to affect the α-crystallin domain and impair its interaction with Bag3. Such mutations have been associated with neuromuscular diseases: distal hereditary motor neuropathy (dHMN type 2A), Charcot-Marie-Tooth disease type 2L (Irobi et al., 2004; Nakhro et al., 2013; Tang et al., 2005); and distal myopathy (Ghaoui et al., 2016). The molecular basis underlying these diseases is not clear yet, although several studies point to a defective capacity of the K141E mutant to prevent aggregation and stimulate macroautophagy.

Maintaining a fully functional CAMA machinery is essential for muscle integrity. *In vivo* studies in adult humans showed that upregulation of CAMA components is an adaptive response to acute and prolonged mechanical stimulation in skeletal muscle (Ulbricht et al., 2015). Conversely, Bag3 deficiency does not affect muscle formation in animal models, but they display impaired activity in post-natal stages, characterized by Z-disk disintegration and severe myopathy (Arndt et al., 2010; Homma et al., 2006). In humans, the Bag3 P209L mutant causes a dominant, progressive myofibrillar myopathy (MFM) in children, with accumulation of aggregates in muscle and Z-disk disintegration (Selcen et al., 2009). The mutation lies within the HspB8-binding motif and is a dominant gain-of-function mutation that causes aggregation of Hsp70, its client proteins and the mutant Bag3 itself (Meister-Broekema et al., 2018). Other Bag3 mutations have been detected in patients with MFM, neuropathies and dilated cardiomyopathy, linking Bag3 to heart disease (Arimura et al., 2011; Knezevic et al., 2015; Meister-Broekema et al., 2018; Semmler et al., 2014; Shy et al., 2017). So far, no disease-associated mutations have been found in Hsp70 genes (Kakkar et al., 2014).

There is an increasing understanding on the molecular basis of client protein detection and clearance by the HspB8:Bag3:Hsp70 complex, and how it is altered in pathological conditions. However, current knowledge about the complex at a structural level is limited, including how Bag3 coordinates the activity of the two chaperones. Structural information is required to understand the functional aspects of the complex and to be able to modulate its function. A limiting factor for structural studies is the flexible nature of the components, since the three harbour intrinsically disordered regions of variable extents. This factor, together with the size of the complex (175 kDa), hinders an approach based on X-ray crystallography and NMR. However, cryoelectron microscopy offers several advantages to deal with the structural heterogeneity expected for flexible complexes, especially after the recent advances in the field.

Cryoelectron microscopy as a means to solve the structure of macromolecular complexes

Cryoelectron microscopy (cryoEM) has become a reference technique, together with X-ray crystallography and NMR, for structure determination at (near-) atomic resolution (Murata & Wolf, 2018). CryoEM requires a small amount of sample, an advantage compared with NMR and X-ray, and allows the visualization of a wide range of sizes, from viruses (Liu et al., 2010; Sugita et al., 2018) to small proteins like streptavidin (52 kDa) (Fan et al., 2019; Herzik et al., 2017). Without the need for crystallization or isotopic labeling, cryoEM allows the study of macromolecular assemblies in vitrified solutions, which can also provide insights on their dynamic behavior in near physiological conditions.

Vitrification consists of applying the sample to a cryoEM grid and plunging it into a solution containing ethane cooled at liquid nitrogen temperature (-190 °C). Using this method, developed by Dubochet et al. in the 80s, the temperature decreases at such rate that water molecules cannot arrange in crystals, but remain disorganized forming vitreous ice (Dubochet et al., 1988). Ideally, the specimen is preserved in a thin water layer, slightly thicker than the longer molecule dimension, with evenly distributed particles suspended across the grid support **(Figure 6)**. This kind of ice preserves the integrity of proteins in solution and allows operation under vacuum conditions in the microscope, while the low temperature slows the rate of radiation damage (Carroni & Saibil, 2016).

In recent years, critical advances in the field have pushed cryoEM to atomic resolution, which has been referred to as the *resolution revolution* (Bai et al., 2015). One of the most relevant advances was the development of the direct electron detectors (DED), which enable the direct detection of incoming electrons as they pass through a thin (10 µm) semiconductor wafer. Here, electrons deposit their energy, which is detected by the electronics incorporated (Bai et al., 2015). Given the high sensitivity of these detectors, the total electron dose must be spread over multiple frames, so DED collect movies rather than individual images. The main advantage of collecting frames is that these can be further aligned to compensate stage- and electron beam-induced movements, preserving high resolution information (Brilot et al., 2012; Li et al., 2013). Moreover, DED offer a better detective quantum efficiency (DQE) (i.e. how the signal-to-noise ratio, SNR, of the initial signal is degraded by errors during the detection process) than previous CCD (charge-coupled device) and films (Bai et al., 2015).

Together with the development of DEDs, 2D and 3D classification methods have improved with the use of maximum likelihood-based algorithms, combined with a novel Bayesian approach, which introduced a regularization term to the likelihood function (Scheres, 2016).

Conformational heterogeneity has been a problem in 3D reconstruction, but recent advances in image processing enable discerning between discrete conformations co-existing in solution (Loveland et al., 2017; Nakane et al., 2018; Zhao et al., 2015), a problem that could not be tackled in the case of X-ray crystallography and NMR.

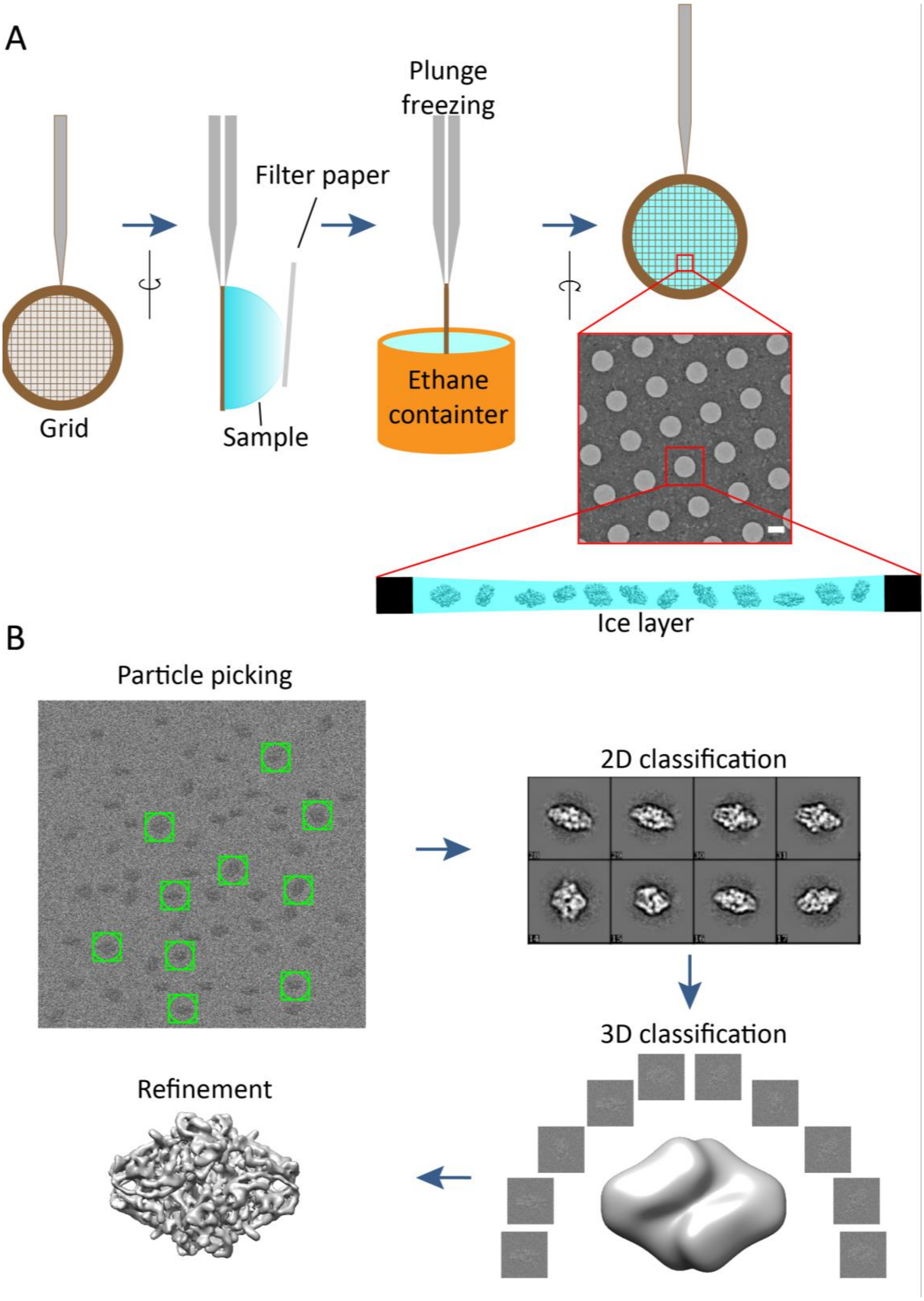

Figure 6. General workflow of cryoEM. (A) *Sample containing proteins in solution is applied to a grid support. The excess of sample is removed with filter paper from the grid that is then immediately sunk in liquid ethane for vitrification. As a result, the molecules remain in a thin layer of vitrified ice for subsequent imaging.* ***(B)*** *Single particle analysis for 3D reconstruction of macromolecular assemblies. Particles are picked and extracted from the aligned micrographs, then subjected to 2D classification to clean the dataset and identify protein views. Subsequent 3D classification allows the assignment of angles to the particles to reconstruct a 3D map of the specimen. Finally, the map is refined for a more accurate angle assignment, which allows the reconstruction of a high-resolution 3D map (in this case obtained from (Chen et al., 2013a)).*

The microscope optics have also experienced progressions with the incorporation of energy filters, a third condenser lens for parallel illumination and new field emission guns with higher coherence and improved stage stability.

Due to the low SNR, images are acquired with certain defocus to be observed, with the subsequent loss of high-resolution information as the defocus increases. The development of in-focus phase plates, namely the Volta phase plate (VPP), has allowed an increment of phase contrast at near-focus, with longer lifespan and reduced artifacts than previous phase plates (Danev et al., 2014). The VPP consists of a heated continuous amorphous carbon film (10 nm) placed at the back-focal plane in the electron microscope. The interaction of the beam with this film introduces a phase shift between the scattered and unscattered electrons, which yields images with an increased contrast even close to focus. The VPP has contributed to solve the structure of small, low-contrast particles (Fan et al., 2019; Khoshouei et al., 2016).

Additional developments include remote control of the microscope, fully automated data collection and reduced computing time thanks to parallelization in GPU-implemented in image processing software (Kimanius et al., 2016; Murata & Wolf, 2018).

In conclusion, cryoEM has become a powerful technique to solve the structure of macromolecules that have remained elusive for other structural techniques due to their physicochemical properties.

OBJECTIVES

OBJECTIVES

1. Generation of a homogeneous and stable HpsB8:Bag3:Hsp70 complex.

2. Biophysical characterization of the HspB8:Bag3:Hsp70 complex.

3. Structural characterization of the HpsB8:Bag3:Hsp70 complex by cryoEM.

MATERIALS AND METHODS

MATERIALS AND METHODS

DNA manipulation

Bacterial transformation

Escherichia coli competent strains were transformed with a heat shock protocol as follows: 50 ng of purified plasmid or 5 µl of ligation reaction were added to 100 µl of the corresponding *E. coli* strain and incubated sequentially at 4°C for 30’, 42°C for 1’20’’ and 4°C for 5’ (Inoue et al., 1990). Then, transformed cells were incubated for 1h at 37°C with 900 µl of fresh LB (Bertani, 1951) at 400 rpm for recovery. Cells were plated on LB-agar plates supplemented with the corresponding antibiotics and incubated o/n (overnight) at 37°C.

Plasmid DNA extraction

Selected colonies from LB-agar plates were grown in 3 ml of LB medium with antibiotics o/n at 37°C and 190 rpm. Cells were centrifuged at 8000 rpm for 3’ and the plasmids were purified from pellets with QIAprep Spin Miniprep Kit (Qiagen), following the manufacturer’s instructions.

DNA agarose electrophoresis and gel band purification

DNA was examined by electrophoresis in 1% (w/v) low EEO agarose (Conda) in TAE buffer with 0.5 µg/ml ethidium bromide. DNA Loading buffer was added to the samples, which were run at 100 V. A 1kb DNA Ladder (Promega) was used as marker. Gels bands were visualized with GelDoc XR (BioRad) and imaged with QuantityOne 4.6 software (BioRad). The bands of interest were purified from gels with the QIAquick Gel Extraction Kit (Qiagen). DNA concentration was measured with Nanodrop 1000 (Thermo Fisher Scientific).

HspB8 and Bag3 cloning

Coding sequences for human Bag3 and HspB8 were amplified from the cDNA library MTC Multiple Tissue cDNA Panels (Clontech) from heart muscle, and cloned into a pGEMT vector (Promega). HspB8 cDNA was amplified using primers M011 and M012 **(Table 1)**. Bag3 cDNA was amplified with primers M009 and M010. All fragments were amplified with the Expand High

Fidelity polymerase (Roche) in a GeneAmp PCR System 2700 thermal cycler (Applied Biosystems). The cycling parameters for each reaction are indicated in **Table 2**. The gel purified Bag3 band or amplified HspB8 directly from the PCR were cloned into pGEMT with the T4 ligase at 8°C o/n (plasmid names: pGEMT-Bag3, pGEMT-HspB8). Plasmids from colonies of *E. coli* DH5α transformed with the ligation reaction were checked by digestion with *Nde*I and *Nco*I restriction enzymes (New England Biolabs). The identity of the HspB8 and Bag3 positive clones was further confirmed by sequencing (Secugen).

In order to facilitate further protein purification, fusion proteins with an N-terminal tag (6xHis-lypoyl domain-TEV) were engineered (Fernandez-Fernandez et al., 2005). The recombinant DNA was created by overlapping PCR by fusing a sequence coding for the tag to the 5’ end of HspB8/Bag3 sequence, as explained in **Figure 7**.

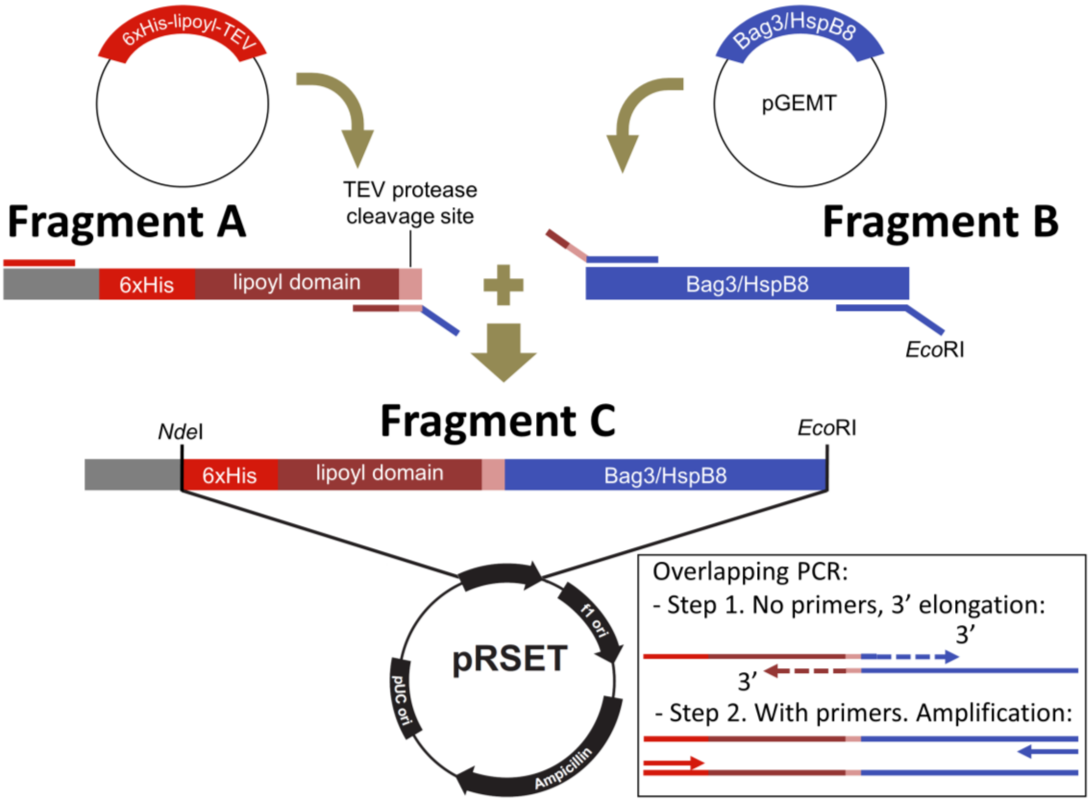

Figure 7. Scheme of the cloning procedure for HspB8 and Bag3 by overlapping PCR. *A recombinant DNA was produced by fusion of two DNA fragments by overlapping PCR: 1) Independent amplification of fragments A (containing a* *<u>NdeI</u>* *restriction site, a histidine-tag, lipoyl domain and a TEV protease cleavage site) and B (coding sequence for HspB8/Bag3 and* *<u>EcoRI</u>* *restriction site). Primers were designed in such a way as to add overlapping sequences for*

the next step. 2) Generation of fragment C by overlapping PCR in two steps: a first PCR without primers for elongation from the 3′ of the overlapping sequences, which was used as product for a second PCR including flanking primers for fragment C amplification.

Primers and templates used to amplify fragments A and B for further overlapping PCR are shown in **Table 1.** To generate the fragments C_{B8} and C_{Bag3}, 200 fmoles of the fragments A_{B8} and B_{B8} or 300 fmoles of A_{Bag3} and B_{Bag3} were mixed in a PCR without primers. These reactions served as templates to amplify the C fragments with the corresponding flanking primers: T7 and M015 for C_{B8}, T7 and M006 for C_{Bag3}. The cycling parameters for overlapping PCR are listed in **Table 2**.

Gel purified C_{B8} and C_{Bag3} bands were cloned in pRSET-B with *Nde*I and *EcoR*I restriction sites. Ligation reactions were set with an insert:vector ratio of 15:1 at 4°C o/n (plasmid name: pRSET-HspB8) or 7:1 at 16°C o/n (plasmid name: pRSET-Bag3). Constructions were sequenced for verification, and mutations affecting the final amino acid sequence were corrected with QuikChange Site-Directed Mutagenesis Kit (Stratagene) and verified again by sequencing.

Hsp70 cloning

The coding sequence for human Hsp70 was cloned in pPROEX-HTa for the expression of recombinant Hsp70 with His-tag removable by TEV digestion. The Hsp70 sequence was amplified from the pQE30-His-Hsp70 plasmid (Quintana-Gallardo et al., 2019) with primers M016 and M017, that added a short sequence that overlaps with *Sfo*I-digested pPROEX-HTa ends. The In-Fusion cloning system (Takara) was used following manufacturer's instructions, and 50 ng of digested pPROEX were incubated with 100 ng insert.

Target	PCR	Primer name	Sense	Sequence	Template
Bag3	A	M004	R	GGTGGCGGCGCTCATTCCCTGGAAGTACAG	pRHislipoTEV-p53CT[1]
	B	M005	F	CTGTACTTCCAGGGAATGAGCGCCGCCACC	pGEMT-Bag3
		M006	R	CGGAATTCCTACGGTGCTGCTGGGTTACC	
		M009	F	CGCCTTTAATTCATAAAGGTGCCCGGCG	cDNA library
		M010	R	TTTTTACAGGGCAGAGGCTACGGTGCTG	
	A	T7	F	AATACGACTCACTATAGGG	

HspB8		M011	F	TCCCTGGCAGTGGTTGGTTCTGCTTCTC	cDNA library
		M012	R	GTCAGTCCTCACCCCCGCACCCTCTAAC	
	A	M013	R	CTGACCGTCAGCCATTCCCTGGAAGTACAGG	pRHislipoTEV-p53CT*
	B	M014	F	CTGTACTTCCAGGGAATGGCTGACGGTCAGATGC	pGEMT-HspB8
		M015	R	GCGAATTCTCAGGTACAGGTGACTTCCTGG	
Hsp70		M016	F	CTGTATTTTCAGGGCATGGCCAAAGCCGCGGCG	pQE30-His-Hsp70[2]
		M017	R	TTCCGGATCCATGGCCTAATCTACCTCCTCAATGGTGG	

[1] From (Fernandez-Fernandez et al., 2005). [2] From (Quintana-Gallardo et al., 2019).

Table 1. List of primers used for cloning. *Underline: restriction sites for EcoRI. Bold underline: START codon. Double underline: STOP codon. Dashed underlines: overlapping sequences introduced for overlapping PCR. F: Forward. R: Reverse.*

Target DNA	**Cycling conditions**
HspB8/Bag3 from cDNA library	95°C 1’, (95°C 30”, 68°C 3’, 68°C 3’) x 30 cycles
A_{B8} / B_{B8} / A_{Bag3}	92°C 5’, (92°C 1”, 50°C 45”, 68°C 2’) x 25 cycles, 68°C 5’
B_{Bag3}	94°C 5’, (94°C 30”, 68°C 2’30”) x 30 cycles, 68°C 1’
C_{B8} elongation	94°C 2’, (94°C 30”, 60°C 1’, 72°C 2’) x 99 cycles, 72°C 5’
C_{B8} amplification	94°C 2’, (94°C 30”, 55°C 1’, 72°C 2’ 30”) x 30 cycles, 72°C 7’
C_{Bag3} elongation/amplification	94°C 2’, (94°C 30”, 60°C 5’, 72°C 2’) x 50 cycles, 72°C 7’
Hsp70 from plasmid	94°C 5’, (94°C 30”, 57°C 30”, 72°C 1’ 30”) x 25 cycles, 72°C 5’

Table 2. Cycling parameters used for the different PCR.

Protein expression

Protein electrophoresis

Protein samples were analysed by SDS-PAGE following the standard protocol described in (Maniatis et al., 1982). 6, 10 or 15% polyacrylamide gels were prepared depending on the molecular weight of the protein of interest. Samples were incubated with SDS-PAGE Loading Buffer and boiled at 95°C for 3-5’. 3 µl of Precision Plus Protein Standards molecular weight markers (BioRad) were also loaded. Gels were run at 50 mA in SDS-Running buffer and stained with Quick Coomassie Stain (Generon) for 15’.

A silver staining protocol was also used to stain gels of GraFix fractions. Gels were soaked in the fixation solution **(see LIST OF BUFFERS)** for 1h and washed 4 times with 50% ethanol for 10', shaking gently. The fixed gel was transferred to a thiosulfate solution for 1', washed twice in MilliQ H_2O for 20" and rinsed in staining solution for 20'. After two washings of 20" in MilliQ H_2O, the gel was soaked in the developing solution. The reaction was stopped by soaking the gel in the fixation solution.

For Blue Native-PAGE, samples were mixed with Blue-Native loading buffer and loaded in 6% acrylamide native gels (Schägger et al., 1994). Gels were run at 15 mA in Native running buffer.

Western blot

Protein bands from SDS-PAGE were transferred to a nitrocellulose membrane (BioRad) soaked in Transfer buffer using a semi-dry transfer system (BioRad) at 245 mA for 1h. The membrane was stained with Ponceau 0.1% for a rapid visualization of the transferred proteins, and blocked with 5% non-fat dried milk in PBS-Tween 0.1%. The membrane was incubated with 5 ml of mouse monoclonal antibody against BAG3 at 1:5000 in blocking solution (Novus Biologicals, Ref: H00009531-M01A) o/n at 4°C with mild shaking. Three washing steps of 10' in PBS-Tween were performed before incubating with 5 ml of a 1:5000 dilution of secondary antibody against mouse IgG coupled to horseradish peroxidase (NA931, GE Healthcare) in blocking solution 1h at RT. The membrane was washed with PBS-Tween three times for 10' and incubated with Clarity Western ECL substrate (BioRad). The chemoluminiscent bands were exposed to autoradiography films (Kodak) for developing.

Expression screening

E. coli strains used for expression screening were BL21(DE3) (Bag3, Hsp70), C41(DE3) (HspB8, Bag3, Hsp70), Rosetta(DE3)pLysS (Bag3, Hsp70) and C43 (Bag3). Temperatures for expression were 16°C, 25°C, 30°C and 37°C and two growth media were tested: IPTG-induction in LB medium and auto-induction medium (AIM) (Studier, 2005). All the incubations were carried out at 190 rpm with the corresponding antibiotics. As a general procedure, 100 µl of bacteria were transformed with 50 ng of the expression plasmids. For IPTG-expression, a preculture for each strain was grown in LB with antibiotics at 37°C o/n and inoculated to the final culture until $O.D._{600}= 0.1$. Cultures were incubated at 37°C until $O.D._{600}= 0.4\text{-}0.6$, when they were set to the indicated temperature and IPTG concentration for expression induction **(Figure 1Figure 8)**.

For expression in AIM, transformed colonies were suspended in fresh AIM and then inoculated to the final volume of AIM at the desired temperature. When the expression test was performed at 16°C, the culture was preincubated at 37°C for 3 h. Cells were lysed either by sonication (IPTG-induced HspB8 and Bag3) or by boiling an aliquot with Loading buffer at 95°C for 3’ (Hsp70 and AIM HspB8 and Bag3). Overexpression was checked by SDS-PAGE, and the lysate volumes were normalized according to the final O.D.$_{600}$ of the culture for appropriate comparison.

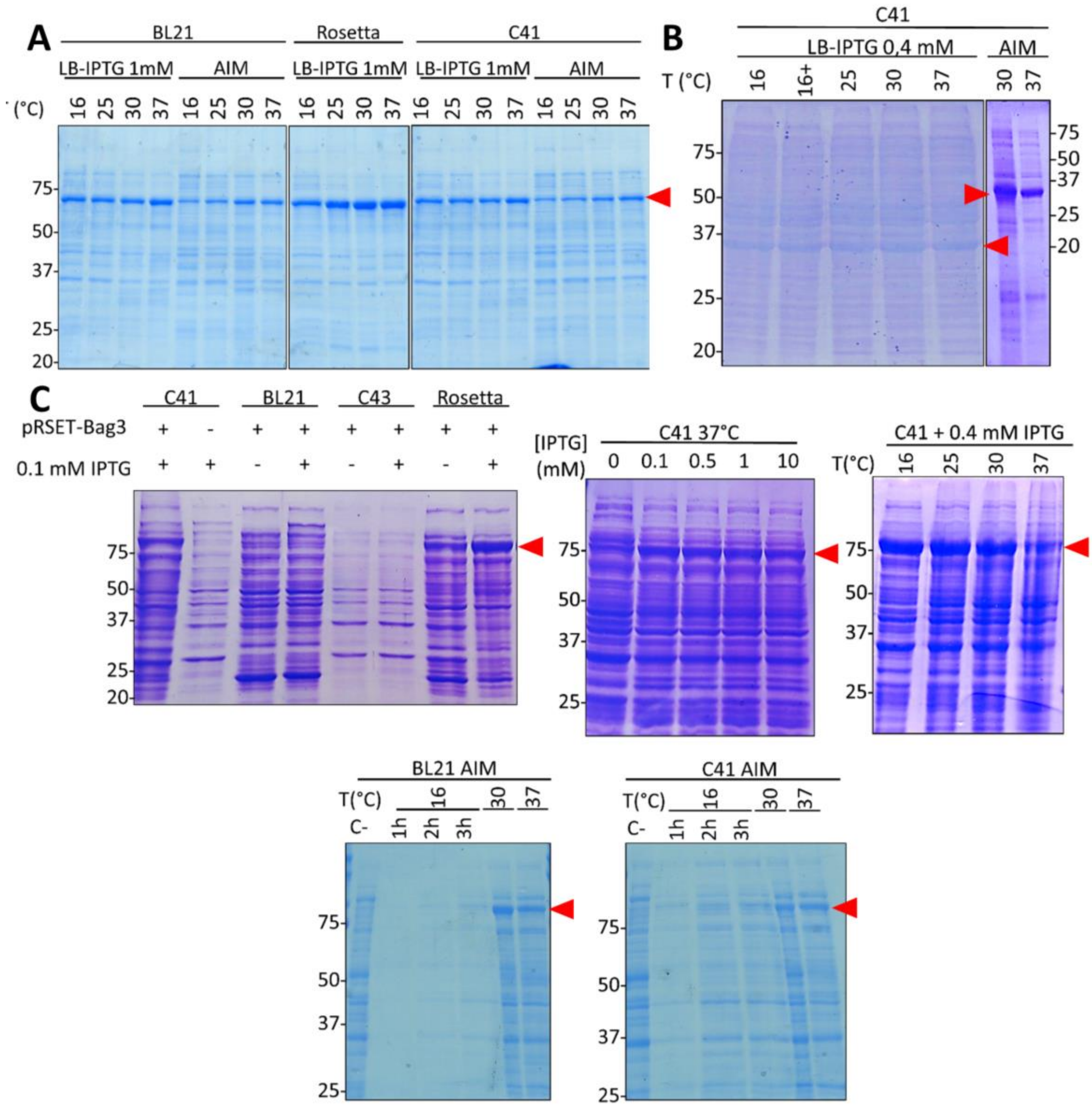

Figure 8. Expression screenings for Hsp70 (A), HspB8 (B) and Bag3 (C). *Each protein was expressed o/n except indicated otherwise:* ***(A)*** *BL21 and C41 LB-IPTG at 25°C, 30°C and 37°C (6 h).* ***(B)*** *C41 in LB-IPTG at 25°C, 30°C and 37°C (7 h).* ***(C)*** *Strain screening (upper left) was performed at 37°C. Expression in LB-ITPG was for 3 h. Red arrowheads indicate the full-length recombinant protein in each gel.*

Protein expression

Conditions with the highest overexpression levels were selected for the growth of larger cultures for protein expression. For Hsp70, the selected condition was Rosetta in LB-IPTG at 30°C o/n. For Bag3, overexpression was carried out in C41 in AIM at 30°C o/n. For HspB8, the selected condition was BL21 in AIM at 30°C o/n. For TEV protease, expression was induced as for Hsp70, but with 0.1 mM IPTG for 5 h at 30°C in LB medium supplemented with kanamycin. Bacterial cultures were pelleted by centrifugation in a Hitachi CR 22N centrifuge at 5000 rpm for 10'. For long-term storage, pellets were resuspended in PBS 1x or fresh LB medium, centrifuged in falcon-like 50 ml tubes at 5000 rpm 15' and stored at -20°C until further use. His-Hsp70, a recombinant protein with non-cleavable tag used in some experiments, was expressed from plasmid pQE30-His-Hsp70 as in (Quintana-Gallardo et al., 2019).

Protein purification

Proteins were purified following the general workflow shown in **Figure 9** in AKTA FPLC systems, at 25°C (TEV protease) or 4°C (Hsp70, Bag3, HspB8). The eluted fractions were examined by SDS-PAGE in 10% (Hsp70, Bag3) or 15% (HspB8, TEV) polyacrylamide gels. The purified proteins are shown in **Figure 10**.

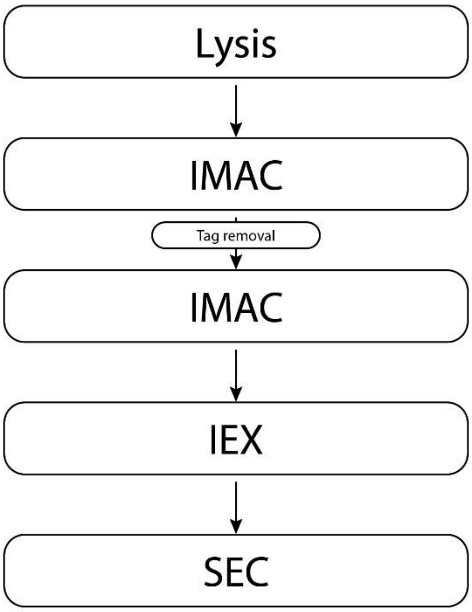

Figure 9. General chromatography steps of protein purification. *IMAC: Immobilized Metal Ion Affinity Chromatography. IEX: Ion Exchange Chromatrography. SEC: Size Exclusion Chromatography.*

Lysis

Pellets corresponding to 1 L (Hsp70, Bag3, TEV) or 0.5 L (HspB8) of culture were thawed in 40 ml of the corresponding Buffer A IMAC **(see LIST OF BUFFERS)** with cOmplete EDTA-free Protease Inhibitor Cocktail (Roche). The resuspended pellet was sonicated on ice with alternating sonication pulses of 5’’ and 40’’ pauses for a total sonication time of 60-80” with an amplitude of 50% in a Digital Sonifier 250 (Branson). Cell lysates were centrifuged at 40000 rpm 30’ at 4°C in a 50.2 Ti rotor with a Beckman L-70 Ultracentrifuge and the supernatant filtered with syringe filters of 0.45 and 0.22 µm (Millipore) for clarification.

Immobilized metal ion affinity chromatography

The cleared lysate was subjected to a first immobilized metal ion affinity chromatography (IMAC). For that, the filtered lysate was loaded onto a HisTrap FF 5 ml column (GE Healthcare) at 5 ml/min flow rate. Then, the column was washed with several column volumes (CV) of the corresponding Buffer A IMAC and the bound protein was eluted as follows: 100% Buffer B IMAC-Hsp70 for Hsp70, 15% B Buffer B IMAC-Bag3 for Bag3, 40% Buffer B IMAC-HspB8 for HspB8 and 10-50% Buffer B IMAC-TEV along 5 CV for TEV.

The eluted fractions were analyzed by SDS-PAGE, and those containing the protein with removable tag were pooled and incubated o/n with the TEV protease while dialyzed against 2 L of Buffer A IMAC. In order to separate the digested tag and the uncut fraction from the cleaved protein, the sample was subjected to a second IMAC. The unbound fractions, corresponding to digested protein, were pooled and dialyzed against the buffers described below for each protein.

Ion exchange chromatography

For Hsp70/His-Hsp70, pooled fractions from the IMAC were dialyzed against 2 L of Buffer A IEX-Hsp70 for 5 hours. The dialyzed sample was diluted 1:5 with Buffer A IEX-Hsp70 to decrease salt concentration before loading it onto a HiTrap Heparin HP 5 ml column (GE Healthcare) at 5 ml/min. The elution was performed with a linear gradient of 10-25% buffer B IEX-Hsp70 in 30

CV, and two peaks, one corresponding to Hsp70 monomer and the other to a mixture of monomer and dimer could be separated. The fractions from the monomeric peak were concentrated to 5 ml with Amicon Ultra-15 Centrifugal 30K filters (Millipore).

For Bag3, pooled fractions from the second IMAC were dialyzed against 2 L of Buffer A IEX-Bag3 for 5 hours. The dialyzed sample was diluted 1:5 with Buffer A IEX-Bag3 without NaCl to decrease salt concentration before loading. The diluted sample was applied to a HiTrap Q HP 5ml (GE Healthcare) at 5 ml/min, and eluted at 15% Buffer B IEX-Bag3. The selected fractions were concentrated to 5 ml with Amicon Ultra-15 Centrifugal 10K filters (Millipore).

For HspB8, fractions from the second IMAC were dialyzed against 2 L of Buffer A IEX-HspB8 with 100 mM NaCl for 5 hours and diluted afterwards 1:5 with Buffer A IEX-HspB8 without NaCl. The sample was loaded onto a HiTrap Heparin HP 5 ml column at 5 ml/min equilibrated with Buffer A IEX-HspB8. Fractions eluted at 30% Buffer B IEX-HspB8 were concentrated to 5 ml with Amicon Ultra-15 Centrifugal 10K filters (Millipore).

Size exclusion chromatography

The concentrated inputs were loaded onto a Superdex 200 HiLoad 16/600 (GE Healthcare) at 0.6 ml/min previously equilibrated in Buffer SEC-Hsp70 (for Hsp70 and Bag3) or Buffer SEC-HspB8 (for HspB8). Those fractions with highest purity, as checked by SDS-PAGE, were pooled, concentrated and frozen in liquid nitrogen for long-term storage at -80°C. Additionally for Hsp70, fractions were also analyzed by Native-PAGE to check for the oligomerization state, selecting those fractions containing only the monomeric form. The protein concentration was measured in BioSpectrometer basic (Eppendorf). A summary of the result of each purification step is shown in **Figure 10**.

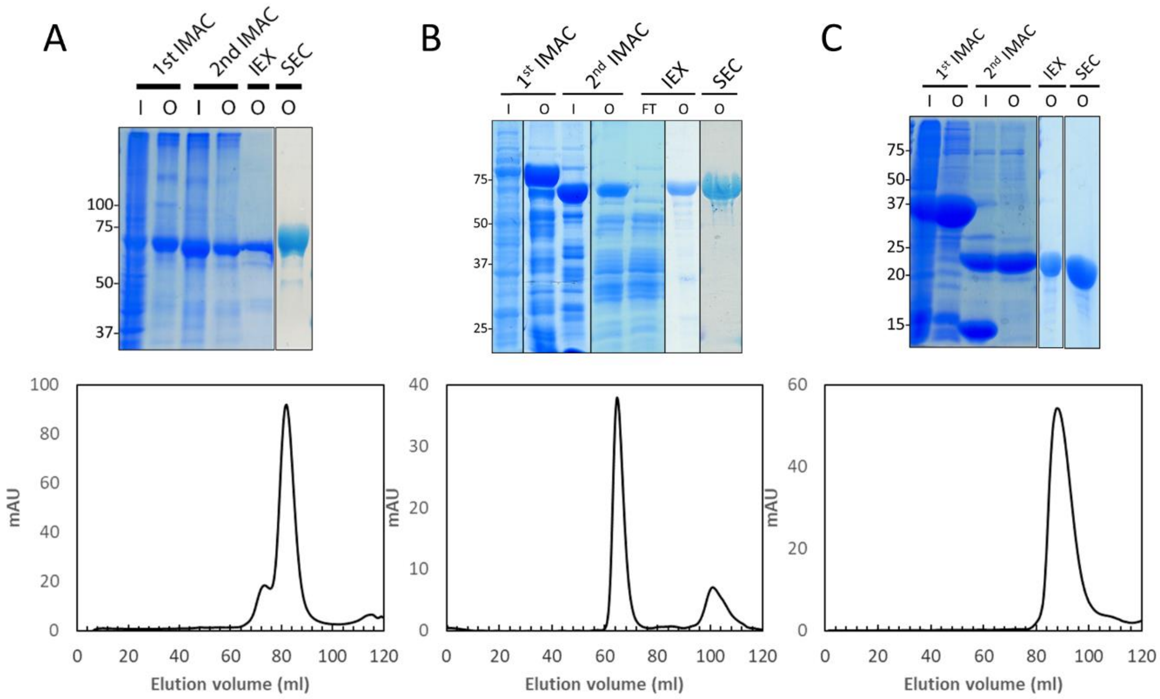

Figure 10. Purification steps for Hsp70 (A), Bag3 (B) and HspB8 (C). *Upper panels: SDS-PAGE showing inputs and outputs of the indicated purification step. Lower panels: SEC profiles of the last purification step. Fractions of the main peaks were concentrated and loaded as SEC output in upper panels. I: input; O: output; FT: flow-through.*

Biophysical studies

Analytical Size Exclusion Chromatography

A total of 500 µl of 14 µM HspB8, 7 µM Bag3 and 7 µM His-Hsp70 were incubated in Buffer Complex for 5-10' at 22°C in the different permutations before loading onto a Superdex 200 Increase 10/300 GL (GE Healthcare) equilibrated with the Buffer Complex. Fractions were analyzed by SDS-PAGE and used for further applications.

For HspB8 oligomerization experiments, 100 µl of protein at 9, 20 and 88 µM were loaded onto a Superdex 75 10/300 GL (GE Healthcare).

For Bag3:HspB8 stoichiometry experiments, 100 µl of Bag3 and HspB8 at the indicated molar ratios were loaded onto a Superdex 200 Increase 10/300 GL equilibrated with Buffer SEC-HspB8. HspB8:Bag3 complexes were incubated at 22°C for 10' before loading.

SEC experiments comparing the complex crosslinked by the GraFix method in the presence or absence of ADP were performed in a Superdex 200 Increase 3.2/300 equilibrated with Buffer Complex. 50 µl of the concentrated fractions from GraFix containing the ternary complex in each condition were loaded as input.

For SEC experiments of the native complex comparing apo- and ADP-bound state, 10 µl with 28 µM HspB8, 14 µM Bag3 and 14 µM Hsp70 were incubated at 22°C for 10' with or without 2 mM ADP. The samples were loaded onto a Superdex 200 Increase 5/150 GL (GE Healthcare) equilibrated with Buffer Complex with or without 2 mM ADP.

The native HspB8:Bag3:Hsp70 complex for cryoEM was prepared as follows: 50 µl of 14 µM HspB8, 7 µM Bag3 and 7 µM Hsp70 were incubated at 22°C for 5' and loaded onto a Superdex 200 Increase 3.2/300 (GE Healthcare) to minimize sample dilution. Fractions containing the complex were immediately vitrified or after incubation with 2 mM of ADP, ATP or AMP-PNP 5'.

Analytical Ultracentrifugation experiments

AUC experiments were carried out at the Molecular Interaction Facility at the Centro de Investigaciones Biológicas (CIB-CSIC, Madrid) in an Optima XL-I analytical ultracentrifuge (Beckman-Coulter) equipped with UV-VIS absorbance and Raleigh interference detection systems.

Sedimentation velocity Analytical Ultracentrifugation (SV-AUC)

HspB8, Bag3 and His-Hsp70 were buffer-exchanged to Buffer Complex with 0.1 mM β-ME instead of DTT. The different protein complexes were incubated at the indicated concentrations and loaded (420 µl) onto the analytical ultracentrifugation cells. All the experiments were performed at 48000 rpm at 4°C and the sedimentation profiles were recorded at 280 nm. The sedimentation coefficients (SE) were calculated by least squares boundary modelling of sedimentation velocity data using the continuous distribution c(s) Lamm equation model implemented by SEDFIT 15.01 (Schuck, 2000). The experimental sedimentation coefficients were corrected for solvent composition with the program SEDNTERP (Laue, 2000) to obtain the standard s-values ($S_{20,w}$).

Sedimentation equilibrium Analytical Ultracentrifugation (SE-AUC)

HspB8 was buffer exchanged to Buffer Complex with or without 0.1 mM TCEP using illustra NAP-5 columns (GE Healthcare). SE experiments were carried out at 280 nm with speeds ranging from 12000 to 16000 rpm. A high-speed centrifugation run at 48000 rpm was performed to estimate the corresponding baseline. Weight-average buoyant molecular weights were determined using HeteroAnalysis program (Cole, 2004) and corrected for solvent composition and temperature with SEDNTERP.

Circular dichroism

HspB8, Bag3 and His-Hsp70 were buffer exchanged to a filtered Buffer CD **(LIST OF BUFFERS)**, compatible with CD measurements and incubated at 22°C for 5' for complex formation. CD spectra from 190 to 250 nm (collected every 1 nanometer) were recorded on a Chirascan CD spectrometer (Applied Photophysics) at 20°C in cuvettes with 0.02 or 0.05 cm path lengths.

ProteoPlex

The ProteoPlex assay for screening of stabilizing buffer conditions for the complex (Chari et al., 2015) was a kind offer from Prof. Holger Stark (Max Planck Institute for Biophysical Chemistry, Göttingen, Germany). Samples were sent in Buffer SEC-Hsp70 (Bag3) and Buffer SEC-HspB8 (HspB8, His-Hsp70).

Crosslinking and mass spectrometry analysis

The LC-MS analysis was a service carried out by the Proteomics facility at the CNB. HspB8, Bag3 and Hsp70 were incubated in Complex Buffer with 10 mM BS3 (Thermo Scientific) 30' at 25°C. The reaction was quenched with 50 mM Tris pH 7.3, mixed with Loading Buffer and subjected to SDS-PAGE. The gel band was excised from the Coomassie-stained 6% gel and subjected to automated reduction, alkylation with iodoacetamide and trypsin digestion in a Proteineer DP robot (Bruker Daltonics). The resulting peptide mixture was speed-vac dried and re-dissolved in 0.1% formic acid. The LC-MS/MS analysis was carried out using a nano-LC Ultra HPLC (Eksigent) coupled to a 5600 triple TOF mass spectrometer (AB Sciex) through a nanospray III ion source (AB Sciex) equipped with a fused silica PicoTip emitter (10 µm x 12 cm, New Objective). The HPLC setup included an Acclaim PepMap 100 trapping column (100 µm x 2 cm, 5 µm particle size, Thermo Scientific) and an Acquity UPLC BEH C18 column (75 µm x 150 mm, 1.7 µm particle size, Waters). Solvent A and B were 0.1% formic acid and 0.1% formic acid in acetonitrile, respectively. Peptides were fractionated at 0.250 ml/min flowrate at 50°C under gradient elution conditions consisting of 2% B for 1’, a linear gradient to 30% B in 109’, a linear increase to 40% B in 10’, a linear increase to 90% B in 5’ and 90% B for 5’. The ion source was operated in positive ionization mode at 150°C with a potential difference of 2300 V. Each acquisition cycle included a survey scan (350-1250 m/z) of 250 ms and a maximum of 25 MS2 spectra (100-1500 m/z). For peptide identification, raw MS data were converted to a .mgf file using PeakView v2.2 (AB Sciex). The search was against a custom-made database containing the sequences of the proteins in the complex. The MS/MS ion search and crosslinked product analysis were performed with Stavrox 3.6.6 (Götze et al., 2012). Search parameters were set as follows: trypsin as enzyme allowing 2 and 3 missed cleavages for R and K, respectively, BS3 as crosslinker, MS tolerance of 20 ppm and MS/MS tolerance of 40 ppm, carbamidomethylation of cysteins as fixed modification and oxidation of methionines as variable modification. Peptide identifications were filtered at a FDR < 5%.

Sample preparation for cryoelectron microscopy

Complex stabilization with GraFix

Complexes were stabilized and isolated for electron microscopy applications using GraFix (Kastner et al., 2007), a method for mild fixation of macromolecular complexes. For gradient formation, 2.5 ml of a 10% sucrose, glutaraldehyde-free solution (Top Buffer) was carefully applied on top of 2.5 ml of a denser solution containing 25% sucrose and 0.15% glutaraldehyde (Bottom Buffer), avoiding their mixing. Buffers were previously filtered with 0.22 µm syringe filters. A Gradient Master device (BioComp) was used to produce a linear gradient of 10-25% sucrose and 0-0.15% glutaraldehyde. 50 µl of a solution containing 28 µM HspB8, 14 µM Bag3 and 14 µM Hsp70 were incubated in Buffer Complex ± 2mM ADP for 10’ at 22°C in the absence of crosslinker. The mixture was then applied to the top of the gradient and centrifuged 16 h at 44.000 rpm 4°C using an SW55 Ti rotor in a Beckman XL-90 ultracentrifuge. As control, a gradient made with glutaraldehyde-free Bottom Buffer was run in parallel. Fractions of 200 µl were manually collected from the top of the gradient, subjected to SDS-PAGE in 6% polyacrylamide gels and subjected to silver staining. The fractions containing the crosslinked complex were concentrated using Vivaspin 500 10k columns (GE Healthcare) in rounds of 5’ at 7000 g at 4°C, refilling with Buffer Complex for buffer exchange to remove glycerol. Sample was quality-controlled by negative staining at 0.02 mg/ml before vitrification.

Negative Staining

Aliquots of 10 µl samples were applied onto glow-discharged carbon-coated Cu/Rh 300 mesh grids (Electron Microscopy Science) and incubated for 1'. For samples containing a high concentration of sucrose, incubated grids were washed by touching with two 20 µl droplets of 20 mM HEPES pH 7.4 prior blotting. Excess of sample was laterally blotted with a filter paper grade 1 (Whatman). Proteins adsorbed were stained with 10 µl of 2% (w/v) uranyl acetate for 1'. Grids were examined using a JEOL JEM 1011 transmission electron microscope equipped with a Gatan ES1000Ww camera.

Grid supports

CryoEM grids (Quantifoil, Electron Microscopy Science) used in this work are listed in **Table 3.**

Grid support (300 mesh)	**Hole pattern**		**Graphene oxide**
	0.6/1	**1.2/1.3**	
Cu/Rh	*Q350CR-06*	*Q3100CR1.3*	No
	Q350CR-06	*Q3100CR1.3*	Yes
UltrAuFoil	*Q350AR1A*	*Q350AR13A*	No

Table 3. Grids tested for cryoEM. *The reference number for each grid is indicated in italics.*

A graphene oxide (GO) (Sigma Aldrich) 1:10 solution was prepared and centrifuged at 300 g 15" to pellet GO flakes. A 3 µl aliquot of supernatant was applied for 1' onto glow-discharged Cu/Rh 300 mesh grids (Quantifoil). Grids were blotted with filter paper grade (Whatman) from the back side and washed by touching three times by the front side with 20 µl MilliQ H_2O droplets. Grids were air-dried and no additional glow was needed for sample application.

Grids for negative stain were glow-discharged at 25 mA 15" in an Emitech K100X system (Quorum Technologies). Grids for cryoEM were treated as follows: Cu/Rh grids were either untreated or glow-discharged at 20-25 mA for 30"-1'; UltrAuFoil grids were glow-discharged at 15 mA for 3'.

Vitrification

CryoEM grids were vitrified in a Vitrobot Mark IV (FEI) set to 4°C and 95% humidity. Aliquots of 3 µl with the sample were applied to the grid, with no incubation, in the conditions listed in **Table 4**. Vitrified grids were stored in grid containers at liquid nitrogen temperature for further screening.

Sample	Concentration (mg/ml)	Force	Blotting time (s)	Grid type	Glow treatment	Acquisition
Native	0.8	-15	3	Cu/Rh R 0.6/1	25 mA 30”	-
GraFix-apo	0.17	+5	3	Cu/Rh R 0.6/1 & R 1.2/1.3	20 mA 30”	-
GraFix-apo + detergents[1]	0.5	+5	3	Cu/Rh R 0.6/1	25 mA 1’	-
GraFix-apo	0.13	0	1	Cu/Rh R 0.6/1	-	Dataset_1
GraFix-ADP	1	0	1	UltrAuFoil R 0.6/1 & R 1.2/1.3	20 mA 3’	Dataset_2
GraFix-ADP	0.8	0	2	UltrAuFoil R 0.6/1 & R 1.2/1.3	20 mA 3’	Dataset_3
GraFix-ADP	N/A	-15	3	Cu/Rh R 0.6/1-GO & R 1.2/1.3-GO	-	Dataset_4

[1] Samples were incubated with 0.16 mM CHAPS, 0.05 mM DDM, 0.001 mM LMNG or 1 mM OG immediately before application to grid.

Table 4. List of vitrification conditions for grid preparation.

Cryoelectron microscopy, cryoelectron tomography and single particles analysis

Data acquisition parameters for cryoelectron microscopy

For the negative stain model, images were acquired in a 200 kV Tecnai G2 (FEI-Thermofisher) at 66000x nominal magnification, at a defocus range from -1.3 to -2.4 µm and a sampling rate of 2.24 Å/px. Automatic acquisition was performed with SerialEM software (Mastronarde, 2005).

Grids for cryoEM were clipped at the CNB cryoelectron microscopy facility. Images of Dataset_1, Dataset_2 and Dataset_4 were obtained in a 200 kV Talos Arctica (FEI-Thermofisher) with a nominal magnification of 120000x and spot size 10. Movies were recorded with a Falcon III detector (FEI) in counting mode (0.855 Å/px) at a defocus range from -1.5 to -3.0 µm. A total dose of 30 $e^{-}/Å^{2}$ was distributed in 60 fractions for a total exposure time of 39 s. Grid screening and automated acquisition was controlled with the EPU software (FEI-Thermofisher).

Movies for Dataset_3 were acquired at the Diamond Light Source facility (Didcot, Oxfordshire) with a 300 kV Titan Krios electron microscope (FEI-Thermofisher) operated at a nominal magnification of 120000x. Movies were recorded with a K2 Summit direct detector (Gatan), with a 20 eV slit width energy filter in counting mode (0.83 Å/px). The Volta Phase Plate was enabled for acquisition and the defocus varied from -0.6 to -0.8 µm. The total electron dose was 39.6 e^{-} in 40 fractions, giving a dose per fraction of 0.99 $e^{-}/Å^{2}$.

A list of the datasets is presented in **Table 5**:

Dataset name	**Sample (GraFix)**	**Grid type**	**VPP**	**Graphene oxide**	**Microscope**	**Number of micrographs**	**Particles picked/selected for 3D**
NS_Dataset	HspB8:Bag3:Hsp70-apo	Cu/Rh-AmC[1]	No	No	Tecnai G2 (200 kV)	390	147014/ 105590
Dataset_1	HspB8:Bag3:Hsp70-apo	Cu/Rh R 0.6/1	No	No	Talos Arctica (200 kV)	530	53291/ 47039
Dataset_2	HspB8:Bag3:Hsp70-ADP	UltrAuFoil 1.2/1.3	No	No	Talos Arctica (200 kV)	417	54184/ 20576
Dataset_3	HspB8:Bag3:Hsp70-ADP	UltrAuFoil 1.2/1.3	Yes	No	Titan Krios (300 kV)	1423	136186/ 29090

Dataset_4	HspB8:Bag3:Hsp70-ADP	Cu/Rh R 0.6/1	No	Yes	Talos Arctica (200 kV)	507	67256/ 45645

[1] Amorphous carbon-coated grid.

Table 5. List of datasets subjected to single particles analysis.

Cryoelectron Tomography

Tomograms were acquired in a Talos Arctica (FEI-Thermofisher) operated at 200 kV in lineal mode, spot size 9 and a 57000x nominal magnification. The acquisition parameters are listed in the table below **(Table 6)**. Acquired tilt-series were binned four times (7.24 Å/px). Tomograms were reconstructed and flattened with IMOD (Kremer et al., 1996).

Pixel size (Å/px)	1.81
e^-/p/s	12.57
e^-/Å/s	3.84
Total tilt dose	113
Number of tilts	41
Total dose per tilt (e^-/Å^2)	2.76
Desired fractions	7
Exposure time per tilt	0.72
Dose/fraction/tilt	0.39

Table 6. Acquisition parameters for cryoelectron tomography.

Image processing methods

All the cryoEM datasets were systematically analyzed with the same pipeline. The software used for single particle analysis was integrated in Scipion image processing framework (de la Rosa-Trevín et al., 2016). For NS Dataset, the contrast transfer function (CTF) was calculated with CTFFIND4 (Rohou & Grigorieff, 2015). Particles were automatically picked with Xmipp auto-picking (Abrishami et al., 2013). Extracted particles were normalized and downsampled to 4.48

Å/px, discarded if Zscore > 2.5 and 2D classified with Relion (Scheres, 2012). Initial models were generated from 2D class averages with EMAN2 (Tang et al., 2007). 3D classification was carried out with Relion.

For cryoEM datasets, frame alignment for beam-induced motion correction was carried out using MotionCorr2 (Zheng et al., 2017). The CTF was determined using CTFFIND4 or Gctf (Zhang, 2016) for VPP data. Images were discarded according to one of these criteria: low resolution, high astigmatism, poor ice quality and overall appearance based on visual inspection.

Particles were automatically picked from the aligned micrographs using Gautomatch (Zhang K, MRC Laboratory of Molecular Biology, Cambridge, UK) without reference and extracted with a 320 px box size. The extracted particles were normalized, downsampled to 2.4 Å/px and those particles with a Zscore > 2.5 were discarded. Then, particles were subjected to several rounds of 2D classification with cryoSPARC, limiting the resolution for the alignment to 6 Å, (Punjani et al., 2017) to discard defective particles from the datasets. Selected particles were 3D-classified with the *ab initio* reconstruction protocol in cryoSPARC, using the information up to 12 Å resolution for classification.

The atomic models for the docking were downloaded from the Protein Data Bank (PDB) and manually docked into the EM maps using USCF Chimera (Pettersen et al., 2004). PDB ID for $Hsp70_{NBD}$ was 1HX1 (chain A). $Hsp70_{SBD}$ was obtained from full length DnaK (PDB ID 2KHO). Bag3 BAG domain and WW region and HspB8 atomic models were generated from the atomic structure of Bag1 BAG domain (chain B in PDB: 1HX1), the WW region from the E3 ubiquitin ligase NEDD4L (2MPT) and Hsp16.9 (1GME) with SWISS-MODEL (Waterhouse et al., 2018).

RESULTS

RESULTS

Optimization of protein purification protocols enabled the production of proteins with high purity

Sample purity has been shown to be of paramount importance for successful structural determination by cryoEM. For this reason, protocols for protein purification were set up to obtain high purity preparations of the HpsB8:Bag3:Hsp70 complex components.

A protocol for Hsp70 purification was already established in our lab, consisting of a nickel-charged IMAC to retain the proteins through its N-terminal His-tag, followed by a second purification step with a SEC (Quintana-Gallardo et al., 2019). We optimized the existing protocol with an extra chromatography with heparin resin. This extra purification step allowed us to partially separate the oligomeric and monomeric species of Hsp70 and to remove the proteolyzed population **(Figure 11.A)**. The oligomeric state of Hsp70 that eluted in each peak was examined by SEC. Fractions corresponding to the first peak (input A, underlined with solid black line) and the second one (input B, dashed line) were independently concentrated and loaded onto a Superdex 200 HiLoad **(Figure 11.B)**. Input A eluted as a single peak preceded by a small shoulder of dimer, whereas input B showed similar amounts of monomeric and dimeric forms. The species distribution is corroborated by Blue Native-PAGE **(Figure 11.C)**.

As the reversibility character of this Hsp70 dimeric form is not yet clear, the dimer peak was avoided in order to reduce the potential heterogeneity for future applications. The dimer formation was concentration-dependent and distinguishable over 1 mg/ml, so we avoided concentrating Hsp70 over 2 mg/ml. The effect of the extra purification step compared to the previous protocol is shown in **Figure 11.D.**

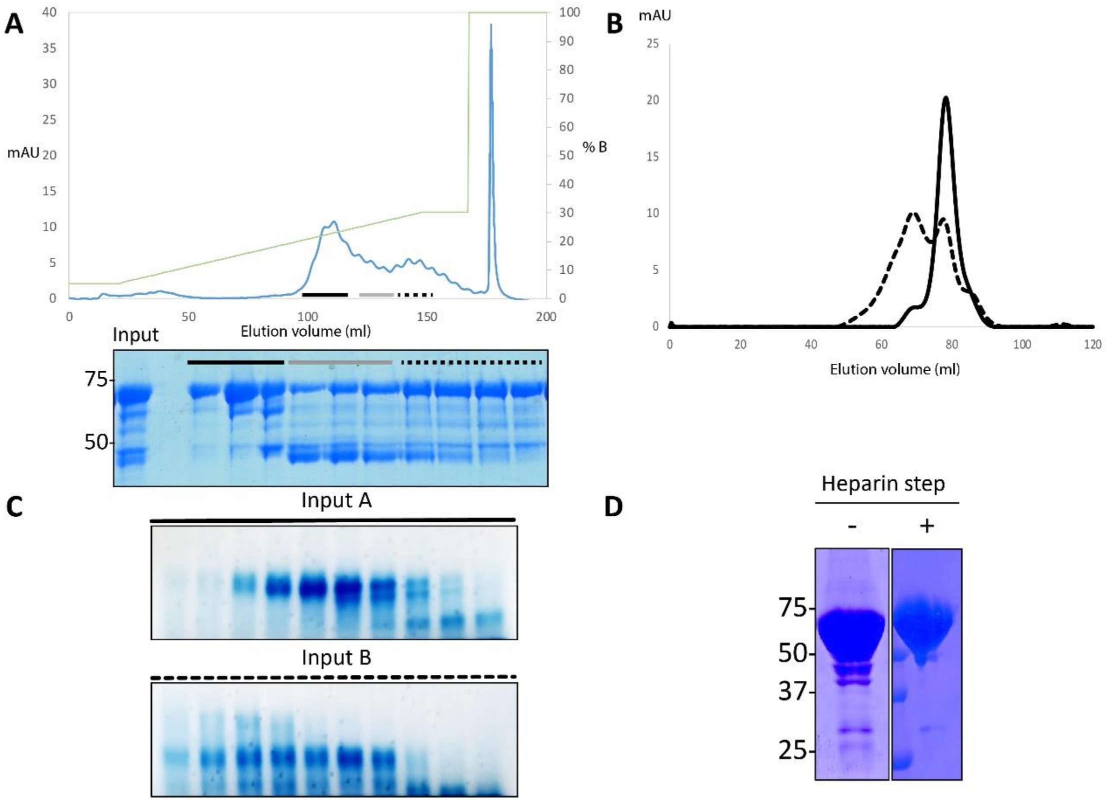

Figure 11. Optimization of the purification protocol for Hsp70. (A) *Analysis of the fractions eluted in the IEX chromatography. The green line indicates the percentage of Buffer B IEX-Hsp70 along the gradient. The blue line is the absorbance of the eluted proteins. Underlined fractions were examined by SDS-PAGE.* ***(B)*** *Fractions marked with black bar (input A) and dashed bar (input B) were concentrated and analyzed by SEC.* ***(C)*** *Native-PAGE of fractions from (B) of showing the presence of higher oligomeric species.* ***(D)*** *Comparison of the effect of the IEX step on the purity of His-Hsp70. Aliquots of two His-Hsp70 purifications after the final SEC without and with the previous heparin chromatography.*

The main drawback during Bag3 purification was its tendency to undergo degradation, which could be seen by WB from the initial lysates **(Figure 12.A)**. As a result, proteolyzed polypeptides bearing the N-terminal His-tag also bound to the Ni^{2+} resin in the first IMAC, had their tag cleaved and consequently eluted together with the full-length Bag3 when digested with TEV protease. This issue was overcome by introducing an anion exchange chromatography (HiTrap Q) in the purification protocol. The IEX step was useful to retain a considerable amount of degraded species, visible after comparing the 2nd IMAC output with IEX FT and output in **(Figure 10)**. The resulting output had a faint smear that was even fainter after a final SEC **(Figure 12.B)**.

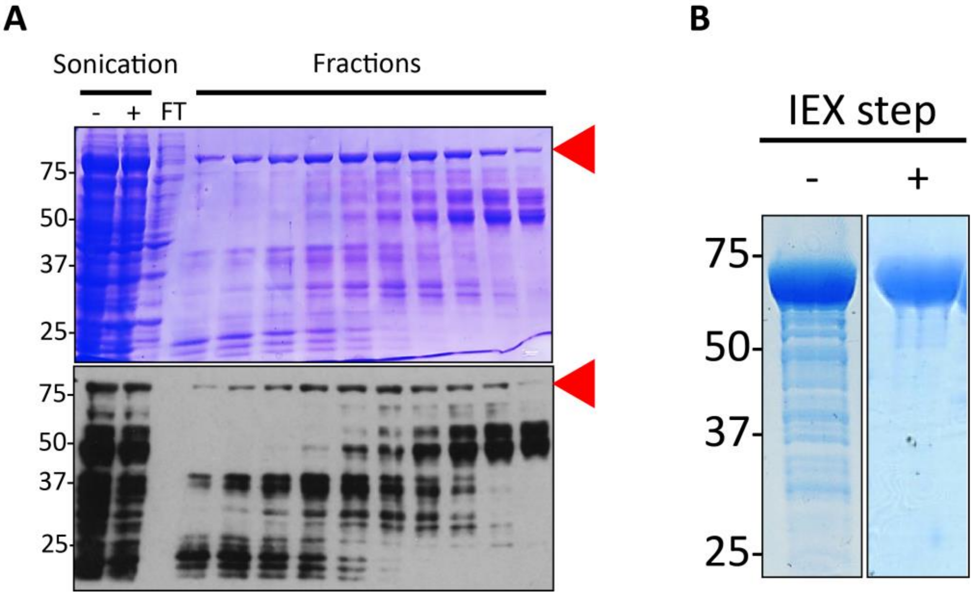

Figure 12. The effect of an IEX step on Bag3 purification. (A) *Fractions from an IMAC step, including cell content before and after lysis by sonication, were analyzed by SDS-PAGE (upper panel) and WB (lower panel).* ***(B)*** *Comparison of the SEC output from two independent purification experiments with or without the IEX chromatography at pH 7.4. FT: Flow-through.*

Small Hsp exist in high-order oligomeric species, with assemblies of up to 48 subunits (Haslbeck & Vierling, 2015). However, the oligomerization state of HspB8 has been poorly studied. We observed a concentration dependent effect on the elution volume when several input concentrations of HspB8 were loaded **(Figure 13.A)**. Increasing input concentrations resulted in a peak shifting to a higher molecular mass in the elution volume, consistent with a equilibrium of monomer (21.7 kDa) and dimer (43.4 kDa), where an increasing proportion of dimer contributed to displace the peak to lower retention volumes. Complementary to this, sedimentation velocity experiments with analytical ultracentrifugation (SE-AUC) also showed a slight but distinguishable peak with at S= 4.1-4.5 **(Figure 13.B)**. To confirm these observations, we carried out sedimentation equilibrium experiments. In sedimentation equilibrium, the sample is centrifuged at low speed with the aim of equalizing diffusion and centrifugation forces. Under these conditions, a concentration gradient of protein is formed along the cell, which depends only on the molecular weight of the species in solution. The distribution can be modelled, so the result is a weight-average molecular weight (MW_W) of the different species in solution. We tested the same concentrations as for SV-SEC, 9 and 18 µM. At 9 µM, the MW_W was similar to the one calculated from the amino acid sequence **(Figure 13.C)**. The MW_W at 18 µM was 24.36 kDa, compatible with 86.3% monomer and 13.7% dimer, which confirmed the coexistence of dimeric HspB8 in solution. Both SV-AUC and SE-AUC experiments were also performed in the presence of reducing agents in buffer. The oxidative state of HspB8 had no influence on the oligomerization state. Altogether, these studies suggest that HspB8 exists mainly as a monomer, and that increasing concentrations induces a certain dimerization, detectable at concentrations over 9 µM.

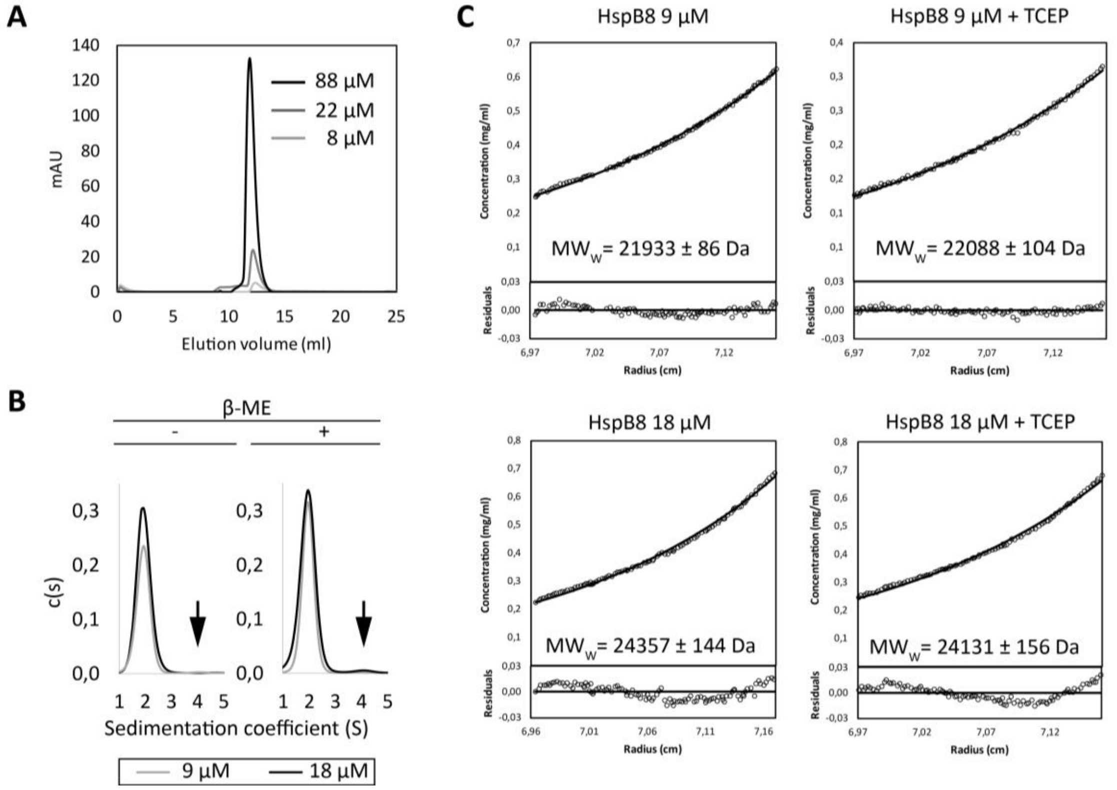

Figure 13. Study of oligomerization state of HspB8. (A) *SEC of HspB8 at several concentrations. Elution volumes were 12.32 (9 µM), 12.11 (20 µM) and 11.82 ml (88 µM).* ***(B)*** *SV-AUC at 9 and 18 µM in the presence or absence of β-ME.* ***(C)*** *SE-AUC of HspB8 in similar conditions as in (B), with TCEP instead of β-ME as reducing agent. TCEP is more stable over time than β-ME and does not absorb at 280 nm, so it does not interfere with protein absorbance measurements. Residuals plots below each graph indicate the deviation of each point respect to the fitted curve.*

Characterization of the HspB8:Bag3:Hsp70 complex by analytical size exclusion chromatography

First, we studied the interaction between HspB8 with Bag3, Bag3 with Hsp70 and Hsp70 with HspB8. The corresponding proteins were incubated and loaded onto a Superdex 200 Increase, and eluted fractions were examined by SDS-PAGE. For each pair, the individual components were loaded independently as controls. The Bag3:Hsp70 complex eluted as a single peak of higher apparent MW at 11.13 ml, whereas Bag3 and Hsp70 eluted at 11.90 and 14.19 ml, respectively **(Figure 14.A)**. The presence of both proteins in the peak was corroborated in the gel.

HspB8:Bag3 eluted as a single broader peak with the same retention volume as Bag3 alone (11.96 vs 11.90) despite the extra molecular mass provided by HspB8 **(Figure 14.C)**. Both proteins were detected in the peak fractions.

In contrast, HspB8 and Hsp70 eluted as two well-differentiated peaks when loaded together, confirming that they do not interact **(Figure 14.B).**

A mixture of HspB8, Bag3 and Hsp70 eluted as a single peak that contained the three proteins **(Figure 14.D)**.

In conclusion, these data confirm that HspB8 interacts with Bag3, and Bag3 interacts with Hsp70, but Hsp70 does not interact with HspB8. Therefore, Bag3 acts as a linker between Hsp70 and HspB8.

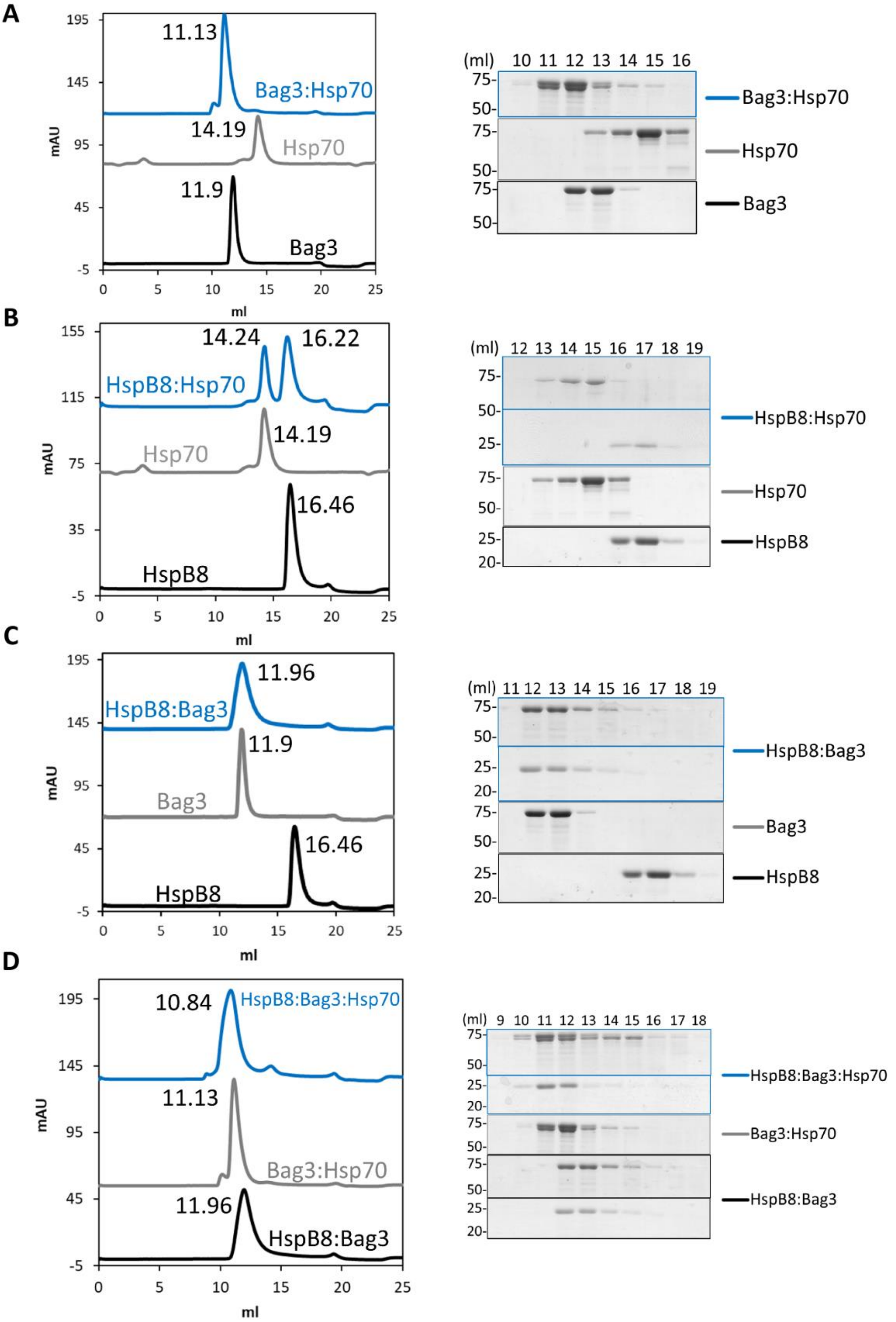

Figure 14. Analytical SEC of complexes with HspB8, Bag3 and Hsp70. *SEC of HspB8, Bag3, Hsp70 to analyze all the possible permutations:* ***(A)*** *Bag3 and Hsp70,* ***(B)*** *HspB8 and Hsp70,* ***(C)*** *HspB8 and Bag3.* ***(D)*** *HspB8, Bag3 and Hsp70 form a ternary complex. The binary complexes*

Bag3:Hsp70 and HspB8:Bag3 were used as controls. Elution volumes are shown next to the peaks.

The interaction between HspB8 and Bag3 was studied in more detail. The stoichiometry of the interaction, measured by ITC, is of 2 HspB8 per 1 Bag3 molecule (Rauch et al., 2016a). In other works, SV-AUC and crosslinking experiments showed that HspB8 and Bag3 formed more than one species, suggesting that HspB8:Bag3 form complexes of variable stoichiometry depending on the relative abundance of both components (Shemetov & Gusev, 2011). We run SEC of the HspB8:Bag3 complex incubated at 1:1, 2:1, 3:1 and 4:1 ratios. All HspB8 interacted with Bag3 when incubated at 1:1 and 2:1 ratios **(Figure 15.A-B)**. Unbound HspB8 was detected only in ratios 3:1 and 4:1 **(Figure 15.C-D)**. The results of SEC experiments at different ratios support a 2:1 stoichiometry for the HspB8:Bag3 complex.

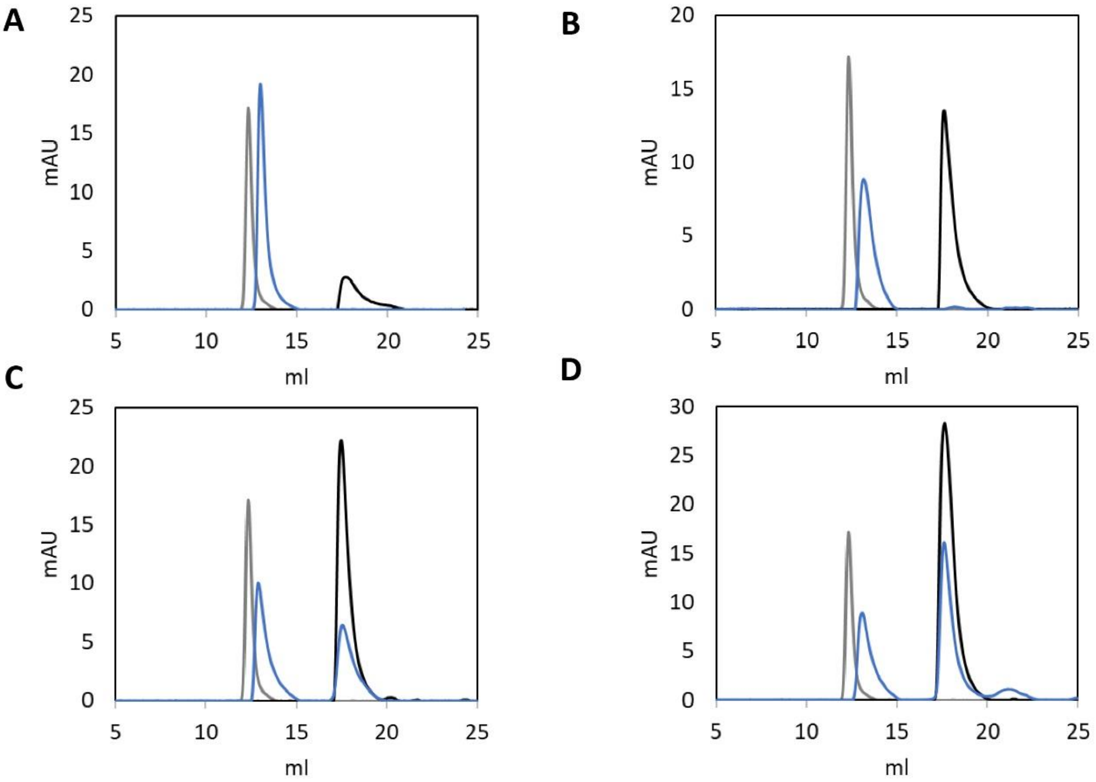

Figure 15. SEC of the HspB8:Bag3 complex incubated at several ratios. *The interaction HspB8:Bag3 was studied at several ratios, 1:1* ***(A)****, 2:1* ***(B)*** *3:1* ***(C)*** *and 4:1* ***(D)****.*

The interaction of HspB8 and Bag3 entails changes in secondary structure

Interestingly, despite the MW_{Bag3} being lower (61.6 kDa) than $MW_{His\text{-}Hsp70}$ (72.1 kDa), Bag3 eluted earlier. Also, the HspB8:Bag3 interaction was not accompanied by a lower elution volume. These differences in the hydrodynamic behavior could be explained by the degree of order in the structure of Bag3. To test this, we subjected the three proteins to CD with a double purpose, first to check the structural integrity of the complex components by comparing their CD spectra with the structural information in literature; and second to correlate this structural information with their behavior in solution.

Random coil sequences typically display a negative band near 195 nm, while α-helical proteins have negative bands at 208 and 222 nm (Greenfield, 2006). Bag3 CD spectrum shows a minimum at 200-205 nm and a faint negative band at 225 nm. This spectrum is compatible with an unstructured protein with certain contribution of α-helices. Indeed, the crystal structure of the BAG domain **(Figure 5.D)** consists of a bundle of 3 α-helices and Bag3 has been previously described as an intrinsically disordered protein (Shemetov & Gusev, 2011). These particularities in Bag3 structure would be responsible for its apparent molecular weight in SEC.

The HspB8 spectrum also had a minimum at 205 nm and a broad signal at around 215 nm, which indicates random coil with influence of secondary structure elements (β sheet in the case of HspB8) that displace the 195 nm peak to higher wavelengths. The spectrum also shows a small peak at 228-300 nm, which can be attributed to disulfide bonds or aromatic residues.

The fact that HspB8:Bag3 eluted like Bag3 could be an indicative of acquisition of structure upon interaction that compensates for the gain of MW. We studied this interaction by exploiting the additive character of CD spectra. The comparison of HspB8:Bag3 spectrum with the sum of HspB8 and Bag3 spectra recorded independently showed differences in secondary structure **(Figure 16.B)**. The exact nature of the change is revealed by the differential spectrum, which indicates that the interaction is accompanied by a gain in β-structure and/or a loss in random coil contribution **(Figure 16.C)**. β-strand containing proteins are characterized by a positive band near 195 nm and a negative band near 215 nm. This reduced disorder associated to a conformational change would compensate the peak displacement expected in SEC by the extra molecular mass from HspB8 when both proteins are loaded.

The Hsp70 spectrum presents secondary structure elements of α-helices and β-strands, in agreement with the structures obtained by X-ray crystallography and NMR **(Figure 2.B)**, which confirms that His-Hsp70 conserves its folded state after purification.

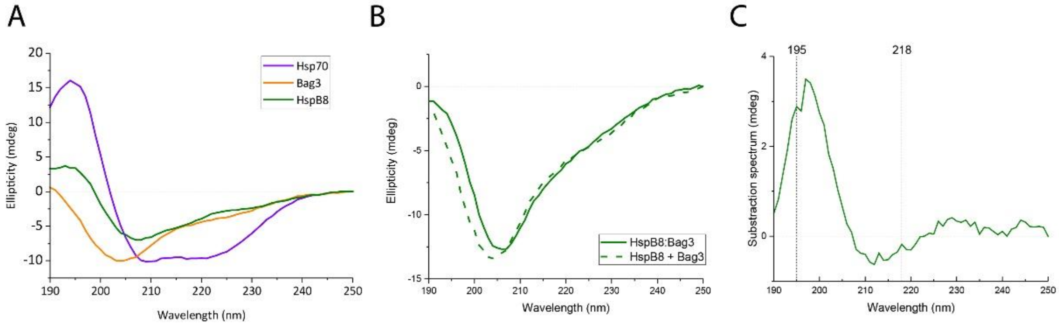

Figure 16. CD spectra of HspB8, Bag3 and Hsp70. (A) *Far-UV spectra of HspB8 (18 µM), Bag3 (7 µM) and Hsp70 (7 µM).* ***(B)*** *Comparison of the HspB8:Bag3 CD spectrum against the added spectra of HspB8 and Bag3.* ***(C)*** *Differential spectrum resulting from the subtraction of HspB8 and Bag3 spectra from HspB8:Bag3 spectrum.*

Characterization of the HspB8:Bag3:Hsp70 complex by sedimentation velocity analytical ultracentrifugation

To confirm the SEC results, HspB8, Bag3 and Hsp70 were subjected to sedimentation velocity analytical ultracentrifugation. SV-AUC is not only a powerful method to characterize macromolecular solutions even in the case of transient interactions, but it also provides useful information on the global size and shape of the different species in solution.

Bag3 sedimented as a single peak with S= 2.5. HspB8 separated in two peaks, a main one corresponding to the monomer (1.9 S, 98.4%) and a minor one consistent with a dimer (4.1 S, 1.6%). As shown before, the HspB8:Bag3 interaction yielded a main peak at 4.4 S and a small one at 6.2 S **(Figure 17.A)**. This interaction also produced other minor peaks at 8.8 S, 12.1 S and aggregates that sedimented at higher S values (not shown). Therefore, HspB8 and Bag3 form a binary complex as a main species and a mixture of denser populations that were undetected by SEC. Unlike SEC, SV-AUC experiments show differences in the hydrodynamic behavior of Bag3 and HspB8:Bag3.

Hsp70 was incubated with a molar excess of Bag3 and a peak at 4.4 S was detected. The unbound Bag3 sedimented as the control **(Figure 17.C)**. As in SEC, HspB8 did not form a detectable complex with Hsp70 **(Figure 17.B)**. Finally, HspB8:Bag3:Hsp70 produced a peak of 5.6 S **(Figure 17.D)**. Due to the molar excess of HspB8 and Bag3, another peak at 4.6 S was detected, which overlaps with the control HspB8-Bag3. Approximately the 45% of the sedimented species were aggregates.

In conclusion, our SV-AUC experiments confirmed the observations of analytical SEC relative to the formation of the Hsp70:Bag3:HspB8 complex.

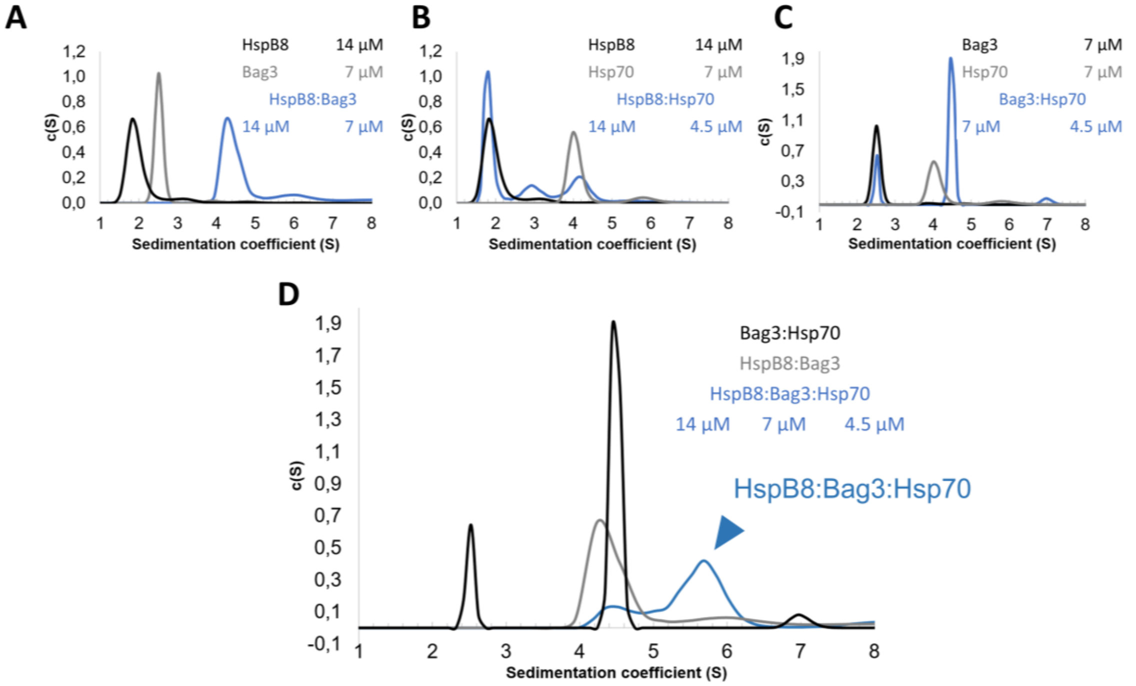

Figure 17. SV-AUC of HspB8, Bag3 and Hsp70. *SV-AUC experiments with HspB8, Bag3, Hsp70:* ***(A)*** *HspB8:Bag3,* ***(B)*** *HspB8 and Hsp70,* ***(C)*** *Bag3:Hsp70.* ***(D)*** *HspB8, Bag3 and Hsp70 formed a ternary complex. Binary complexes Bag3:Hsp70 and HspB8:Bag3 were used as controls.*

ProteoPlex assay for optimization of buffer conditions

The structure determination of purified macromolecular complexes is often problematic due to suboptimal buffer conditions. This issue can be addressed by searching stabilizing buffer conditions. There are techniques to measure the effects of ligands or buffer components on protein stability, like differential scanning fluorimetry (DSF). DSF is a fluorescence-based assay that monitors protein unfolding as it is subjected to an increasing gradient of temperature. A higher melting temperature (T_m) under certain ligand or buffer conditions correlates with a higher protein stability under such conditions. Although useful for single-chain proteins, DSF works poorly with multidomain proteins or multiprotein complexes because the overlay of the unfolding events of the individual components hampers data interpretation and accurate T_m estimation.

ProteoPlex is a screening method based on DSF, which combines an automated high-throughput screening of buffer components (pH and small molecules) with a new mathematical model to interpret the unfolding curves of macromolecular complexes and infer its thermodynamic parameters (Chari et al., 2015).

We subjected the HspB8:Bag3:Hsp70 complex to a ProteoPlex assay in order to find stabilizing buffer conditions that facilitated downstream applications. The multiprotein complex was screened in common buffer systems within a pH range of 5.5-9.0. The resulting unfolding curves were analyzed and the best-ranked pH conditions are shown in **Figure 18**. The T_m for each condition was calculated from the lineal stage of the curves.

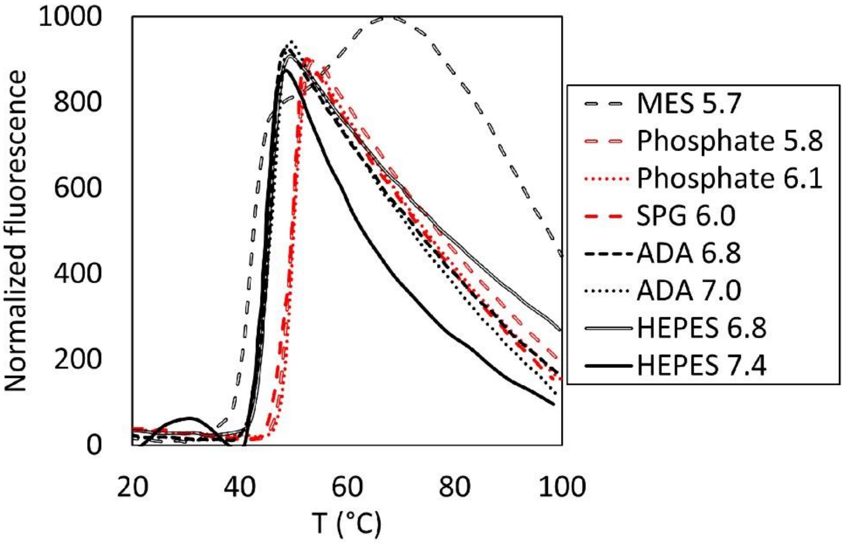

Buffer	SPG 6.0	Phosphate 6.1	Phosphate 5.8	HEPES 6.8	ADA 6.8	ADA 7.0
T_m (°C)	50.01	49.95	49.63	45.41	46.3	46.34

Figure 18. ProteoPlex assay for screening of stabilizing buffer conditions. *Top: Normalized unfolding curves of the ternary complex as a function of temperature under the indicated buffer systems. Unfolding curve in MES buffer pH 5.7 was included as an example of deviation of a two-state unfolding model. Bottom: Table with the T_m of the melting curves shown above. T_m of the reference buffer (HEPES 7.4) was not calculated.*

Analysis of the HspB8:Bag3:Hsp70 complex by cryoelectron microscopy

Cryoelectron microscopy of the HspB8:Bag3:Hsp70 complex

After a characterization of the biophysical properties of the HspB8:Bag3:Hsp70 complex, our goal was its structural characterization using cryoEM, a suitable technique for macromolecular complexes capable of solving structures of a wide range of sizes and structural complexity.

Since HspB8, Bag3 and Hsp70 formed a stable ternary complex in SEC, our first approach to prepare the sample for cryoEM was the vitrification of the ternary complex isolated from the SEC experiment. For cryoEM, we used the untagged Hsp70 to avoid a potential interference of the N-terminal tag in the structure determination. The SEC of the complex was performed in a FPLC system optimized to minimize sample dilution, since protein interactions might result affected by dilution.

SEC performed immediately before sample vitrification showed a defined peak for the ternary complex, with no signs of aggregated material **(Figure 19.A)**. The eluted complex was subjected to cryoEM after incubation in four nucleotide states: absence of nucleotide (apo-state), ADP, ATP and with the non-hydrolyzable ATP analogue AMP-PNP. The nucleotide state induces conformational changes in Hsp70 that could affect complex stability and/or reveal structural features that make SPA more feasible.

A standard glow-discharged grid support made of Cu/Rh with carbon foil was used as a starting point. Under the microscope, particles of variable sizes, ranging from aggregates to small particles corresponding to disassembled components, were visible in variable extents regardless of the nucleotide state **(Figure 19.B-D).**

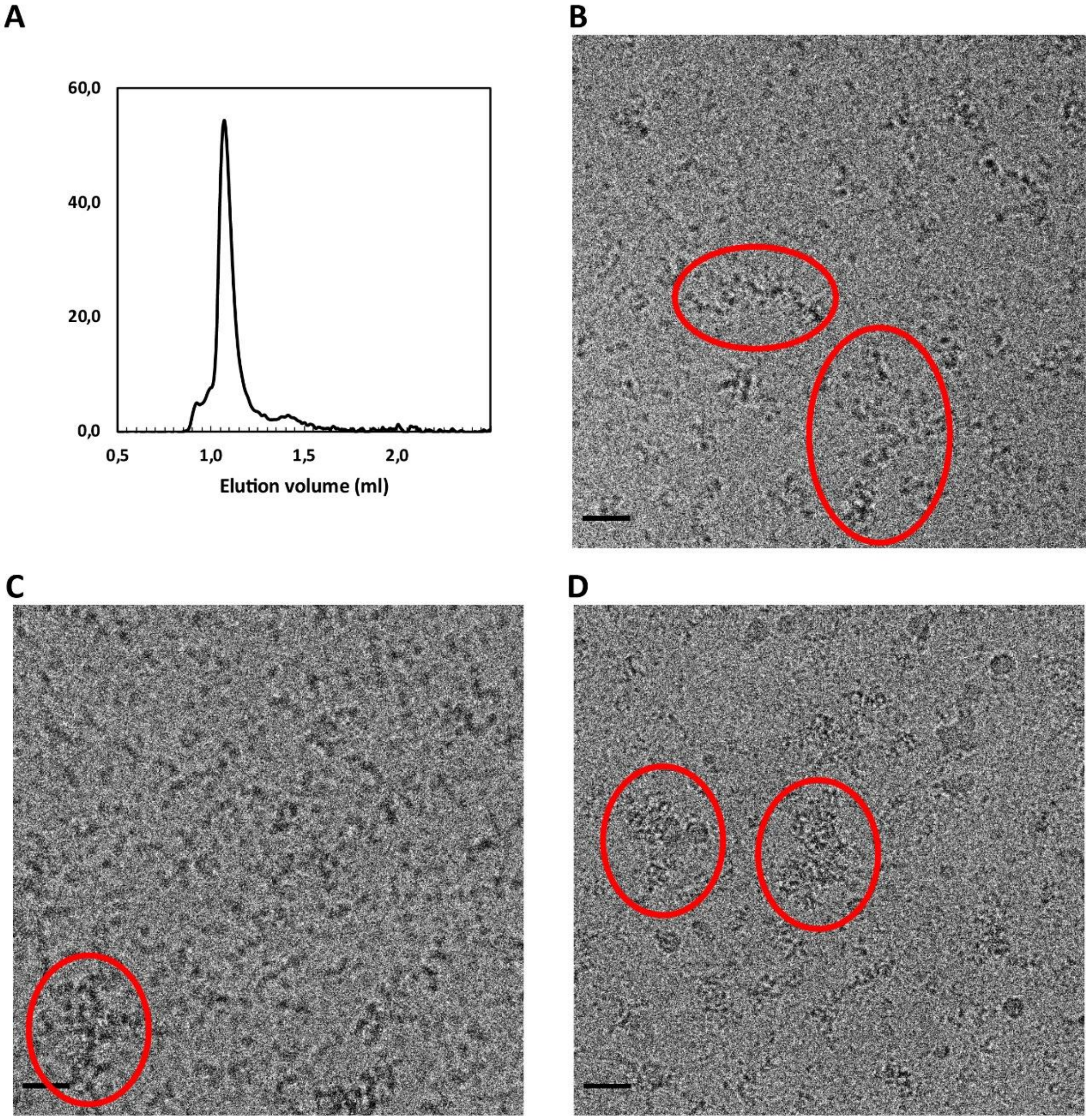

Figure 19. Cryoelectron microscopy of the HspB8:Bag3:Hsp70 complex. (A) *SEC chromatography of the HspB8:Bag3:Hsp70 complex shows a sharp peak. Fractions containing the peak maximum were subjected to cryoEM after incubation with different nucleotides. Micrographs of the ternary complex in the apo-state **(B)**, ADP state **(C)** and AMP-PNP state **(D)**. Red circles indicate protein aggregates. Scale bar: 320 Å.*

In order to understand the behavior of the complex upon vitrification, the HspB8:Bag3:Hsp70 complex in the apo-state was subjected to cryoelectron tomography (cryoET). CryoET allows the 3D reconstruction of the ice layer in a grid hole, so it provides information on particle distribution and ice thickness that is absent in the 2D micrographs.

The tomogram showed that the particles were distributed forming concentric rings along the z-axis **(Figure 20.A)**. The particle distribution pattern suggests that the ice layer adopted the shape of a concave meniscus in the grid hole. Based on the signal provided by the particles, we were able to define a 2D curve that was computationally levelled so that all the particles lay in the same plane. This change was applied to the rest of the planes in the tomogram in a process known as tomogram flattening **(Figure 20.B)**.

The artificial flattening allowed us to assess the particle distribution along the z-axis. If a random particle distribution across the ice were assumed, particles would be expected to distribute evenly all along the z-axis. However, after artificial flattening of the tomogram, particles were only found in a single plane in the z-axis **(Figure 20.B)**. Planes spaced 20 nm from the latter showed no particles within the ice layer. We assume that this pattern corresponds to particles adsorbed to the air-water interface (AWI). The contact with interfaces can result in complex dissociation and protein denaturation, and could also be responsible for aggregation (Drulyte et al., 2018).

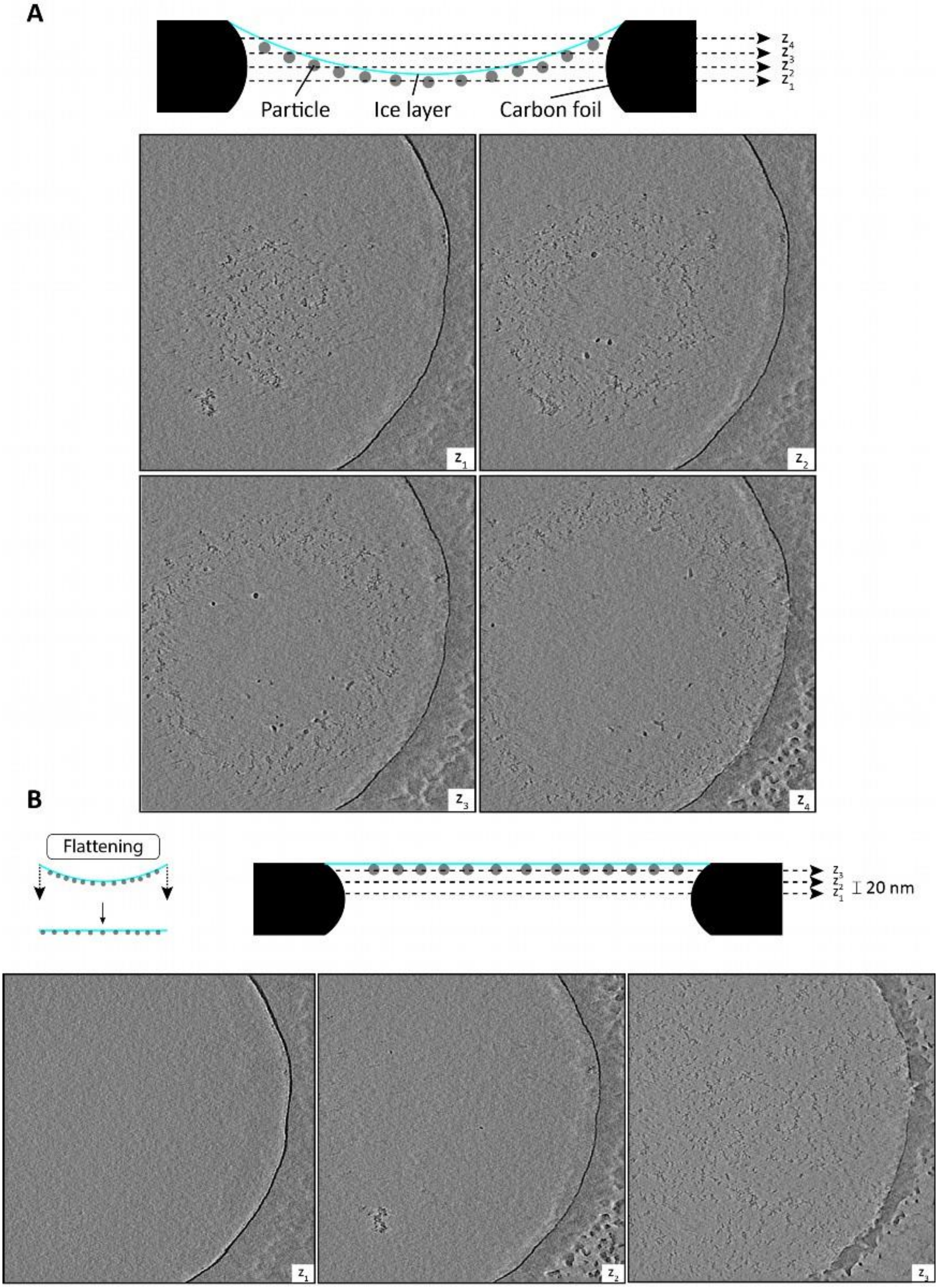

Figure 20. CryoET of the ternary complex in a Cu/Rh R0.6/1 grid. (A) *Top: diagram of the grid hole showing the meniscus of one surface of the ice layer, particles potentially adsorbed to the air-water interface and planes. Bottom: Tomogram planes along the z-axis showing potential particle distribution in the meniscus.* ***(B)*** *Top: schematic representation of tomogram flattening.*

Bottom: Flattened tomogram displayed in (A) at three positions in the z-axis. Planes are spaced 20 nm each other.

Complex stabilization by the GraFix method to prevent dissociation of its components

Some proteins tend to adsorb to air-water interfaces when in close contact with them (Trurnit, 1960). Thus, some of the complex components can be sensitive to the interaction with interfaces, causing them to disassemble and/or unfold, which severely compromises structural determination (D'Imprima et al., 2019). A suitable alternative for the preparation of transient macromolecular complexes that disassemble when vitrified is the chemical fixation of the subunits with crosslinkers.

Crosslinkers are linear molecules with two reactive groups connected by a spacer arm of constant length (i.e. 8-12 Å, depending on the crosslinker). They covalently react with functional groups of amino acids, often ε-amines of lysines, which remain within the arm distance, turning the interaction irreversible. The GraFix method (Stark, 2010) combines a centrifugation in a density gradient with an increasing glutaraldehyde gradient for isolation of crosslinked macromolecular complexes. Moreover, the mild fixation conditions prevent artifacts and aggregation due to inter-complex crosslinking, and it allows the isolation and stabilization of homogeneous populations of macromolecules.

A mixture of HspB8, Bag3 and Hsp70 was subjected to the GraFix procedure and fractions from the gradient were analyzed to identify those containing the ternary complex. A mixture of molecular species, including unbound protein, complete and partial complexes and aggregates was obtained **(Figure 21.A)**. A defined band with an apparent MW between 150-250 kDa was identified, consistent with the MW of the complex with a stoichiometry of 2:1:1 (HspB8:Bag3:Hsp70, 175.1 kDa), as it has been reported previously for HspB8 bound to Bag3 (Rauch et al., 2016a; Shemetov & Gusev, 2011) **(Figure 15)**. The presence of HspB8, Bag3 and Hsp70 in this band was confirmed by mass spectrometry. The advantage of GraFix compared to the direct application of crosslinkers is the separation of the different species along the density gradient. Gradient centrifugation allowed us to isolate the ternary complex, with a minimum presence of other species **(Figure 21.B)**. The reduction of compositional heterogeneity is crucial to facilitate further single particle analysis.

Negative staining is a rapid method to assess the state of an isolated sample in solution by its visualization under the microscope. It can be used to easily evaluate the sample homogeneity and its size. A fraction containing the ternary complex was imaged using a standard negative staining technique, and a homogenous sample with discrete particles of uniform size between 10-20 nm was observed **(Figure 21.C)**.

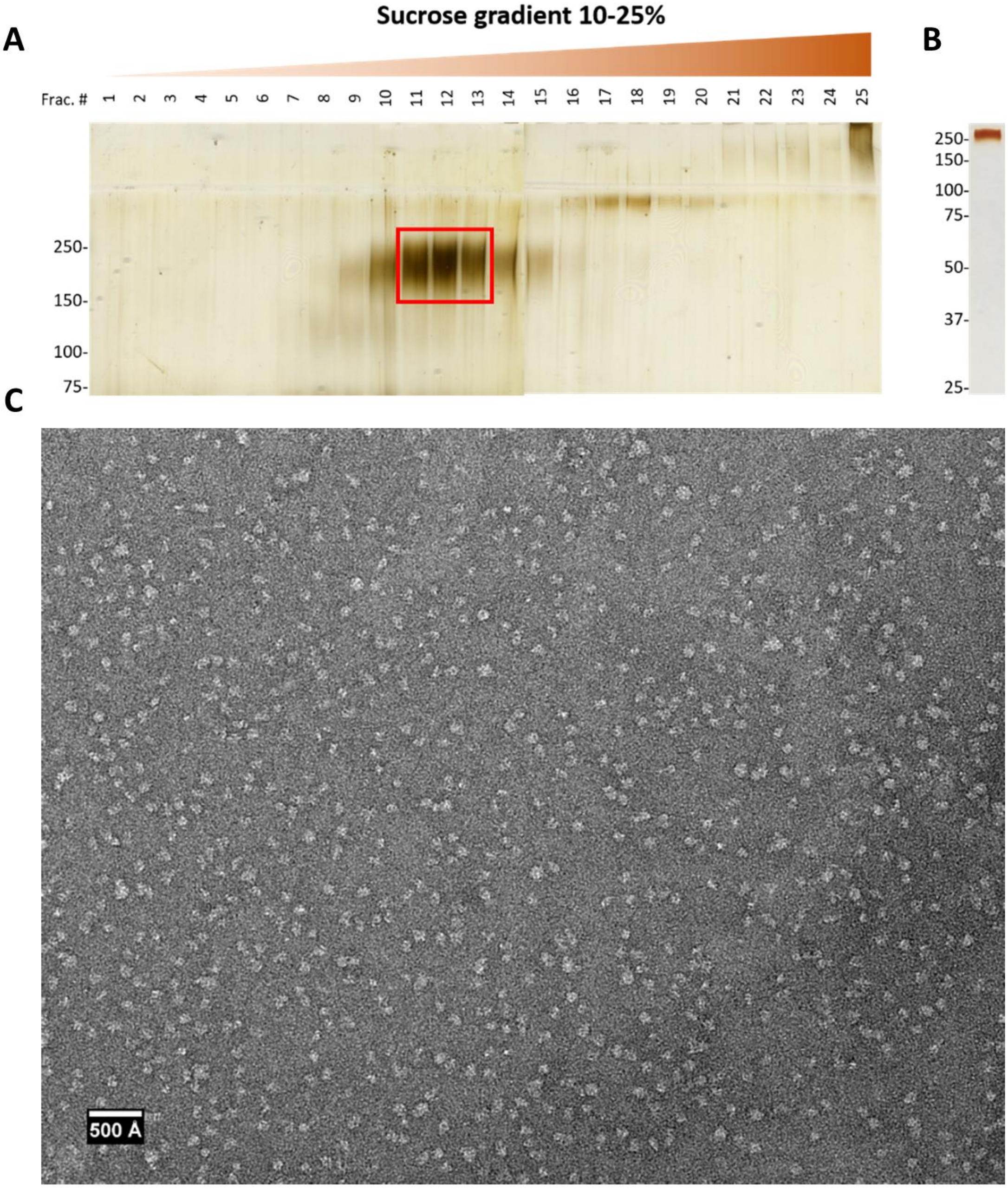

Figure 21. Complex stabilization by the GraFix method. (A) *Silver stained 6% polyacrylamide gel of the fractions from the sucrose gradient. Bands corresponding to the ternary complex are indicated with a red square.* ***(B)*** *The selected fractions were then concentrated and loaded on a*

10% gel to analyze sample purity. ***(C)*** *Negative staining of the crosslinked complex showing discrete particles of similar sizes.*

Structural analysis of the HspB8:Bag3:Hsp70 complex by negative staining

Negative staining is a standard procedure to carry out a preliminary 3D reconstruction of a specimen before moving to cryoEM. With this procedure, it is possible to obtain a low-resolution 3D model with the approximate size and shape, which can be even used as reference for cryoEM. We collected a dataset from the negative stained crosslinked complex and subjected it to single particle analysis. A 3D volume of 140 x 120 x 80 Å was reconstructed at approximately 20 Å resolution, which is limited by the size of the uranyl acetate grains **(Figure 22.A)**.

At this resolution, it was difficult to unequivocally identify any of the complex components, so the 3D model was combined with XL-MS analysis to help positioning them within the density map, in a procedure known as docking.

The ternary complex was incubated with the crosslinker BS3, digested and submitted to mass spectrometry analysis (XL-MS). BS3 possesses two reactive extremes that covalently bind to mainly ε-amines of lysine side chains that remain within a certain distance upon interaction. The distance is defined by the length of the crosslinker, which is 11-12 Å for the case of BS3. Inter-subunit crosslinked peptides can be identified by MS analysis, and by these means, the maximum distance between such peptides, and therefore between the subunits can be determined. The sum of the crosslinker arm length and the two lysine side chains determines the maximum distance between the two C_α of the crosslinked lysines, which has been stablished up to approximately 40 Å (Merkley et al., 2014).

With this information, the atomic models of the complex components can be placed inside the 3D map, arranged in such a way that the maximum atomic distances imposed by crosslinked amino acids are fulfilled. It is important to note that a crosslink between two components of the complex means that both proteins are close enough (i.e. within the space arm length range) to be crosslinked, but not necessarily implies a physical interaction between them. The crosslinking also depends on the accessibility of the reactive groups to the crosslinker.

The results of the XL-MS analysis with the inter-subunit crosslinks are shown in **Figure 22.D-E**. Nine high-quality inter subunit crosslinks were obtained, six of them between the Bag3 WW domain and Hsp70 (three with $Hsp70_{NBD}$ and three with $Hsp70_{SBD}$), and two with a region in the

HspB8 NTD, close to the ACD. Only one high-quality crosslink was found between Hsp70 and HspB8.

Subsequently, a docking of the structural motifs known for Hsp70, Bag3 and HspB8 was carried out in the 3D reconstructed volume. The atomic structures of $Hsp70_{NBD}$ and $Hsp70_{SBD}$ are known and atomic models were generated using the SWISS-MODEL server for the $Hsp70_{NBD}$:BAG domain complex with the atomic structure of the rat Bag3 BAG domain (94% identity; PDB: 1UK5) and the atomic structure of the complex between $Hsp70_{NBD}$ and the Bag1 BAG domain (1HX1). For the WW domain of Bag3, we used the atomic structure of the WW3 domain of the E3 ubiquitin-protein ligase NEDD4L (69% sequence identity with the Bag3 WW domain; PDB: 2MPT) and for HspB8, the atomic structure of Hsp16.9 (40% identity; PDB: 1GME).

In the docked model, Hsp70 displays a semi-extended conformation, where $Hsp70_{NBD}$ and $Hsp70_{SBD}$ are separated, but not as much as in the fully extended conformation shown in **Figure 2.B**. The BAG domain interacts with $Hsp70_{NBD}$ as described earlier (Sondermann et al., 2001) **(Figure 22.B-C)**.

The WW region of Bag3 crosslinked with the $Hsp70_{NBD}$, $Hsp70_{SBD}$ and the NTD of HspB8 **(Figure 22.E)**. Therefore, it was docked in a position that fulfills in most of the cases the distances imposed by the XL-MS analysis **(Figure 22.B, dashed circle)**. No interactions between the Bag3 WW region and other complex components have been described. Interestingly, the high number of crosslinks with other components suggests that the WW region occupies a core position in the complex.

After docking the BAG domain, the WW region and Hsp70 subdomains, there was still mass in the 3D model to accommodate two molecules of HspB8 and the remaining 60% of Bag3 structure, for which there is no structural information.

In conclusion, our 3D reconstruction of the negative stained-crosslinked HspB8:Bag3:Hsp70 complex is consistent with a 2:1:1 stoichiometry.

A

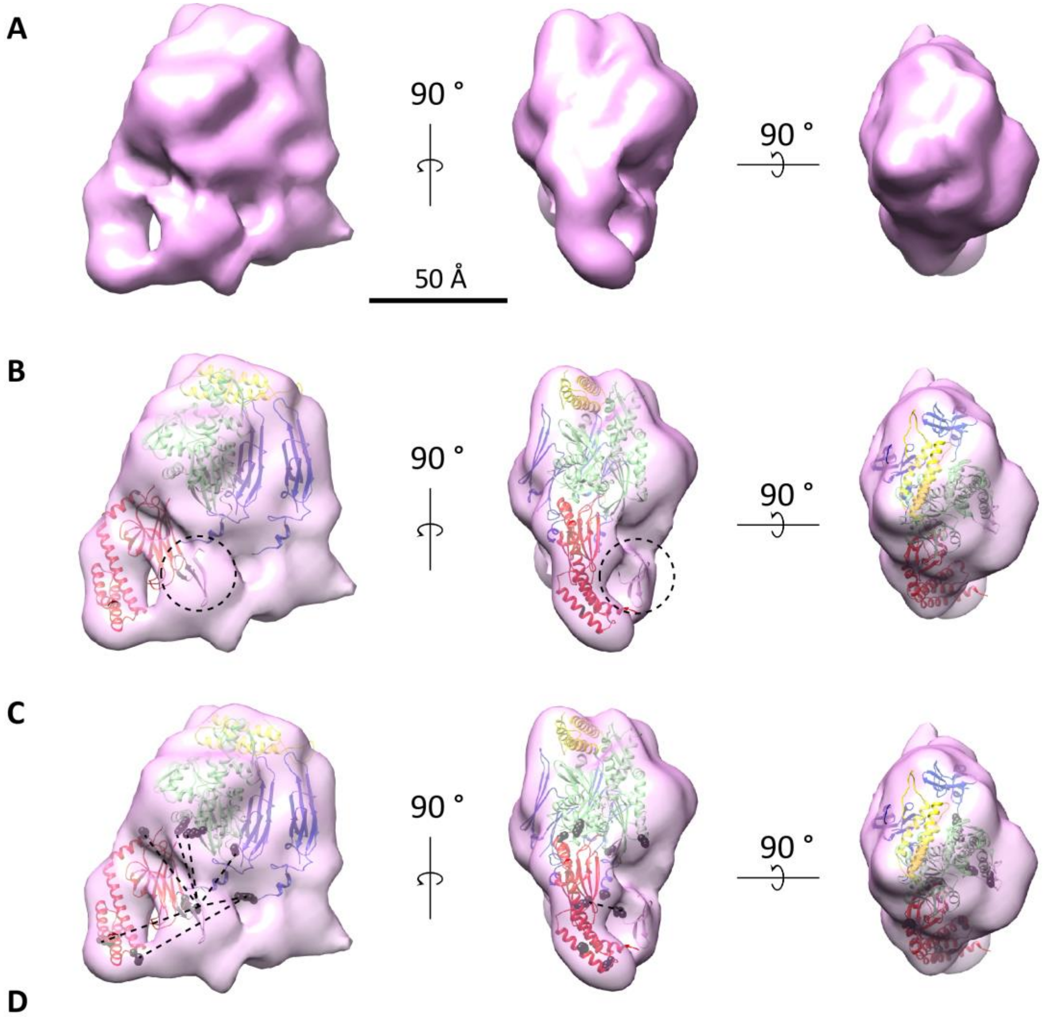

D

Hsp70	**Bag3**	**Distance (Å)**
D$_{324}$A**K**LD**K**$_{329}$	V$_{55}$PSEGP**K**ETPSSANGPSR$_{72}$	33
L$_{511}$S**K**EEIER$_{518}$	V$_{55}$PSEGP**K**ETPSSANGPSR$_{72}$	50
K$_{570}$VLD**K**$_{574}$	V$_{55}$PSEGP**K**ETPSSANGPSR$_{72}$	45
T$_{189}$G**K**GER$_{194}$	V$_{55}$PSEGP**K**ETPSSANGPSR$_{72}$	32
Q$_{157}$AT**K**DAGVIAGLNVLR$_{172}$	V$_{55}$PSEGP**K**ETPSSANGPSR$_{72}$	42
S$_{495}$TG**K**AN**K**$_{501}$	V$_{55}$PSEGP**K**ETPSSANGPSR$_{72}$	17
Hsp70	**HspB8**	
S$_{552}$AVEDEGL**K**G**K**$_{562}$	S$_{67}$GMVP**R**$_{72}$	35
HspB8	**Bag3**	
S$_{67}$GMVP**R**$_{72}$	V$_{55}$PSEGP**K**ETPSSANGPSR$_{72}$	17
G$_1$MADGQMPFSCHYPS**R**$_{16}$	V$_{55}$PSEGP**K**ETPSSANGPSR$_{72}$	>17

E

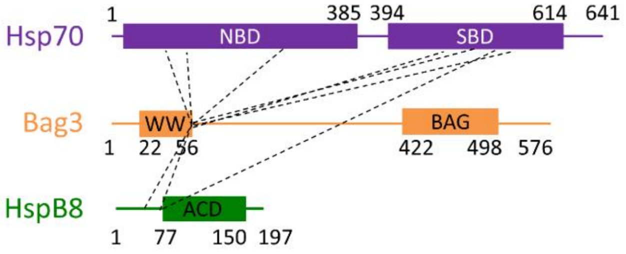

Figure 22. Negative staining model of the crosslinked HspB8:Bag3:Hsp70 complex. (A) *Three orthogonal views of the reconstructed model.* ***(B)*** *Docking of the atomic models of BAG domain (yellow), Hsp70$_{NBD}$ (green), Hsp70$_{SBD}$ (red) and HspB8 (blue) and Bag3 WW region (pink, dashed circle) in the same views as (A).* ***(C)*** *The same views as in (B), with the crosslinked peptides*

detected in XL-MS analysis denoted with dashed lines. ***(D)*** *Table with the inter-subunit crosslinks and their calculated distances between both backbones. Crosslinked lysine residues are highlighted in bold.* ***(E)*** *Schematic representation of the crosslinks with diagrams of the primary structure of Hsp70, Bag3 and HspB8.*

Cryoelectron microscopy of the fixed HspB8:Bag3:Hsp70 complex in Cu/Rh grids

After the initial structural determination of the HspB8:Bag3:Hsp70 complex using a combination of image processing of negatively stained complexes and XL-MS, we resorted to cryoEM using crosslinked complexes. CryoEM grids generally consist of a metallic (copper/rhodium, nickel, gold) mesh that supports a perforated foil with either an irregular or regular pattern of holes of variable sizes, commonly circular (Quantifoil, quantifoil.com) **(Figure 6.A)**. The foil can be made of different materials, like amorphous carbon or gold. Circular holey-foils follow an ordered pattern of holes. The diameter of the hole has an effect on the formation of the aqueous film and the distribution of the sample in the ice layer (Cho et al., 2013). We vitrified the crosslinked complex in glow-discharged Cu/Rh grids supporting a foil of amorphous carbon with a circular hole pattern of 1.2 µm diameter, spaced 1.3 µm each other (R1.2/1.3), or 0.6 µm diameter spaced 1 µm (R0.6/1). The crosslinked complex was always found in aggregates **(Figure 23.A)**. The aggregation did not depend neither on the sample concentration, since it was titrated from 0.1 mg/ml to 1 mg/ml, nor the hole size.

Following the same approach as for the native complex, we performed cryoET to study the sample distribution across the ice layer. The flattened tomogram showed that the complex tended to aggregate and accumulate in a single stratum, an indicative of adsorption to the AWI **(Figure 24)**. The fact that the negative staining showed individual evenly-disperse particles suggests that aggregation could be a consequence of the interaction with the AWI during vitrification.

A general approach to alter particle distribution in samples affected by the AWI involves the use of detergents. Detergents tend to form a layer at the interfaces, protecting the sample from the deleterious effect of AWI (Glaeser et al., 2016). We screened several detergents commonly used for cryoEM applications (CHAPS, DDM, LMNG and OG) at concentrations below the CMC, observing that the aggregating behavior was exacerbated with all the detergents tested **(Figure 23.B-E)**.

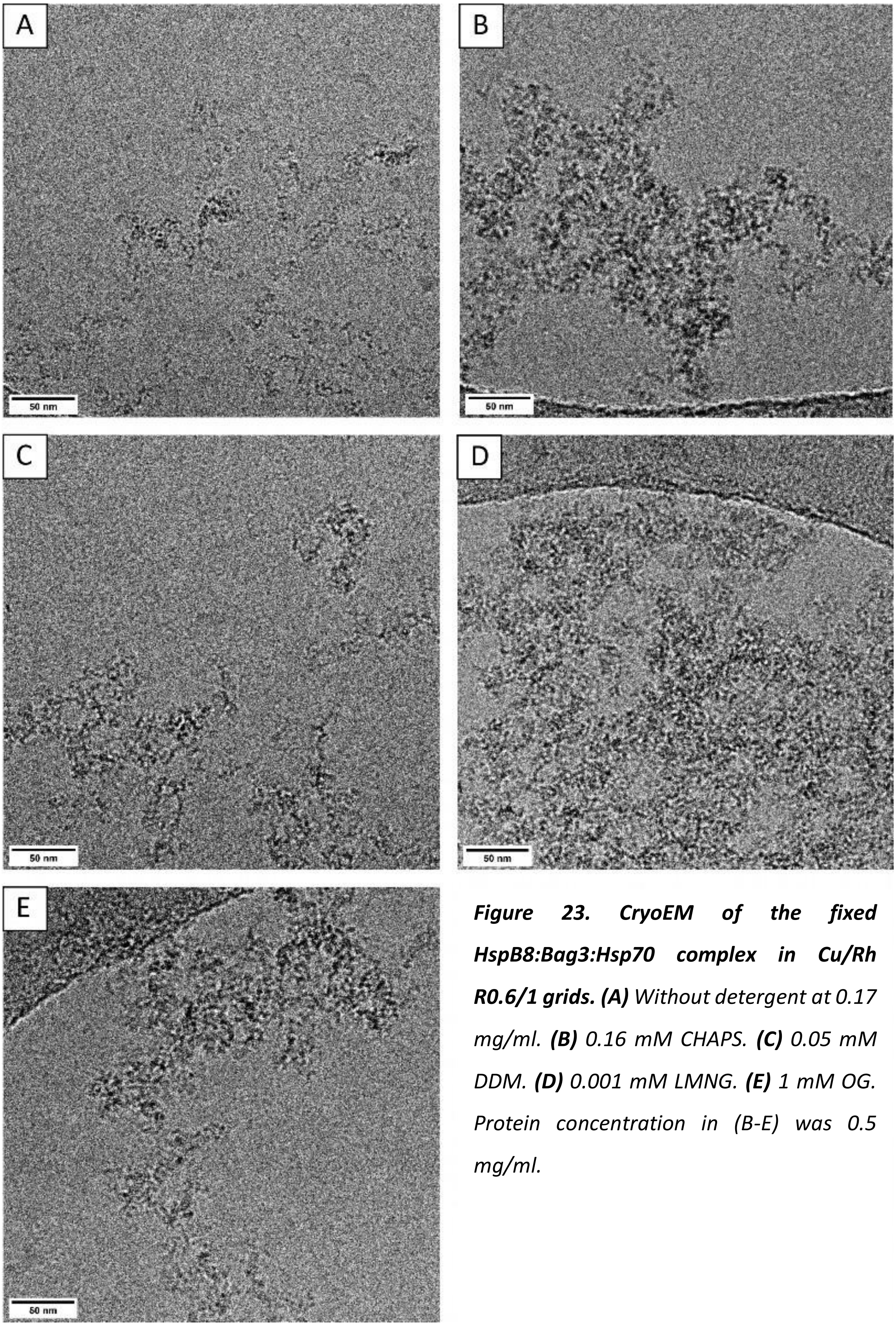

Figure 23. CryoEM of the fixed HspB8:Bag3:Hsp70 complex in Cu/Rh R0.6/1 grids. (A) *Without detergent at 0.17 mg/ml.* ***(B)*** *0.16 mM CHAPS.* ***(C)*** *0.05 mM DDM.* ***(D)*** *0.001 mM LMNG.* ***(E)*** *1 mM OG. Protein concentration in (B-E) was 0.5 mg/ml.*

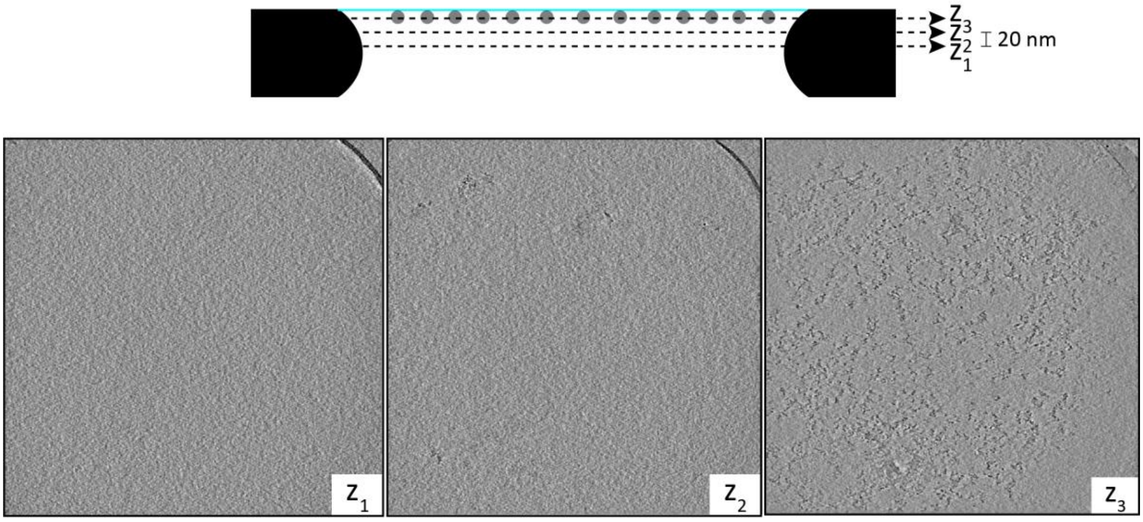

Figure 24. CryoET of the crosslinked complex in a glow-discharged Cu/Rh R0.6/1 grid. *Diagram of the flattened tomogram and three planes at different points of the z-axis.*

CryoEM grids have a hydrophobic surface that hinders the spreading of the sample drop and results in an uneven ice distribution throughout the grid. To solve this, an electrical charge is usually applied to a gas at low pressure inside a chamber where the grid stands. This gas can be either air (glow discharge) or a defined gas mixture (plasma cleaning). The charge generates ions and radicals that interact with the grid surface, rendering it hydrophilic and removing surface contamination. Since the treatment is intended for an even distribution of the sample drop throughout the grid surface, glow discharge influences particle distribution (Drulyte et al., 2018). Our previous attempts showed that the complex aggregated in glow-discharged Cu/Rh grids, so in order to explore the influence of glow-discharge on the particle distribution we vitrified the crosslinked complex in non-treated Cu/Rh R0.6/1 grids. The lack of glow discharge resulted in ice clusters that accumulated in the center of the square, too thick to be imaged and to discern individual particles. However, holes in the periphery of such clusters showed particles with minimal aggregation **(Figure 25.B)**.

A dataset was collected from this grid in a 200 kV Talos Arctica. Holes with thicker ice were avoided. Ice thickness judgment was based on the grey levels of the ice in the holes at low magnification. Movies acquired from the selected holes were subjected to SPA as described earlier **(see MATERIALS AND METHODS)**.

Particles of an approximate diameter of 120 Å were automatically picked from aligned micrographs without using references to avoid bias. They were subjected to 2D classification to remove defective particles, and those particles yielding 2D classes with dark background were re-classified until no further improvement was observed **(Figure 25.D)**. The 2D classes did not show high-resolution structural features after several rounds of 2D classifications.

The selected particles (47039) were subjected to 3D *ab initio* reconstruction in cryoSPARC, which classifies the particles and generates 3D volumes without an initial model (Punjani et al., 2017). Only the information up to 12 Å resolution was considered for the 3D reconstruction.

The size of the reconstructed volumes was compared with that generated using negative staining **(Figure 25.E)**. The comparison indicates that the 3D maps obtained from this dataset are too small to contain all the components of the complex, even considering the increment in size of the negative stain model due to the staining procedure. Both samples were prepared and verified following the same procedure, so we hypothesize that the causes of the differences in size would be situated downstream the grid preparation stage.

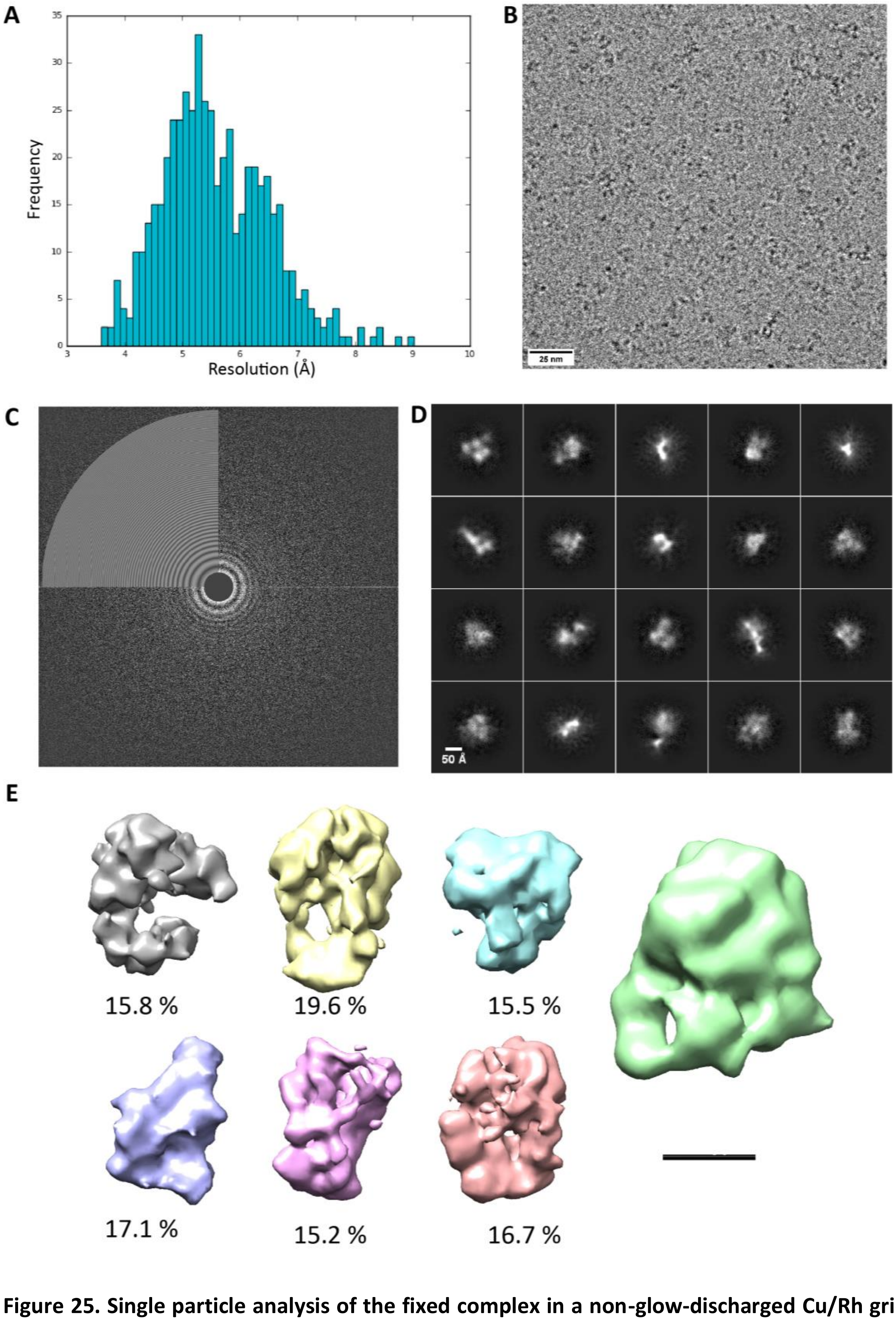

Figure 25. Single particle analysis of the fixed complex in a non-glow-discharged Cu/Rh grid. ***(A)*** *Histogram of the micrograph resolution.* ***(B)*** *Representative image of the dataset.* ***(C)*** *CTF of the selected micrograph.* ***(D)*** *Averages from 2D classification from automatically picked particles.* ***(E)*** *A gallery of 3D volumes obtained without an initial model. Particle distribution is indicated*

below the 3D models. For size comparison, the negative stain volume is shown in green. Scale bar in (E) represents 50 Å.

Cryoelectron microscopy of the fixed HspB8:Bag3:Hsp70 complex in UltrAuFoil grids

In UltrAuFoil grids, both the metal mesh and the holey foil are made entirely of gold. Such gold supports provide several advantages during specimen preparation and data acquisition. Cu/Rh and amorphous carbon have different coefficients of thermal contraction, so that when plunge freezing, the carbon shrinks less than the metallic mesh. This difference leads to a phenomenon known as "cryo-clinking", where the compressive forces on the carbon result in an increased specimen movement (Booy & Pawley, 1993). UltrAuFoil grids prevent cryo-clinking since both mesh and foil contract with the same coefficient. Gold properties also make the grid support more resistant to beam-induced movement (Russo & Passmore, 2016).

At this point, we introduced a change in the sample preparation. So far, the crosslinked complex had been prepared by the GraFix method in the absence of nucleotide. In order to produce the complex under conditions closer to the physiological ones, the complex was produced by the GraFix method with 2 mM ADP. We chose ADP because Hsp70 preserves a similar extended conformation as in the apo-state **(Figure 2.B)**. The ADP-state reduces the affinity of the Bag3:Hsp70 interaction (Rauch & Gestwicki, 2014), so we expected to have more heterogeneity during the complex formation. Indeed, the ternary complex eluted as two peaks when incubated with ADP **(Figure 26.A,C)**. The first peak contained the three components, but the second one was enriched in Hsp70, since the ratio between Bag3 and Hsp70 bands in the Coomassie-stained gel was unequal. The heterogeneity observed in SEC experiments under native conditions was also patent with the crosslinked complex, with more species appearing when the sample was prepared with ADP **(Figure 26.B,D)**.

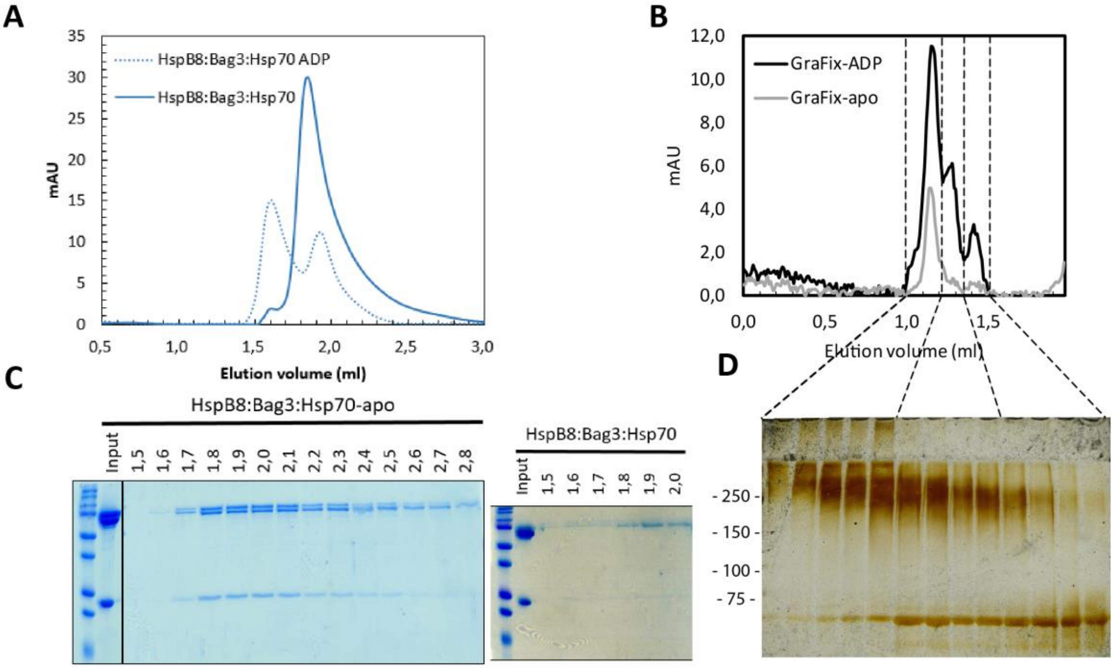

Figure 26. The influence of ADP on complex formation. (A) *SEC of the native ternary complex with and without incubation with 2 mM ADP.* ***(B)*** *SEC of the crosslinked complex with and without incubation with 2 mM ADP. Fractions from the corresponding GraFix gradient with the ternary complex were concentrated and used as input.* ***(C)*** *SDS-PAGE of the profiles in (A).* ***(D)*** *Silver-stained SDS-PAGE gel of the fractions from GraFix-ADP condition in (B).*

The same glow discharge conditions as for Cu/Rh grids were tested. We found that the majority of grid holes were empty in UltrAuFoil grids glow-discharged for 0” or 15” at 25 mA. An extended glow treatment of 3’ at 25 mA was necessary to occupy the grid holes with ice. Again, R 1.2/1.3 and R 0.6/1 holey foils were compared, and no differences were appreciated in terms of ice coverage.

With the glow discharged Cu/Rh grids, the sample aggregated independently of the concentration. Indeed, **Figure 23.A** shows aggregation in a grid prepared with 0.17 mg/ml of sample. Interestingly, the sample did not aggregate in the UltrAuFoil even at 1 mg/ml. Thus, the grid support material dramatically affected the sample solubility during vitrification **(Figure 27.B)**.

A dataset of the fixed complex with ADP in an UltrAuFoil R1.2/1.3 grid was collected in a 200 kV Talos Arctica. The average resolution of the aligned micrographs calculated by CTFFIND was lower than the dataset from the Cu/Rh grid. The micrograph resolution depends on the amount of signal of the Thon rings in the Fourier space that can be detected **(Figure 27.C)**. This signal is affected by several factors, like mechanical drift of the sample stage in the microscope or the ice thickness on the images.

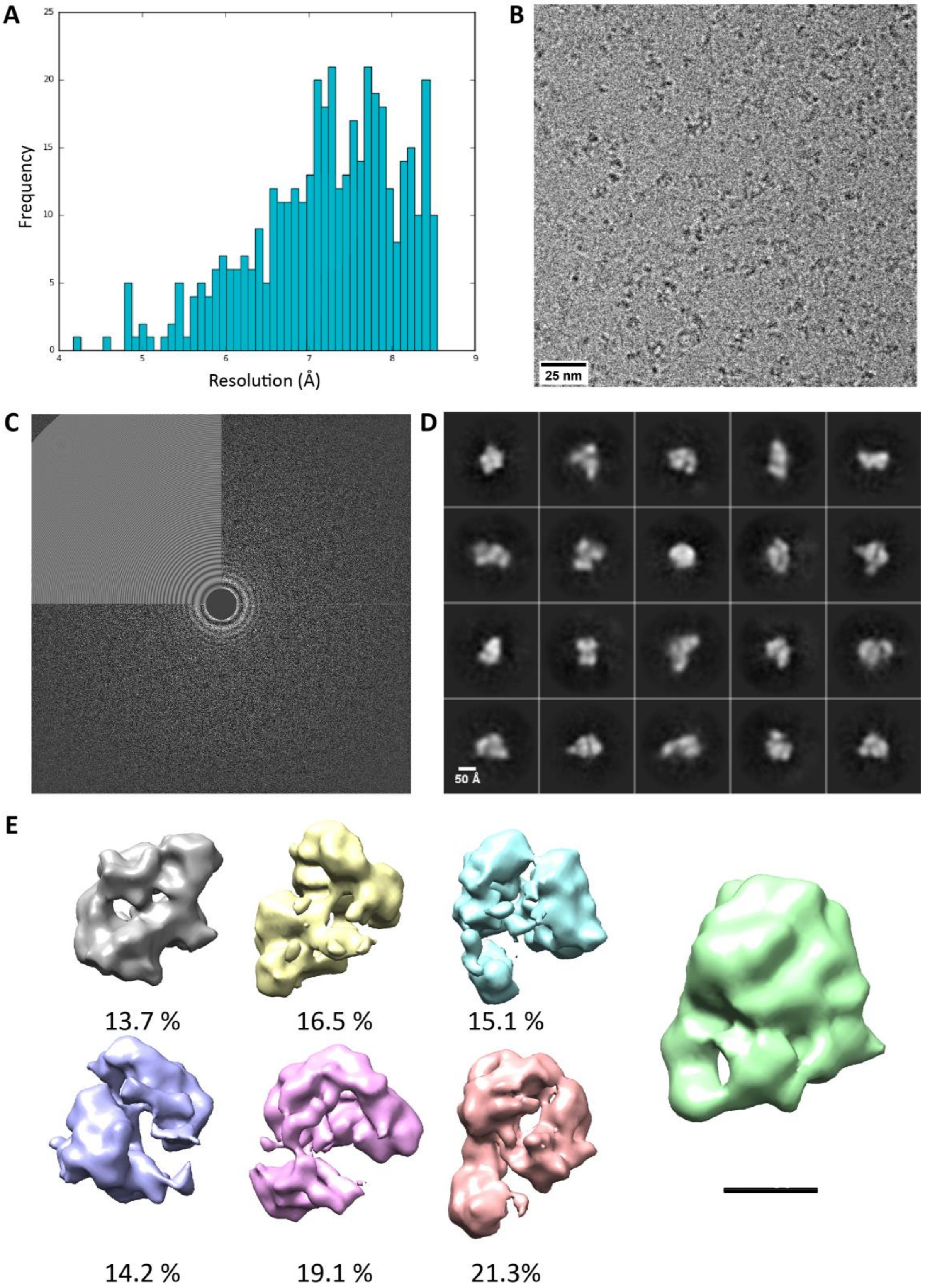

Figure 27. Single particle analysis of the fixed complex in an UltrAuFoil R1.2/1.3 grid. (A) *Histogram of the micrograph resolution.* ***(B)*** *Representative micrograph of the dataset.* ***(C)*** *CTF*

of the selected micrograph. ***(D)*** *Averages from 2D classification from automatically picked particles.* ***(E)*** *A gallery of 3D volumes obtained without an initial model. Particle distribution is indicated below the 3D models. For size comparison, the negative stain volume is shown in green. Scale bar in (E) represents 50 Å.*

Single particle analysis of the dataset performed with cryoSPARC showed 2D averages with strong signal and uniformly dark background after several rounds of classification **(Figure 27.D)**. Particles (20576) were 3D-classified with cryoSPARC considering Fourier components up to 12 Å. The classification yielded better-defined classes, some of them reminiscent of the 3D classes obtained in Dataset_1 **(Figure 25.E)**. A common feature shared by the models is the presence of two lobes of different size connected by a thinner density. However, the comparison with the negative staining model suggests that the reconstructed volumes might be incomplete complexes.

Despite having class averages with a strong signal, no details of defined structural features could be noticed, neither from the 2D classes nor the 3D volumes. Biological samples scatter electrons poorly, which results in low SNR images. Consequently, thousands of particle images are compared and clustered in 2D classes. Here, particles are averaged to increase the SNR and, therefore, assess structural features and heterogeneity (either compositional or conformational) of the specimen. To increase the SNR in conventional transmission electron microscopy, the movies are acquired within a defocus range that enhances the contrast at the expense of losing high-resolution information.

Phase plate devices introduce a phase shift between scattered and unscattered electron waves that translate in amplitude variations in the image collected by the detectors. There is a stable version of the phase plate, based on the generation of a Volta potential in an amorphous carbon film at the diffraction plane, known as Volta Phase Plate (Danev & Baumeister, 2016; Danev et al., 2014). The VPP enables the imaging of the sample near to focus, avoiding the attenuation of high-resolution frequencies while increasing the contrast.

We reasoned that the lack of high-resolution features might be due to a loss of high-resolution information because of the underfocus. To test this hypothesis, images of the crosslinked complex-ADP in UltrAuFoil R1.2/1.3 were collected in a 300 kV Titan Krios equipped with VPP and an energy filter at the Diamond Light Source. In addition, the enhanced contrast provided by the VPP could help to visualize regions of the complex that are missing in the non-VPP cryoEM 3D reconstruction.

Images showed an enhanced contrast compared to the absence of VPP **(Figure 27.B vs Figure 28.B)**. SPA yielded 2D classes with more structural details than non-VPP data **(Figure 28.D)**. We classified the particles (29090) using cryoSPARC to generate several volumes, using only the information up to 12 Å resolution in the experimental images to generate the maps. The reconstructed volumes **(Figure 28.E)** showed two well-differentiated lobes of approximately the same size, a difference respect to the Dataset_2 **(Figure 27.E)**, possibly due to the contribution of the VPP. Moreover, the volumes showed differences in the relative orientation of the two lobes, which indicates the presence of several conformations and therefore points to the flexibility of the sample **(Figure 28.E)**.

Despite having more density than classes from Dataset_2 **(Figure 27.E)**, when compared with the 3D reconstruction of the HspB8:Bag3:Hsp70 complex obtained using negative staining, the 3D classes from Dataset_3 were clearly smaller and therefore could not contain all the components of the complex.

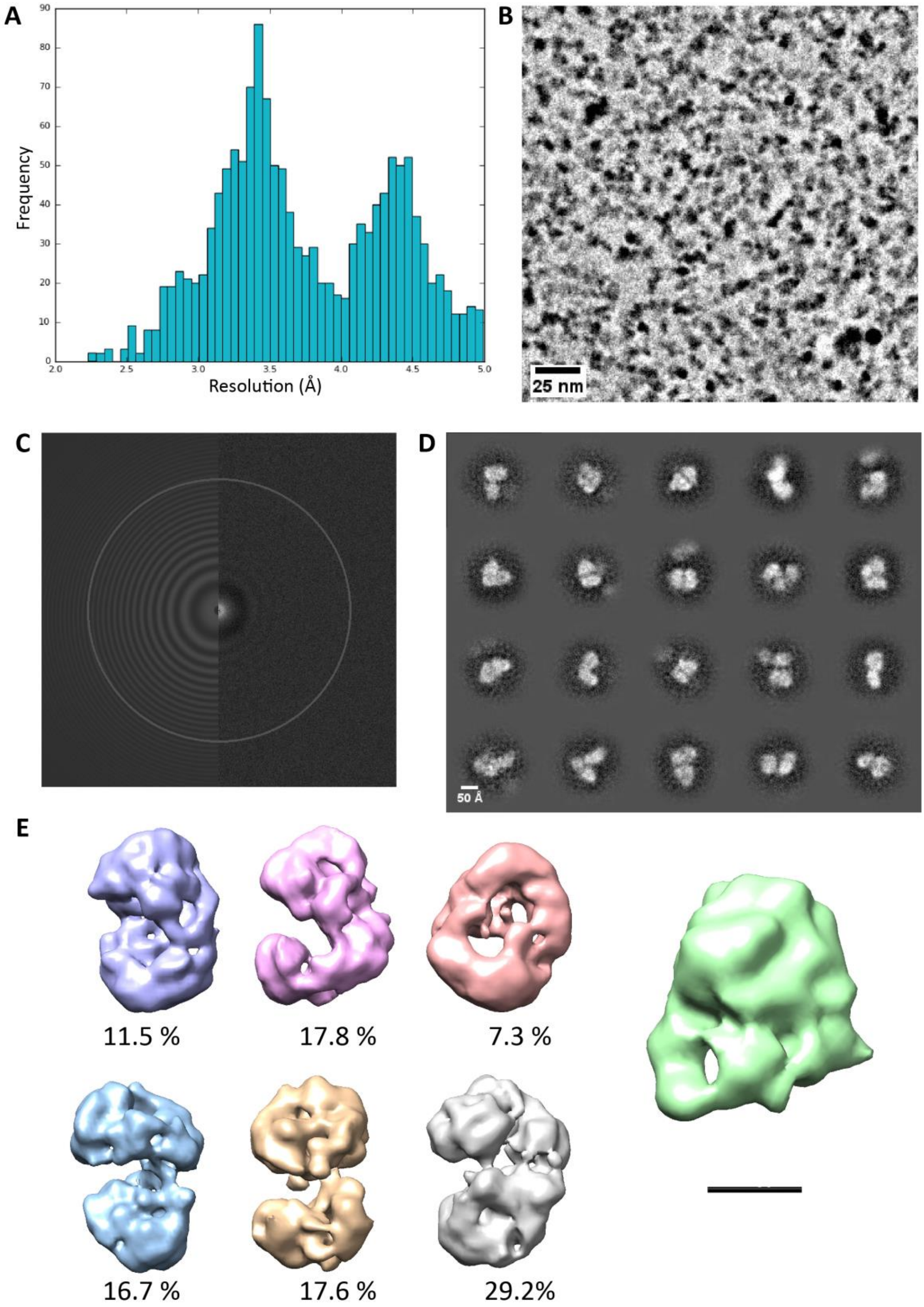

Figure 28. Single particle analysis of the fixed complex in an UltrAuFoil R1.2/1.3 grid with a 300 kV microscope equipped with VPP. (A) *Histogram of the micrograph resolution.* ***(B)*** *Representative image of the dataset.* ***(C)*** *CTF of the selected micrograph.* ***(D)*** *Averages from 2D classification from automatically picked particles.* ***(E)*** *A gallery of 3D volumes obtained without*

an initial model. Particle distribution is indicated below the 3D models. For size comparison, the negative stain volume is shown in green. Scale bar in (E) represents 50 Å.

At this point, the volumes obtained by cryoEM were not large enough to contain the atomic models of all the complex components. We selected Dataset_3 to dock the atomic models, since it was collected in a 300 kV microscope equipped with VPP, and the reconstructed 3D classes showed more mass than in other datasets.

The majority of the 3D classes from Dataset_3 displayed two connections between the two main densities **(Figure 29.A)**. We carried out the docking of the atomic structures in the most populated 3D class, which is shown in **Figure 29.B**. Being the mass of the reconstructed volumes much smaller than that obtained for the HspB8:Bag3:Hsp70 ternary complex reconstructed by negative stain, we reasoned that these particles had to be assigned to either Hsp70:Bag3 or Bag3:HspB8 complexes **(Figure 14 and Figure 17)**. The former is more compatible since the Hsp70 possesses two well-structured subdomains and consequently, they could be docked easily in the 3D map.

In the model, the atomic model of the Hsp70$_{NBD}$:BAG domain and the atomic structure of Hsp70$_{SBD}$ were conspicuous enough to be docked in the upper and lower masses, respectively. There was not enough mass left to dock neither any of the HspB8 molecules nor the remaining disordered parts of Bag3.

Based on this docking, the connection marked with a red arrow in **Figure 29.B** could correspond to the linker between Hsp70$_{SBD}$ and Hsp70$_{NBD}$. We propose that the second connection shown in **Figure 29.B** (marked with an asterisk) could correspond to an extra interaction between Bag3 and Hsp70, in this case with the Hsp70$_{SBD}$, that has been shown to be important for client release (Rauch et al., 2016b). The position of these two connections varies between the models shown in **Figure 29.A**, which could be explained by the flexibility of the Hsp70 linker and Bag3, and strengthens the dynamic nature of the interaction. Apart from this second connection, the other main difference between the two models is the relative orientation of Hsp70$_{SBD}$ and Hsp70$_{NBD}$.

Therefore, UltrAuFoil grids improved the stability of the complex during the ice layer formation as shown by the absence of aggregation. Images acquired with a Titan Krios, combined with VPP produced better 2D averages, reflecting the higher quality of the data. However, the reconstructed volumes did not contain enough density to allocate all the complex components. CryoET revealed that, despite the aggregation problem being solved, the particles still tended to arrange in a single stratum on one side of the ice layer **(Figure 30)**. We attribute that the interaction with the AWI could explain, at least partially, the current impossibility to obtain a 3D map at a higher resolution.

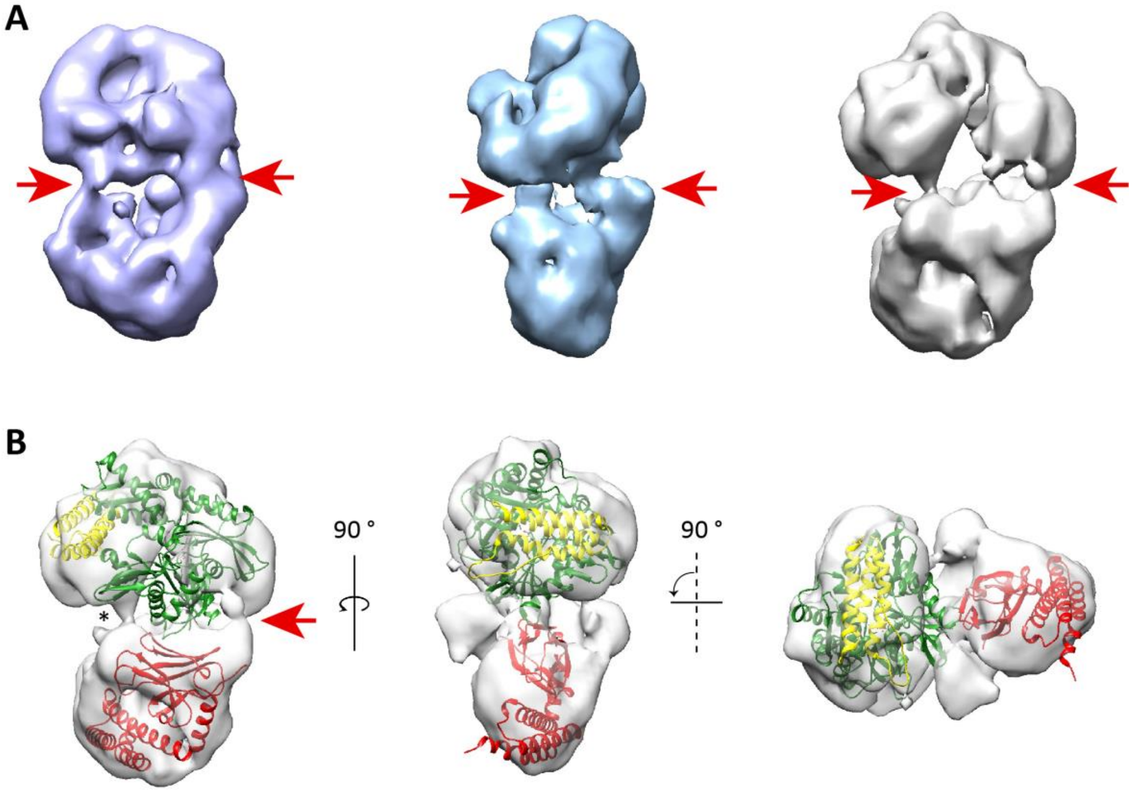

Figure 29. Docking of the Bag3:Hsp70 complex in the cryoelectron microscopy model. (A) *Three 3D classes from Figure 28.E rotated to display the connections between the two main lobes (red arrows). Volumes follow the same color code as in Figure 28.E.* ***(B)*** *Docking of the BAG domain, Hsp70*$_{NBD}$ *and Hsp70*$_{SBD}$ *in the reconstructed volume (the right one in (A)), showing two connections between the two main lobes.*

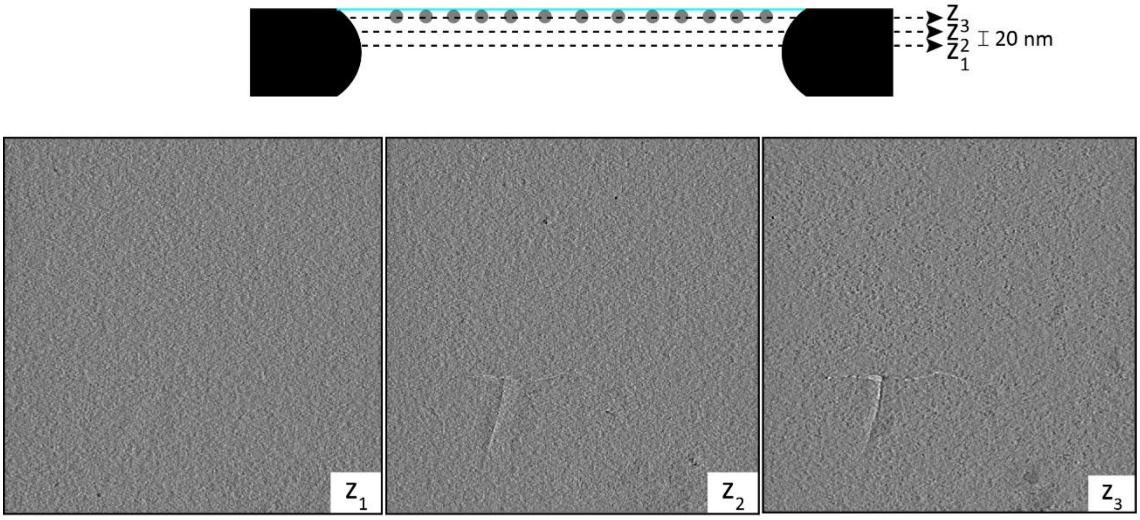

Figure 30. CryoET of the crosslinked complex in a glow-discharged UltrAuFoil R1.2/1.3 grid. *Diagram of the flattened tomogram and three planes at different points of the z-axis. Individual particles can be distinguished as darker dots in Z_3. A rip in the ice layer in the lower left quadrant of the planes was captured at different heights.*

Cryoelectron microscopy of the fixed HspB8:Bag3:Hsp70 complex in graphene oxide-coated Cu/Rh grids.

CryoET revealed a common feature during grid preparation, which was the tendency of the particles to distribute unevenly in ice, quite probably adsorbing to the AWI. The detergents employed with the fixed complex enhanced the aggregation, so an alternative method to protect the sample from the AWI was tested, which consisted in providing a substrate for the particles that maintain them far from the AWI (Pantelic et al., 2010). Common substrates include amorphous carbon or graphene oxide (GO), which can be functionalized to improve particle distribution and image quality (Naydenova et al., 2019).

We prepared custom-made GO-coated Cu/Rh grids with the crosslinked complex and analyzed them by cryoET to study their particle distribution **(Figure 31)**. The stripes in the plane Z_3 correspond to wrinkles of the GO layers, and shows that the grid hole was covered by several layers of GO. The Z_2 plane, spaced 10 nm from Z_3, shows the particles colocalizing with GO wrinkles. Therefore, cryoET demonstrates that the particles adsorb to the GO interface rather than the AWI.

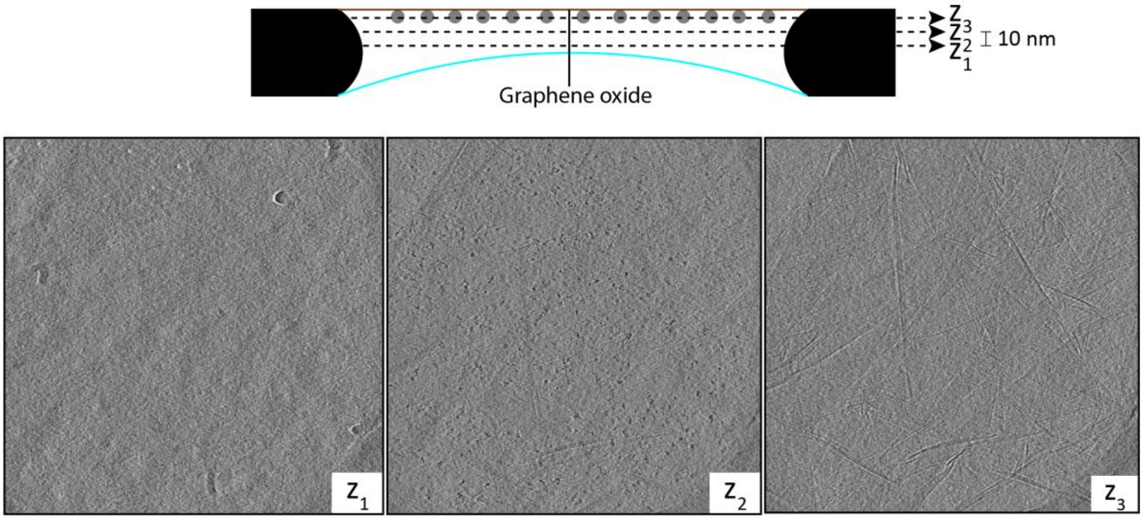

Figure 31. CryoET of the crosslinked complex in GO-coated Cu/Rh R0.6/1 grid. *Diagram of the flattened tomogram and three planes at different points of the z-axis.*

A dataset of the crosslinked complex in GO-grids was collected with a 200 kV Talos Arctica microscope and subjected to SPA **(Figure 32)**. The Thon rings in the CTF had a strong signal, a typical feature of carbon/GO-coated grids, and it allows the determination of the highest image resolution value. The 2D averages showed blurred regions, with less structural details than previous datasets. At this point, 45645 particles were 3D-classified limiting the resolution to consider up to 12 Å. The resulting 3D volumes were flatter than the ones obtained so far and again smaller in size compared with the negative stain model.

In summary, on the one hand, the use of GO-grids overcame the problem of particle attraction to the AWI, but its adsorption to the graphene-water interface caused particles to adopt preferential orientations. Consequently, the lack of angular projections covering all the directions yielded deformed 3D classes.

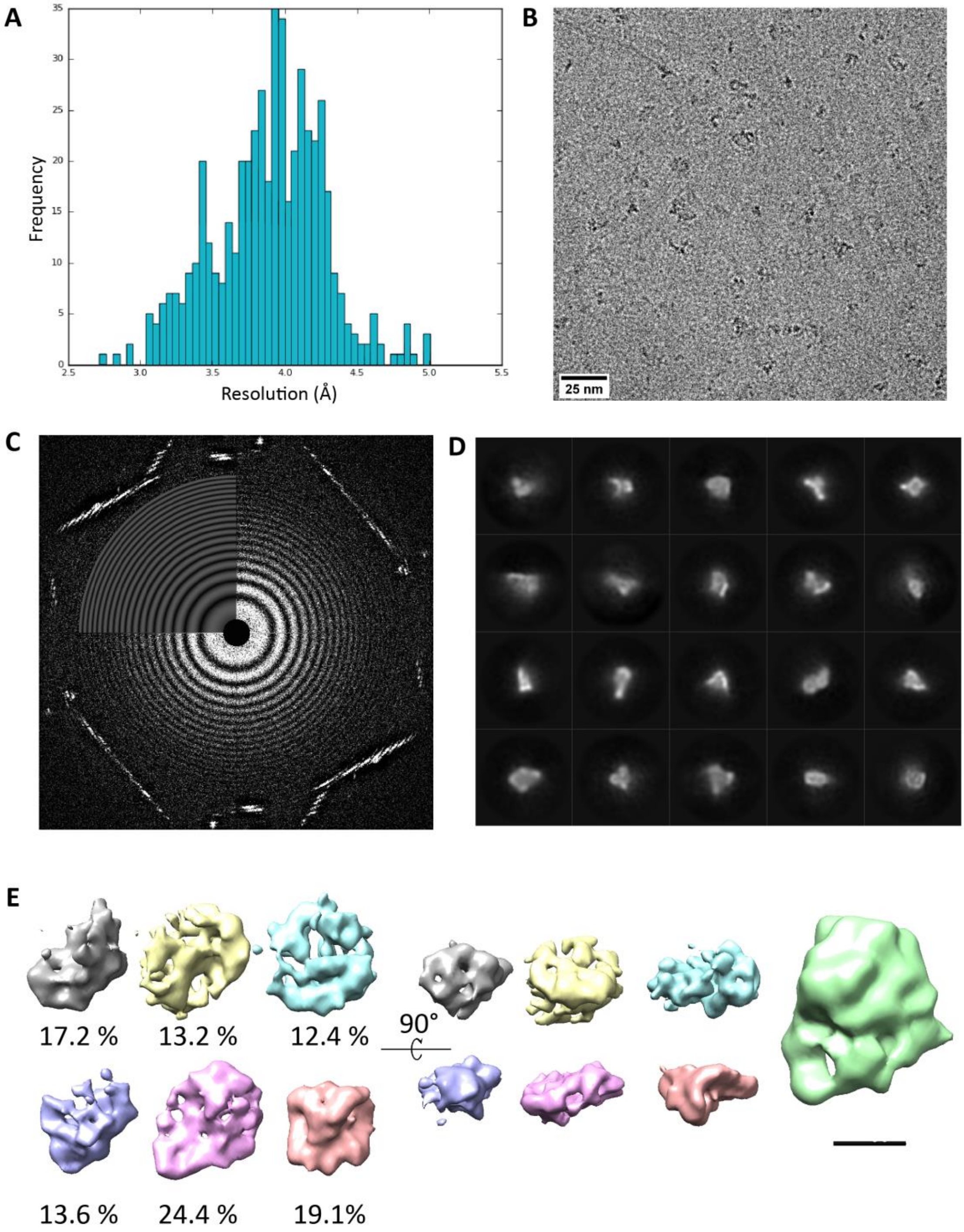

Figure 32. Single particle analysis of the fixed complex in graphene oxide grids. (A) *Histogram of the image resolution.* ***(B)*** *Representative image of the dataset.* ***(C)*** *CTF of the selected image.* ***(D)*** *Averages from 2D classification from automatically picked particles.* ***(E)*** *A gallery of 3D volumes obtained without an initial model. The same models were tilted 90° to show their flattened features. Particle distribution is indicated below the 3D models. For size comparison, the negative stain volume is shown in green. Scale bar in (E) represents 50 Å.*

DISCUSSION

DISCUSSION

Compositional homogeneity of the HspB8:Bag3:Hsp70 complex for cryoEM applications

Structure determination by cryoEM includes a series of critical steps, each of which should be optimized before moving downstream in the workflow (Passmore & Russo, 2016). The first critical step in the whole workflow is the purity of the sample. Compositional homogeneity is essential for single particle analysis. The presence of contaminants and degradation products may interfere in the complex formation and introduces a variability that complicates further image processing. Also, complementary biophysical characterization techniques result in easier data interpretation when performed with purified proteins. For this reason, we dedicated a considerable effort to optimize the purification protocols to obtain high purity proteins.

Hsp70 has two well-structured domains ($Hsp70_{NBD}$ and $Hsp70_{SBD}$), but the presence of a flexible linker connecting them makes Hsp70 prone to degradation by proteases. Indeed, a classical protocol for purifying either $Hsp70_{SBD}$ or $Hsp70_{NBD}$ included a digestion of this linker with papain (Cuéllar et al., 2008). Mass spectrometry analysis of the main bands observed by SDS-PAGE confirmed that the contaminants were degradation products, namely coming from $Hsp70_{NBD}$. This domain is able to interact with the BAG domain of Bag3 by itself, as shown in the crystal structure of $Hsc70_{NBD}$ with the BAG domain of the homologous Bag1 (Sondermann et al., 2001). Therefore, the presence of a mixture of Hsp70 and $Hsp70_{NBD}$ would be a source of heterogeneity, and its avoidance is recommended. Hsp70 is able to oligomerize depending on the nucleotide state (Aprile et al., 2013; Thompson et al., 2012). The biological relevance of the oligomers is still unclear. We have observed a certain degree of irreversible oligomerization during the purification procedure.

These problems led us to put an extra effort in improving the purification protocol for Hsp70. The previous protocol (Quintana-Gallardo et al., 2019) comprised an IMAC followed by a preparative SEC. The outcome was a preparation enriched in full-length Hsp70, but with a considerable amount of degradation and coexistence of monomeric and oligomeric forms in approximately similar extents.

The introduction of an IEX step with a heparin column greatly overcomes the two issues outlined above. The application of an extended salt gradient separated two populations of full-length Hsp70, while a considerable amount of degraded forms were also separated **(Figure 11)**. The two peaks were analyzed independently by SEC and Native-PAGE, showing that the IEX was critical for improving sample homogeneity. It is interesting to highlight that binding of Hsp70 to the heparin resin could have either an electrostatic or an affinity nature. Hsp70 contains the sequence LIGRK, which shares homology with a heparin-binding sequence present in fibronectin (Hansen et al., 1995).

Degradation was also the major challenge during Bag3 purification, despite the fact that it was conducted at 4°C in the presence of protease inhibitors. Degradation was initially attributed to an aggressive lysis method, however, WB analysis of aliquots taken directly from the cultured and lysed with SDS-PAGE Loading buffer **(Figure 12.A)** led us to conclude that Bag3 degradation existed before sonication, probably because of bacterial proteases. Moreover, the disordered nature of Bag3 structure could contribute to the degradation by proteases.

The degradation issue was overcome by screening expression conditions that minimized degradation while showing a reasonable overexpression level. This was attained in BL21 cells expressing in AIM at 30°C, where the proportion of full-length Bag3 to degraded species increased compared to IPTG-induced C41 cells. Bag3 degradation yielded an almost continuous smear of bands bearing the N-terminal His-tag, as can be seen by the fact that a shift in the migration distance of full-length Bag3 after TEV digestion also occurred for many of the lower molecular weight bands below **(Figure 10.B)**. Several IEX columns were tested at pH ranging from 6.0 to 8.5 and HiTrap Q column at pH 7.4 was found to retain mainly the full-length form **(Figure 12.B)**.

Even with pure proteins, it is difficult to have a perfectly homogenous sample of multiprotein complexes. Partially assembled complexes, conformational states, especially those complexes whose function relies on their flexibility, are potential sources of heterogeneity. Conformational heterogeneity has been a problem in the 3D reconstruction process, but recent advances in image processing allow discerning between discrete conformations co-existing in solution (Loveland et al., 2017; Nakane et al., 2018; Zhao et al., 2015). Even so, stabilizing the sample is sometimes necessary in order to attain higher resolution in the final reconstruction. Using crosslinkers, ligands or immunocomplexes that stabilize a certain conformation might result helpful in this regard (Masiulis et al., 2019; Wu et al., 2012).

The tendency of the HspB8:Bag3:Hsp70 complex to dissociate and aggregate during grid preparation **(Figure 19)** led us consider chemical crosslinking to covalently link subunits. Crosslinking can be made by direct addition of the crosslinker to a solution containing the sample. It is important to optimize both protein and crosslinker concentrations to reduce aggregates due to inter-complex crosslinks. Direct crosslinking combined with separation by SEC was also explored, but species were poorly separated (data not shown).

An alternative to this method is GraFix, which consists of centrifuging the sample in a combined density and crosslinker gradient (Kastner et al., 2007). The principle underlying this technique is that the complex fixation occurs gradually as it moves along the gradient. The main advantage of GraFix is a mild crosslinking that prevents fixation-associated artifacts, while removing aggregates. GraFix-treated structures have been successfully solved by cryoEM. For example, maps over 7 Å resolution of the spliceosome, a multisubunit complex, have been obtained, which has allowed to build pseudo-atomic models of the spliceosomal machinery (Agafonov et al., 2016; Bertram et al., 2017; Rauhut et al., 2016).

By adjusting the sucrose percentage of the gradient, we could successfully separate the majority of partially formed complexes and unbound components from the ternary complex. The presence of HspB8, Bag3 and Hsp70 in the isolated fractions was confirmed by MS analysis **(Figure 21)**. At a certain point, we decided to fix the complex in the presence of ADP, which introduced more heterogeneity in both the native and the crosslinked complex, reducing the fraction of complete complex in favor of incomplete complexes **(Figure 26.B)**. We assumed this increased variability in order to work closer to physiological conditions and to test whether ADP could stabilize certain conformations that could make processing more amenable.

The quaternary structure of HspB8

HspB8 was purified in the presence of elevated concentrations of reducing agents, following the protocol in (Kim et al., 2004) to prevent intermolecular crosslinking due to disulfide bonds. Other members of the sHsp family exist in high-order oligomers. Oligomerization is mediated by the conserved motif IXI/V in the sHsp CTD, which is absent in HspB8 CTD. Therefore, it is not expected to found HspB8 in high-oligomeric states. HspB8 can form heteroligomers *in vivo* (Arrigo & Gibert, 2013), but its homoligomerization state *in vitro* remains poorly studied.

SEC experiments showed that HspB8 eluted with an apparent molecular weight of 32-35 kDa, which slightly increased with concentration, similar to our observations (Kim et al., 2006) **(Figure 13.A)**. In the same study, bands compatible with dimers were detected upon incubation with crosslinker. Increasing protein concentration gradually reduced the quantity of monomers and increased the amount of dimers and high molecular species observed in SDS-PAGE.

We provide additional evidence to support a concentration-dependent oligomerization of HspB8. At 9 µM, the MW_W was similar to that calculated from the primary structure **(Figure 13.C)**. At 18 µM, the MW_W rose to 24.1 - 24.3 kDa, compatible with approximately a 15% of dimer. In SE-AUC, buoyant forces equilibrate with centrifugal forces, so protein distribution along the cell and subsequent MW calculation depend only on the molecular weight of the components. Therefore, SE-AUC provides molecular weight values that are not inferred from the hydrodynamic behavior of the species in solution, as can be the case for SEC or SV-AUC. This property allows not only an accurate estimation of the molecular weight but also the proportion of oligomeric forms present in solution.

HspB8 is sensitive to the oxidative state, so both SV- and SE-AUC experiments on HspB8 quaternary structure were performed in the presence and absence of reducing agent (Kim et al., 2004) **(Figure 13.B-C)**. According to our results, no differences in quaternary structure behavior were detected under oxidative and reducing conditions.

Biophysical properties of the HspB8:Bag3:Hsp70 complex

The chaperone network comprises several families of chaperones and co-chaperones involved in proteostasis. Some of those families have specialized in specific tasks. CCT, a member of the Hsp60 family has specialized in folding, Hsp100 are disaggregases, Hsp40 recruits specific clients to Hsp70 and Hsp90, and sHsp act as holdases, preventing aggregation. Hsp70 are versatile chaperones present in all the aspects of proteostasis thanks to their ability to interact with other chaperones. These interactions might be either direct or facilitated by other co-chaperones like Hop or Bag3 (Fernández-Fernández & Valpuesta, 2018).

In this work, we explored the role of Bag3 as an adaptor protein that physically connects Hsp70 and HspB8 and forms a ternary complex (HspB8:Bag3:Hsp70) that contributes to maintain the cellular proteostasis by removing aggregated or unfolded proteins through macroautophagy. Some of the client proteins of the complex are associated to neurodegenerative disorders, like mutant huntingtin or SOD (Crippa et al., 2010a).

We addressed the characterization of the ternary complex using analytical SEC and SV-AUC, which analyze the interaction in solution without the need for immobilizing any of the components. Our experiments corroborated that HspB8, Bag3 and Hsp70 form a stable multichaperone complex *in vitro*, with Bag3 linking HspB8 and Hsp70 **(Figure 14 and Figure 17)**, as previously demonstrated by Gestwicki's laboratory (Rauch et al., 2016a).

The affinity of Bag3 and Hsp70$_{NBD}$ is dependent on the nucleotide state (Rauch & Gestwicki, 2014). A hierarchy of affinity values exists, with the K_d decreasing from 3.3 nM for the apo-state, 10 nM in the ATP-bound and 41 nM for the ADP-bound state. Consistent with these measurements, a single peak containing the three proteins eluted when the complex was incubated without nucleotide **(Figure 14)** or with ATP (Rauch et al., 2016a). Incubation with ADP reduced the efficiency in the formation of the ternary complex, and consequently, two well-differentiated peaks eluted compared with incubation without nucleotide **(Figure 26.A)**.

An effect of pH on the complex stability was observed. The ProteoPlex assay revealed a preference for acidic pH under certain buffer systems **(Figure 18)**. However, we could not take advantage of this finding for electron microscopy applications. On the one hand, the condition recommended by the ProteoPlex assay, i.e. MES buffer at pH 6, did not improve the stability of the complex tested by negative stain. On the other hand, the crosslinking with glutaraldehyde is inefficient at pH 6, so the GraFix method was finally run with HEPES pH 7.4, the same buffer system as for SEC and AUC experiments.

In addition to a physical link, Bag3 is also a functional link between HspB8 and Hsp70. Substoichiometric concentrations of Bag3 promote nucleotide turnover (because it overcomes the rate-limiting step in cycling) of Hsp70, whereas ATPase activity is inhibited by higher concentrations of Bag3 (Rauch & Gestwicki, 2014). A similar effect has been observed on the stimulation of folding activity of Hsp70. The presence of HspB8 adds an additional level of regulation, affecting the chaperone function of Hsp70 through Bag3. Low concentrations of HspB8 stimulate ATPase activity, but make Bag3 a more potent inhibitor at high concentrations. However, increasing concentrations of HspB8 promote luciferase refolding activity (Rauch et al., 2016a). HspB8 has no effect on ATPase activity in the absence of Bag3.

The mechanistic aspects of this process and how the three proteins interplay in physiological conditions are still not fully understood. Bag3 is the only stress-inducible member of the BAG family, so it has been proposed that Bag3 could recruit HspB8 and Hsp70 together under circumstances that promote protein unfolding and aggregation (Rauch et al., 2016a).

Based on our results, HspB8 and Hsp70 do not form a binary complex **(Figure 14.B)**. However, an interesting pattern occurred in both SEC and SV-AUC experiments. In controls, Hsp70 eluted at 14.19 ml and HspB8 eluted at 16.46. When a mixture of both proteins was loaded, two peaks corresponding to Hsp70 and HspB8 eluted independently **(Figure 14.B)**. The peak corresponding to HspB8 underwent a slight shift to higher MW (16.22 ml). In SV-AUC, loading HspB8 and Hsp70 together was accompanied by an increase of the dimer peak of HspB8 in the presence of Hsp70 with respect to the control, despite the fact that similar concentrations of HspB8 were loaded (14 µM). This observation suggests an influence of Hsp70 on the oligomeric state of HspB8. However, the relevance of this observation and its possible influence in the final stoichiometry of the complex remain to be explored.

Characterization of vitrification-derived problems: particle distribution and the air-water interface

After sample purity and stability, the next bottleneck is the sample preparation in cryoEM grids. The aim is to obtain grids with a thin layer of amorphous ice with well-distributed particles that preserves high-resolution information.

Several parameters were adjusted to obtain high-quality preparations for dataset acquisition that include the type of grid support (Cu/Rh and UltrAuFoil grids), grid hole diameter (R0.6/1 and R1.2/1.3), glow discharge, protein concentration and protein stability.

Glow discharge had clear effects on ice distribution. Increasing discharge time resulted in increased ice coverage, with little or no grid squares without ice. The absence of treatment resulted in empty holes or clusters of thick ice in the center of the grid square, which limited the grid areas susceptible to be imaged. Shorter discharge times diminished the particle aggregation in Cu/Rh grids.

The material of the grid support also had an influence on particle distribution. Whereas the crosslinked complex aggregated in glow-discharged Cu/Rh grids, the aggregation was completely avoided in UltrAuFoil grids.

The hole size is also a parameter to take into account, since a thin film of vitreous ice is easier to obtain in small diameter holes (Drulyte et al., 2018). However, more images per hole can be collected in larger holes, so the speed of data collection increases. In our experience, we did not observe differences in terms of ice coverage when both sizes where compared.

HspB8:Bag3:Hsp70 formed a stable ternary complex under native conditions. It was subjected to cryoEM in four nucleotide states: apo(no nucleotide)-, ADP-, ATP-state and with the non-hydrolyzable ATP analogue AMP-PNP **(Figure 19)**. Proteins were mixed for a final complex concentration of 7 µM (1.23 mg/ml). The selected concentration was a compromise between an over-populated grid, but still above the K_d to prevent complex disassembly (K_d HspB8:Bag3= 0.3-1.2 µM; K_d Bag3:Hsp70= 2-3 nM) (Rauch & Gestwicki, 2014; Rauch et al., 2016a). For cryoEM applications, the ternary complex was generated with SEC in a column that minimized sample dilution. SEC performed immediately before sample vitrification showed a defined peak for the ternary complex, with no indications of aggregated material. However, after vitrification particles of variable sizes were visible in cryoEM regardless of the nucleotide state (ranging from aggregates to small particles). A similar behavior was observed in the crosslinked complex, where no aggregation was detected in the isolated complex **(Figure 23)**. Therefore, the deleterious effect on sample stability can be attributed to the vitrification procedure.

During sample manipulation, proteins are exposed to hostile interfaces that are harmful for many of them. In the vitrification procedure, the excess of sample is blotted with filter paper and a thin film of water (10-90 nm) is formed before the grid is plunged into the cryogen. In this time window (0.5-1 seconds), molecules collide thousands of times with the air-water interface due to Brownian motion (Trurnit, 1960). The contact with interfaces can result in complex dissociation and protein denaturation and consequently high-resolution structure determination might be compromised. Indeed, approximately 90% of the particles adsorbed to the AWI are partly denatured, with the unfolded region facing the interfaces (Noble et al., 2018a).

We performed cryoET to explore particle distribution in the different conditions of grid preparation explored in this work. CryoET allows the 3D reconstruction of a complete grid hole, thus providing diagnostic information on the particle distribution through the ice layer that is missing in 2D images.

The boundaries of the ice layer, and consequently the exact position of the AWI, were difficult to identify in tomograms. However, computationally flattening of tomograms showed the protein complex displaying a tendency to arrange in a single layer, either as aggregates or in a soluble state **(Figure 20, Figure 24 and Figure 30)**. Therefore, it strongly suggests that the sample was adsorbed to one of the interfaces of the ice layer. Negative stain and cryoEM maps are within 10-14 nm in their longer dimensions. The planes shown in the tomograms were spaced 20 nm each other, so the fact that little or no particles were detected in more than a plane strongly supports the idea that the complex adsorbed to one of the interfaces. The potential adsorption to the AWI occurred both in Cu/Rh and UltrAuFoil grids, with almost all the particles lying in a single stratum. Given the impact of the AWI on protein tertiary/quaternary structure, we explored different possibilities to minimize this problem.

Several methods have been developed to tackle the AWI problem. For example, reducing the interval between sample application and plunge freezing to 100 ms results in particles adopting more orientations than in the typical interval of 0.5-1 s. The adoption of preferential orientations is one of the effects caused by the AWI, so the authors used this criterion as an indirect indication of adsorption to the AWI (Noble et al., 2018b).

Another approach to solve the AWI problem consists of using surfactants such as detergents (Glaeser, 2018). The use of detergents has proven to be helpful for samples showing preferential orientations induced by interaction with the AWI. For example, the addition of CHAPSO (zwitterionic) at the CMC to a bacterial polymerase resulted in an evenly spread sample throughout the ice layer, as revealed by cryoET (Chen et al., 2019). The sample had shown a strong tendency to interact with the AWI through few defined orientations. We tested the detergents DDM, LMNG, OG (non-ionic) and CHAPS (zwitterionic) at concentrations below the CMC to improve particle distribution of the crosslinked complex, however the aggregation was unexpectedly enhanced **(Figure 23.B-E)**.

Adsorption to the AWI can be completely avoided when the sample is vitrified in grids with hydrophilized substrate, like carbon or graphene oxide (GO) (D'Imprima et al., 2019). The use of GO monolayers deposited over grids has been shown to prevent particles for arranging in the AWI and structure reconstructions to atomic resolution have been obtained. Therefore, the graphene signal does not interfere with the posterior single particle analysis (Fan et al., 2019).

Custom-made GO-coated Cu/Rh grids dramatically reduced the adsorption to the AWI. Cross-sections of the tomogram along the z-axis spaced 10 nm demonstrated a preference for the graphene-water interface (GWI) **(Figure 31)**. These observations confirm GO as a suitable approach to prevent particles to adsorb to the AWI.

The most popular method for vitrification is based on applying 3-4 µl of sample to the grid, blotting the excess with filter paper to generate a thin layer of water and freezing the grid in cooled ethane. The process is accomplished in a semi-automated vitirification station, where environmental variables like temperature or humidity can be controlled. This fact allows a higher reproducibility compared to previous manual plunge freezers by automatically blotting with prefixed forces and time. Even so, the reproducibility of grid preparation is still limited with this method and there is little control over the ice thickness. Additionally, the interval between sample application and freezing varies from 0.5 to few seconds, enough for the particles to adsorb to the AWI almost completely (Noble et al., 2018b).

New vitrification methods, still under development, aim to minimize the sample application-freezing interval to several hundreds of milliseconds or less, thus, reducing contacts with AWI and induction of preferred orientations. Among them, Spotiton is a device that employs a piezo-electric inkjet dispensing system to apply 20-50 nl of sample to self-blotting grids (Razinkov et al., 2016). The CryoWriter system uses microcapillary to apply 2-20 nl of sample, with the advantage that the ice thickness can be controlled (Arnold et al., 2017). The laboratory of Joachim Frank (Columbia University) has developed a microfluidics-based device to spray a tiny volume of sample on the grid, with controllable thickness, and fast enough for time-resolved electron microscopy (Feng et al., 2017). Finally, other technology employs acoustic waves to dispense few femtoliters of sample, and capable of vitrifying within 50 ms from sample application (Ashtiani et al., 2018). Altogether, new vitrification methods aim to reduce the sample amount, increase grid reproducibility and fasten the process to overcome current issues in one of the main bottlenecks of the cryoEM workflow.

Data processing and intrinsic flexibility of the complex components

Volta Phase Plate (VPP) enhances particle contrast at near-focus, so high-resolution information is preserved. Acquisition of datasets with VPP has been proven useful to increase the resolution to visualize side chains of the adenosine A_{2A} receptor coupled to a heterotrimeric G protein (García-Nafría et al., 2018). A dataset from a preparation of the *Clostridium perfringens* enterotoxin acquired with VPP produced a map with higher resolution than a non-VPP dataset from the same grid (Savva et al., 2019). It is expected that VPP-induced contrast enhancement aids particle picking and particle alignment, and less particles are required to achieve the same resolution than in underfocus-based conventional microscopy. The effects of VPP on the contrast in Dataset_3 were evident compared to non-VPP datasets **(Figure 27.B vs Figure 28.B)**. Indeed, individual particles could be clearly distinguishable in populated grids when VPP was enabled. In relation to the increased signal, the 3D volumes from Dataset_3 displayed two lobes of similar size compared to the uneven lobes in models obtained from Dataset_1 and Dataset_2. The level of details in the 2D averages of the VPP dataset slightly improved compared to the 2D averages of non-VPP datasets. Despite the positive contribution of the VPP, both the 2D averages and 3D classes lacked secondary structure details.

There are a variety of single particle reconstruction software available. They all have been able to successfully solve macromolecular structures at high-resolution. One of the most popular software for single particle reconstruction is Relion (Scheres, 2012). We found that using Relion for 2D classifications yielded averages with overfitting, visible as streaks emerging from the center of the 2D average. In Relion, experimental images are masked with a soft circular mask of a diameter specified by the user, so only the information inside the mask will be used for classification. The overfitting was observed when the particles were masked with zeros, i.e., pixel values covered by this mask were substituted by zeros. Masking with random noise instead of zeros avoided overfitting, but the resulting classes lacked any detail even in those classifications where the resolution was not restricted. In both cases, the discrimination of structural features and the assessment of the classification effectiveness were hindered. As an alternative, we used cryoSPARC (Punjani et al., 2017) for the 2D classifications, which was capable of producing better 2D classes without overfitting.

These observations suggest that, although the efficacy of the different software packages available for single particle analysis has been clearly demonstrated, some of them might work better than others when processing certain datasets.

A 3D reconstruction was carried out using negatively stained, crosslinked particles of the HspB8:Bag3:Hsp70 complex **(Figure 22.A)**. The size of the reconstructed volume clearly pointed to the presence of all the components of the complex, which was confirmed by XL-MS. Data from XL-MS helped in the docking of all the parts of the three proteins whose structure is either known ($Hsp70_{NBD}$ and $Hsp70_{SBD}$) or can be modeled using the atomic structures of homologous domains (HspB8 and the WW and BAG domains of Bag3).

The docking places the two Hsp70 domains in an extended conformation, very similar to that determined for the ADP conformation of the prokaryote homologue DnaK (Bertelsen et al., 2009) (PDB 2KHO). The WW region of Bag3 showed six interaction points with Hsp70 and two with HspB8, which led us to place the WW region in an intermediate position between Hsp70 and HspB8 **(Figure 22.B-E)**.

The sizes of the volumes of the crosslinked HspB8:Bag3:Hsp70 complex obtained by cryoEM were not large enough to contain the atomic structures of the three components **(Figure 25.E, Figure 27.EFigure 28.E)**. We docked the atomic models of $Hsp70_{NBD}$, $Hsp70_{SBD}$ and the BAG domain, in a 3D volume from Dataset_3 **(Figure 29.B)**. ADP-induced sample heterogeneity was observed in both the native and the crosslinked complex **(Figure 26.D)**. Despite the heterogeneity, the band of the ternary complex was still predominant in SDS-PAGE after sample concentration (data not shown), and the presence of the three components in the band was confirmed by MS.

Therefore, we reasoned that the absence of part of the complex in the final reconstruction could be due to issues occurring downstream the grid preparation stage. The complex could be damaged during vitrification, with part of it undergoing degradation or denaturation induced by the AWI. In this scenario, HspB8 could be more susceptible to damage, which would explain its absence in the final reconstruction.

Another possibility, and not necessarily in conflict with the above, is that the flexible and/or unstructured nature of some regions of the complex make difficult their alignment, visualization and further 3D reconstruction. Such regions might include the missing parts of Bag3 and HspB8. In contrast, the structured parts of the complex, $Hsp70_{NBD}$, $Hsp70_{SBD}$ and BAG domain could be aligned and reconstructed. Indeed, the docking of the atomic model of the $Hsp70_{NBD}$:BAG domain and the atomic structure of $Hsp70_{SBD}$ in each of the two lobes of the most populated 3D class from Dataset_3 was straightforward **(Figure 29.B)**.

The two lobes are connected in all the classes by a connection that can be attributed to the $Hsp70_{NBD}$-$Hsp70_{SBD}$ linker. Moreover, some classes show a second connection between the two masses at variables positions of the $Hsp70_{SBD}$. It has already been reported that Hsp70 is linked with Bag3 not only through the “canonical” interaction between $Hsp70_{NBD}$ and the Bag3 BAG domain, but also between $Hsp70_{SBD}$ and a yet an unknown region of Bag3 (Rauch et al., 2016b). According to the authors, whereas the former interaction would control the nucleotide exchange of Hsp70, the latter would be involved in regulating the substrate release **(Figure 33.A)**. A similar bimodal interaction has been observed for the prokaryotic Hsp70, DnaK, and its NEF GrpE between (Melero et al., 2015), which involves the $DnaK_{SBD}$ and the disordered N-terminal domain of the cochaperone **(Figure 33.B)**. In the two cases, the second interaction introduces an additional level of regulation of the stability of the Hsp70:client protein complex that would confer a greater control over the affinity and timing of client release in response to specific conditions in the cell.

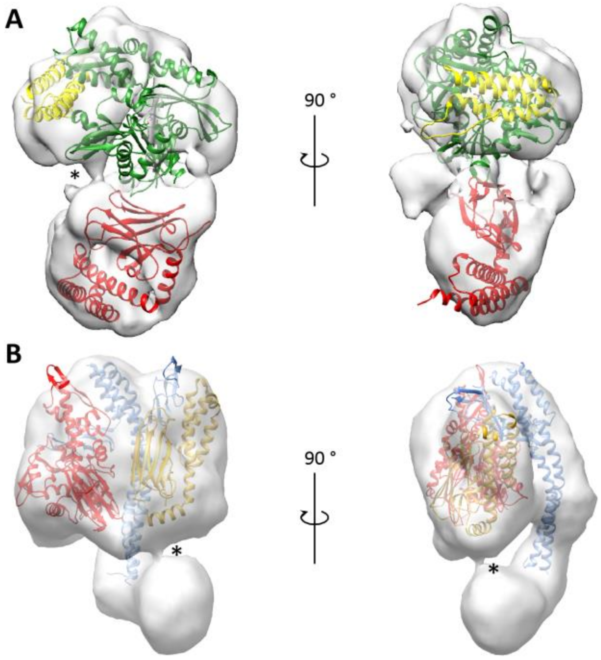

Figure 33. Comparison of two Hsp70:NEF systems. (A) *CryoEM 3D reconstruction with the atomic structures of Hsp70$_{NDB}$ (red), Hsp70$_{SBD}$ (yellow) and BAG domain (blue).* ***(B)*** *3D reconstruction of the DnaK:GrpE complex by negative stain with the DnaK$_{NBD}$ (red), DnaK$_{SBD}$ (yellow) and GrpE (blue) atomic structures docked inside. Extracted from (Melero et al., 2015). Asterisks indicate the second interaction site between Hsp70 and its corresponding NEF.*

We propose the flexibility of the components as one of the factors that contribute to the low resolution of the models. Biophysical analyses by SEC, AUC and CD demonstrate that HspB8 and Bag3 possess unstructured regions. In SEC, Bag3 eluted with an apparent molecular weight considerably higher than that calculated from its sequence (61.6 kDa). For comparison, His-Hsp70 used in the same analytical SEC experiments had a MW= 72.1 kDa and eluted at 14.19 ml. According to Shemetov & Gusev, 2011, the estimated Stokes radius for a globular protein of a MW similar to Bag3 is 32.6 Å, whereas the Stokes radius for the same unfolded protein would be 71-73 Å. The same authors calculated an apparent molecular weight of 390 kDa and Stokes radius of 73.6 Å. This behavior could be explained by either oligomerization or hydrodynamic properties.

So far, there are no reports describing oligomerization of wild type Bag3. Self-association has only been described in Bag3 P209L and P470S mutants (Meister-Broekema et al., 2018). However, more evidences point at a disordered nature of Bag3 structure. CD measurements indicated a strong presence of random coil, with a proportion of α-helices, accounted at least by the BAG domain **(Figure 16.A)**. In SV-AUC, the experimental normalized sedimentation coefficient, $S_{20,w}$ was 2.6. The theoretical coefficient calculated if the protein were a smooth sphere of 61.6 kDa is 5.3 S (S_{max}). The S_{max}/S_{exp} ratio, also known as frictional ratio, provides a low-resolution estimation of the global shape of a protein. For Bag3, S_{max}/S_{exp}= 5.3/2.6= 2.0, which corresponds to a moderately to highly elongated protein (Erickson, 2009). Our data, in agreement with similar experimental data and calculations with protein disorder predictions programs (Shemetov & Gusev, 2011) strongly support that Bag3 is an intrinsically disordered protein.

HspB8 also presents characteristics of a disordered protein. As a member of the sHsp, HspB8 bears an ACD consisting of a β-sandwich, flanked by disordered NTD and CTD. The frictional ratio calculated from S_{max}/S_{exp}= 2.82/2.01= 1.4 for the monomeric HspB8, which shares intermediate properties of globular and moderately elongated proteins. The proportion of secondary elements estimated from its CD spectrum is consistent with the features of the family members: 36.5% β-strand, 37.4% random coil and barely 5% α-helix (Kim et al., 2006). Our analysis of HspB8 secondary structure by CD shows similar properties. In addition, differential CD spectrum reveals an acquisition of secondary structure in the HspB8:Bag3 interaction **(Figure 16.C)**. This gain of secondary structure supports the idea that HspB8:Bag3 interaction entails a decrease in the elongated shape of the binary complex. It would explain the fact that HspB8:Bag3 complex elutes at the same volume as Bag3 alone.

The frictional ratio calculated for His-Hsp70 was 6.27/4.2= 1.5, characteristic of elongated proteins. SV-AUC experiments were performed in the absence of nucleotide. This is consistent with the expected conformation of Hsp70 in the apo-state, similar to the extended conformation of the ADP-bound state **(Figure 2.B)**. Hsp70 bears a flexible interdomain linker that adopts many conformations (English et al., 2017). This is also the case of the most C-terminal part of Hsp70, which is necessary for the interaction with CHIP, and whose flexibility is essential for substrate ubiquitination by this cochaperone (Quintana-Gallardo et al., 2019).

Future structural studies of flexible complexes might benefit from alternative approaches that increase protein stability. Nanobodies and Fabs constitute an interesting example. Nanobodies are derivatives of heavy chain-only antibodies produced by camelids (Pardon et al., 2014). Fabs, which stand for antigen-binding fragment, are generated by digestion of entire antibodies and contain only the antigen-binding site of the light and heavy chains. Both Fabs and nanobodies have been proven helpful in X-ray or NMR structural studies and have been also used to solve challenging structures by cryoEM (Butterwick et al., 2018; García-Nafría et al., 2018).

CONCLUSIONS/CONCLUSIONES

CONCLUSIONS

1. We have generated a ternary complex formed by the chaperones Hsp70 and HspB8 and the co-chaperone Bag3, which acts as a linker between the two chaperones. The complex has been characterized using different biophysical techniques.
2. The complex does not evenly distribute in the ice layer during vitrification but has a tendency to adsorb to a single stratum, quite likely the air-water interface. This uneven distribution is accompanied by the disassembly of the complex. Crosslinking prevents the disassembly of the complex, at least partially, but not the uneven distribution. Crosslinked complexes adsorb to graphene oxide-coated grids preventing them from arranging in the air-water interface, however protein complexes show preferential orientations that yielded deformed 3D classes.
3. The support material and surface ionization of the grids have a dramatic effect on complex solubility.
4. We have obtained a low-resolution 3D map of the HspB8:Bag3:Hsp70 complex by negative staining, and a pseudoatomic model of the ternary complex has been generated in combination with crosslinking-mass spectrometry data.
5. Despite the improvement in sample and grid preparation, we have only obtained by cryoEM a low-resolution 3D map where the atomic models of $Hsp70_{SBD}$ and $BAG:Hsp70_{NBD}$ could be accommodated. In this model, in addition to the “canonical” interaction between $Hsp70_{NBD}$ and the Bag3 BAG domain, we have also identified a second interaction between Bag3 and $Hsp70_{SBD}$ that has been previously proposed to control the release of Hsp70 client proteins.

CONCLUSIONES

1. Hemos generado un complejo ternario formado por las chaperonas Hsp70 y HspB8 y la co-chaperona Bag3, que ejerce como conexión entre las dos chaperonas, y hemos caracterizado el complejo a través de diferentes técnicas biofísicas.
2. El complejo no se distribuye de manera uniforme en la capa de hielo amorfo durante la vitrificación, sino que tiene una tendencia a ordenarse en un único estrato, probablemente en la interfaz líquido-aire. Esta distribución va acompañada del desensamblaje del complejo. La fijación del complejo previno el desensamblaje de sus componentes, al menos parcialmente, pero no la distribución no uniforme. Los complejos fijados se adsorbieron a rejillas cubiertas con óxido de grafeno, protegiéndolos de la interfaz líquido-aire. Sin embargo, el complejo adoptaba orientaciones preferenciales, lo que dio lugar a clases 3D deformadas.
3. El material de la rejilla y la ionización de su superficie tienen efectos notables en la solubilidad del complejo.
4. Hemos obtenido un modelo a baja resolución del complejo HspB8:Bag3:Hsp70 por tinción negativa, con el que elaboramos un modelo pseudoatómico en combinación con datos de espectrometría de masas.
5. A pesar de la mejora en la preparación de la muestra y de la rejilla, por criomicroscopía electrónica solo hemos obtenido un mapa tridimensional a baja resolución donde podemos colocar los modelos atómicos de $\text{Hsp70}_{\text{SBD}}$ y BAG:$\text{Hsp70}_{\text{NBD}}$. En este modelo, además de la interacción canónica entre $\text{Hsp70}_{\text{NBD}}$ y el dominio BAG de Bag3, hemos identificado una segunda interacción entre Bag3 y $\text{Hsp70}_{\text{SBD}}$ descrita previamente e implicada en el control de la liberación de proteínas cliente de Hsp70.

REFERENCES

REFERENCES

Abrishami, V., Zaldívar-Peraza, A., De La Rosa-Trevín, J. M., Vargas, J., Otón, J., Marabini, R., Shkolnisky, Y., Carazo, J. M., & Sorzano, C. O. S. (2013). A pattern matching approach to the automatic selection of particles from low-contrast electron micrographs. *Bioinformatics*, *29*(19), 2460–2468. https://doi.org/10.1093/bioinformatics/btt429

Agafonov, D. E., Kastner, B., Dybkov, O., Hofele, R. V., Liu, W. T., Urlaub, H., Lührmann, R., & Stark, H. (2016). Molecular architecture of the human U4/U6.U5 tri-snRNP. *Science*, *351*(6280). https://doi.org/10.1126/science.aad2085

Agarraberes, F. A., & Dice, J. F. (2001). A molecular chaperone complex at the lysosomal membrane is required for protein translocation. *Journal of Cell Science*, *114*(Pt 13), 2491–2499. Retrieved from http://www.ncbi.nlm.nih.gov/pubmed/11559757

Agarraberes, F. A., Terlecky, S. R., & Dice, J. F. (1997). An intralysosomal hsp70 is required for a selective pathway of lysosomal protein degradation. *Journal of Cell Biology*, *137*(4), 825–834. https://doi.org/10.1083/jcb.137.4.825

Alberti, S., Mateju, D., Mediani, L., & Carra, S. (2017). Granulostasis: Protein Quality Control of RNP Granules. *Frontiers in Molecular Neuroscience*, *10*(March), 84. https://doi.org/10.3389/fnmol.2017.00084

Alvira, S., Cuéllar, J., Röhl, A., Yamamoto, S., Itoh, H., Alfonso, C., Rivas, G., Buchner, J., & Valpuesta, J. M. (2014). Structural characterization of the substrate transfer mechanism in Hsp70/Hsp90 folding machinery mediated by Hop. *Nature Communications*, *5*, 5484. https://doi.org/10.1038/ncomms6484

Aprile, F. A., Dhulesia, A., Stengel, F., Roodveldt, C., Benesch, J. L. P., Tortora, P., Robinson, C. V., Salvatella, X., Dobson, C. M., & Cremades, N. (2013). Hsp70 Oligomerization Is Mediated by an Interaction between the Interdomain Linker and the Substrate-Binding Domain. *PLoS ONE*, *8*(6), 1–17. https://doi.org/10.1371/journal.pone.0067961

Arimura, T., Ishikawa, T., Nunoda, S., Kawai, S., & Kimura, A. (2011). Dilated cardiomyopathy-associated BAG3 mutations impair Z-disc assembly and enhance sensitivity to apoptosis in cardiomyocytes. *Human Mutation*, *32*(12), 1481–1491. https://doi.org/10.1002/humu.21603

Arndt, V., Dick, N., Tawo, R., Dreiseidler, M., Wenzel, D., Hesse, M., Fürst, D. O., Saftig, P., Saint, R., Fleischmann, B. K., Hoch, M., & Höhfeld, J. (2010). Chaperone-Assisted Selective Autophagy Is Essential for Muscle Maintenance. *Current Biology*, *20*(2), 143–148. https://doi.org/10.1016/j.cub.2009.11.022

Arndt, V., Rogon, C., & Höhfeld, J. (2007). To be, or not to be - Molecular chaperones in protein degradation. *Cellular and Molecular Life Sciences*, *64*(19–20), 2525–2541. https://doi.org/10.1007/s00018-007-7188-6

Arnold, S. A., Albiez, S., Bieri, A., Syntychaki, A., Adaixo, R., McLeod, R. A., Goldie, K. N., Stahlberg, H., & Braun, T. (2017). Blotting-free and lossless cryo-electron microscopy grid preparation from nanoliter-sized protein samples and single-cell extracts. *Journal of Structural Biology*, *197*(3), 220–226. https://doi.org/10.1016/j.jsb.2016.11.002

Arrigo, A.-P., & Gibert, B. (2013). Protein interactomes of three stress inducible small heat shock proteins: HspB1, HspB5 and HspB8. *International Journal of Hyperthermia*, *29*(5), 409–422. https://doi.org/10.3109/02656736.2013.792956

Ashford, T. P., & Porter, K. R. (1962). Cytoplasmic components in hepatic cell lysosomes. *The Journal of Cell Biology*, *12*(1), 198–202. https://doi.org/10.1083/jcb.12.1.198

Ashtiani, D., Venugopal, H., Belousoff, M., Spicer, B., Mak, J., Neild, A., & de Marco, A. (2018). Delivery of femtolitre droplets using surface acoustic wave based atomisation for cryo-EM grid preparation. *Journal of Structural Biology*, *203*(2), 94–101. https://doi.org/10.1016/j.jsb.2018.03.012

Bai, X. chen, McMullan, G., & Scheres, S. H. W. (2015). How cryo-EM is revolutionizing structural biology. *Trends in Biochemical Sciences*, *40*(1), 49–57. https://doi.org/10.1016/j.tibs.2014.10.005

Ballinger, C. A., Connell, P., Wu, Y., Hu, Z., Thompson, L. J., Yin, L.-Y., & Patterson, C. (1999). Identification of CHIP, a Novel Tetratricopeptide Repeat-Containing Protein That Interacts with Heat Shock Proteins and Negatively Regulates Chaperone Functions. *Molecular and Cellular Biology*, *19*(6), 4535–4545. https://doi.org/10.1128/mcb.19.6.4535

Bandyopadhyay, U., Kaushik, S., Varticovski, L., & Cuervo, A. M. (2008). The Chaperone-Mediated Autophagy Receptor Organizes in Dynamic Protein Complexes at the Lysosomal Membrane. *Molecular and Cellular Biology*, *28*(18), 5747–5763. https://doi.org/10.1128/mcb.02070-07

Behl, C. (2016). Breaking BAG: The Co-Chaperone BAG3 in Health and Disease. *Trends in Pharmacological Sciences*, *37*(8), 672–688. https://doi.org/10.1016/j.tips.2016.04.007

Bertani, G. (1951). Studies on lysogenesis. I. The mode of phage liberation by lysogenic Escherichia coli. *Journal of Bacteriology*, *62*(3), 293–300.

Bertelsen, E. B., Chang, L., Gestwicki, J. E., & Zuiderweg, E. R. P. (2009). Solution conformation of wild-type E. coli Hsp70 (DnaK) chaperone complexed with ADP and substrate. *Proceedings of the National Academy of Sciences*, *106*(21), 8471–8476. https://doi.org/10.1073/pnas.0903503106

Bertram, K., Agafonov, D. E., Dybkov, O., Haselbach, D., Leelaram, M. N., Will, C. L., Urlaub, H., Kastner, B., Lührmann, R., & Stark, H. (2017). Cryo-EM structure of a human spliceosome activated for step 2 of splicing. *Cell*, *170*(4), 701-713.e11. https://doi.org/10.1016/j.cell.2017.07.011

Booy, F. P., & Pawley, J. B. (1993). Cryo-crinkling: what happens to carbon films on copper grids at low temperature. *Ultramicroscopy*, *48*(3), 273–280. https://doi.org/10.1016/0304-3991(93)90101-3

Brehmer, D., Rüdiger, S., Gässler, C. S., Klostermeier, D., Packschies, L., Reinstein, J., Mayer, M. P., & Bukau, B. (2001). Tuning of chaperone activity of Hsp70 proteins by modulation of nucleotide exchange. *Nature Structural Biology*, *8*(5), 427–432. https://doi.org/10.1038/87588

Brilot, A. F., Chen, J. Z., Cheng, A., Pan, J., Harrison, S. C., Potter, C. S., Carragher, B., Henderson, R., & Grigorieff, N. (2012). Beam-induced motion of vitrified specimen on holey carbon film. *Journal of Structural Biology*, *177*, 630–637. https://doi.org/10.1016/j.jsb.2012.02.003

Butterwick, J. A., del Mármol, J., Kim, K. H., Kahlson, M. A., Rogow, J. A., Walz, T., & Ruta, V. (2018). Cryo-EM structure of the insect olfactory receptor Orco. *Nature*. https://doi.org/10.1038/s41586-018-0420-8

Carra, S., Seguin, S. J., Lambert, H., & Landry, J. (2008a). HspB8 chaperone activity toward poly(Q)-containing proteins depends on its association with Bag3, a stimulator of macroautophagy. *Journal of Biological Chemistry*, *283*(3), 1437–1444. https://doi.org/10.1074/jbc.M706304200

Carra, S., Seguin, S. J., & Landry, J. (2008b). HspB8 and Bag3: A new chaperone complex targeting misfolded proteins to macroautophagy. *Autophagy*, *4*(2), 237–239. https://doi.org/5407 [pii]

Carra, S., Sivilotti, M., Zobel, A. T. C., Lambert, H., Landry, J., Chávez Zobel, A. T., Lambert, H., Landry, J., Zobel, A. T. C., Lambert, H., & Landry, J. (2005). HspB8, a small heat shock protein mutated in human neuromuscular disorders, has in vivo chaperone activity in cultured cells. *Human Molecular Genetics*, *14*(12), 1659–1669. https://doi.org/10.1093/hmg/ddi174

Carrell, R. W., & Lomas, D. A. (1997). Conformational disease. *Lancet*, *350*(9071), 134–138. https://doi.org/10.1016/S0140-6736(97)02073-4

Carroni, M., & Saibil, H. R. (2016). Cryo electron microscopy to determine the structure of macromolecular complexes. *Methods*, *95*, 78–85. https://doi.org/10.1016/j.ymeth.2015.11.023

Caspers, G. J., Leunissen, J. A. M., & de Jong, W. W. (1995). The expanding small heat-shock protein family, and structure predictions of the conserved “α-crystallin domain.” *Journal of Molecular Evolution*, *40*(3), 238–248. https://doi.org/10.1007/BF00163229

Chari, A., Haselbach, D., Kirves, J.-M., Ohmer, J., Paknia, E., Fischer, N., Ganichkin, O., Möller, V., Frye, J. J., Petzold, G., Jarvis, M., Tietzel, M., Grimm, C., Peters, J.-M., Schulman, B. A., Tittmann, K., Markl, J., … Stark, H. (2015). ProteoPlex: stability optimization of macromolecular complexes by sparse-matrix screening of chemical space. *Nature Methods*, *12*(9), 859–865. https://doi.org/10.1038/nmeth.3493

Chen, J., Noble, A. J., Kang, J. Y., & Darst, S. (2019). Eliminating effects of particle adsorption to the air/water interface in single-particle cryo-electron microscopy: Bacterial RNA polymerase and CHAPSO. *Journal of Structural Biology: X*, *1*. https://doi.org/10.1101/457267

Chen, S., McMullan, G., Faruqi, A. R., Murshudov, G. N., Short, J. M., Scheres, S. H. W., & Henderson, R. (2013a). High-resolution noise substitution to measure overfitting and validate resolution in 3D structure determination by single particle electron cryomicroscopy. *Ultramicroscopy*, *135*, 24–35. https://doi.org/10.1016/j.ultramic.2013.06.004

Chen, Y., Yang, L.-N., Cheng, L., Tu, S., Guo, S.-J., Le, H.-Y., Xiong, Q., Mo, R., Li, C. Y., Jeong, J.-S., Jiang, L., Blackshaw, S., Bi, L.-J., Zhu, H., Tao, S.-C., & Ge, F. (2013b). BAG3 Interactome Analysis Reveals a New Role in Modulating Proteasome Activity. *Molecular & Cellular Proteomics : MCP*, 1–46. https://doi.org/10.1074/mcp.M112.025882

Chiang, H. L., Terlecky, S. R., Plant, C. P., & Dice, J. F. (1989). A role for a 70-kilodaton heat shock protein in lysosomal degradation of intracellular proteins. *Science*, *246*(4928), 382–385. https://doi.org/10.1126/science.2799391

Cho, H.-J., Hyun, J.-K., Kim, J.-G., Jeong, H. S., Park, H. N., You, D.-J., & Jung, H. S. (2013). Measurement of ice thickness on vitreous ice embedded cryo-EM grids: investigation of optimizing condition for visualizing macromolecules. *Journal of Analytical Science and Technology*, *4*(1), 7. https://doi.org/10.1186/2093-3371-4-7

Ciechanover, A., & Kwon, Y. T. (2015). Degradation of misfolded proteins in neurodegenerative diseases: therapeutic targets and strategies. *Exp Mol Med*, *47*(3), e147. https://doi.org/10.1038/emm.2014.117

Cole, J. L. (2004). Analysis of Heterogeneous Interactions. *Methods in Enzymology*, *384*(04), 212–232. https://doi.org/10.1016/S0076-6879(04)84013-8

Connell, P., Ballinger, C. A., Jiang, J., Wu, Y., Thompson, L. J., Hohfeld, J., & Patterson, C. (2001). The co-chaperone CHIP regulates protein triage decisions mediated by heat-shock proteins. *Nature Cell Biology*, *3*(1), 93–96. https://doi.org/10.1038/35050618

Craig, E. A. (2018). Hsp70 at the membrane: Driving protein translocation. *BMC Biology*, *16*(1), 1–11. https://doi.org/10.1186/s12915-017-0474-3

Crippa, V., Carra, S., Rusmini, P., Sau, D., Bolzoni, E., Bendotti, C., De Biasi, S., & Poletti, A. (2010a). A role of small heat shock protein B8 (HspB8) in the autophagic removal of misfolded proteins responsible for neurodegenerative diseases. *Autophagy*, *6*(7), 958–960. https://doi.org/10.4161/auto.6.7.13042

Crippa, V., D'Agostino, V. G., Cristofani, R., Rusmini, P., Cicardi, M. E., Messi, E., Loffredo, R., Pancher, M., Piccolella, M., Galbiati, M., Meroni, M., Cereda, C., Carra, S., Provenzani, A., & Poletti, A. (2016). Transcriptional induction of the heat shock protein B8 mediates the clearance of misfolded proteins responsible for motor neuron diseases. *Scientific Reports*, *6*(February), 22827. https://doi.org/10.1038/srep22827

Crippa, V., Sau, D., Rusmini, P., Boncoraglio, A., Onesto, E., Bolzoni, E., Galbiati, M., Fontana, E., Marino, M., Carra, S., Bendotti, C., de Biasi, S., & Poletti, A. (2010b). The small heat shock protein B8 (HspB8) promotes autophagic removal of misfolded proteins involved in amyotrophic lateral sclerosis (ALS). *Human Molecular Genetics*, *19*(17), 3440–3456. https://doi.org/10.1093/hmg/ddq257

Cristofani, R., Crippa, V., Rusmini, P., Cicardi, M. E., Meroni, M., Licata, N. V., Sala, G., Giorgetti, E., Grunseich, C., Galbiati, M., Piccolella, M., Messi, E., Ferrarese, C., Carra, S., & Poletti, A. (2017). Inhibition of retrograde transport modulates misfolded protein accumulation and clearance in motoneuron diseases. *Autophagy*, 00–00. https://doi.org/10.1080/15548627.2017.1308985

Cuéllar, J., Ludlam, W. G., Tensmeyer, N. C., Aoba, T., Dhavale, M., Santiago, C., Bueno-Carrasco, M. T., Mann, M. J., Plimpton, R. L., Makaju, A., Franklin, S., Willardson, B. M., & Valpuesta, J. M. (2019). Structural and functional analysis of the role of the chaperonin CCT in mTOR complex assembly. *Nature Communications*, *10*(1), 1–14. https://doi.org/10.1038/s41467-019-10781-1

Cuéllar, J., Martín-Benito, J., Scheres, S. H. W., Sousa, R., Moro, F., López-Viñas, E., Gómez-Puertas, P., Muga, A., Carrascosa, J. L., & Valpuesta, J. M. (2008). The structure of CCT-Hsc70 NBD suggests a mechanism for Hsp70 delivery of substrates to the chaperonin. *Nature Structural & Molecular Biology*, *15*(8), 858–864. https://doi.org/10.1038/nsmb.1464

D'Imprima, E., Floris, D., Joppe, M., Sánchez, R., Grininger, M., & Kühlbrandt, W. (2019). *Protein denaturation at the air-water interface and how to prevent it*. 1–18.

Danev, R., & Baumeister, W. (2016). Cryo-EM single particle analysis with the volta phase plate. *ELife*, *5*(MARCH2016), 1–14. https://doi.org/10.7554/eLife.13046

Danev, R., Buijsse, B., Khoshouei, M., Plitzko, J. M., & Baumeister, W. (2014). Volta potential phase plate for in-focus phase contrast transmission electron microscopy. *Proceedings of the National Academy of Sciences*, *111*(44). https://doi.org/10.1073/pnas.1418377111

de Duve, C., Pressman, B. C., Gianetto, R., Wattiaux, R., & Appelmans, F. (1955). Tissue fractionation studies. *Biochemical Journal*, *60*, 604–617. https://doi.org/10.1042/bj0600604

de la Rosa-Trevín, J. M., Quintana, A., del Cano, L., Zald?var, A., Foche, I., Guti?rrez, J., G?mez-Blanco, J., Burguet-Castell, J., Cuenca-Alba, J., Abrishami, V., Vargas, J., Ot?n, J., Sharov, G., Vilas, J. L., Navas, J., Conesa, P., Kazemi, M., … Carazo, J. M. (2016). Scipion: A software framework toward integration, reproducibility and validation in 3D electron microscopy. *Journal of Structural Biology*, *195*(1), 93–99. https://doi.org/10.1016/j.jsb.2016.04.010

Dechecchi, M. C., Tamanini, A., & Cabrini, G. (2018). Molecular basis of cystic fibrosis: from bench to bedside. *Annals of Translational Medicine*, *6*(17), 334–334. https://doi.org/10.21037/atm.2018.06.48

Delbecq, S. P., & Klevit, R. E. (2013). One size does not fit all: The oligomeric states of αb crystallin. *FEBS Letters*, *587*(8), 1073–1080. https://doi.org/10.1016/j.febslet.2013.01.021

Doong, H., Price, J., Kim, Y. S., Gasbarre, C., Probst, J., Liotta, L. A., Blanchette, J., Rizzo, K., & Kohn, E. (2000). *CAIR-1 / BAG-3 forms an EGF-regulated ternary complex with phospholipase C- g and Hsp70 / Hsc70*. (January), 4385–4395.

Doyle, S. M., Genest, O., & Wickner, S. (2013). Protein rescue from aggregates by powerful molecular chaperone machines. *Nature Reviews Molecular Cell Biology*, *14*(10), 617–629. https://doi.org/10.1038/nrm3660

Drulyte, I., Johnson, R. M., Hesketh, E. L., Hurdiss, D. L., Scarff, C. A., Porav, S. A., Ranson, N. A., Muench, S. P., & Thompson, R. F. (2018). Approaches to altering particle distributions in cryo-electron microscopy sample preparation. *Acta Crystallographica Section D Structural Biology*, *74*(6), 1–12. https://doi.org/10.1107/S2059798318006496

Dubochet, J., Adrian, M., Chang, J.-J., Homo, J.-C., Lepault, J., McDowall, A. W., & Schultz, P. (1988). Cryo-electron microscopy of vitrified specimens. *Quarterly Reviews of Biophysics*, *21*(2), 129–228. https://doi.org/10.1017/S0033583500004297

English, C. A., Sherman, W., Meng, W., & Gierasch, L. M. (2017). The Hsp70 interdomain linker is a dynamic switch that enables allosteric communication between two structured domains. *Journal of Biological Chemistry*, *292*(36), 14765–14774. https://doi.org/10.1074/jbc.M117.789313

Erickson, H. P. (2009). Size and shape of protein molecules at the nanometer level determined by sedimentation, gel filtration, and electron microscopy. *Biological Procedures Online*, *11*(1), 32–51. https://doi.org/10.1007/s12575-009-9008-x

Fan, X., Wang, J., Zhang, X., Yang, Z., Zhang, J.-C., Zhao, L., Peng, H.-L., Lei, J., & Wang, H.-W. (2019). Single particle cryo-EM reconstruction of 52 kDa streptavidin at 3.2 Angstrom resolution. *Nature Communications*, *10*(2386), 1–11. https://doi.org/10.1038/s41467-019-10368-w

Feng, X., Fu, Z., Kaledhonkar, S., Jia, Y., Shah, B., Jin, A., Liu, Z., Sun, M., Chen, B., Grassucci, R. A., Ren, Y., Jiang, H., Frank, J., & Lin, Q. (2017). A Fast and Effective Microfluidic Spraying-Plunging Method for High-Resolution Single-Particle Cryo-EM. *Structure*, *25*(4), 663-670.e3. https://doi.org/10.1016/j.str.2017.02.005

Feng, Y., He, D., Yao, Z., & Klionsky, D. J. (2014). The machinery of macroautophagy. *Cell*

Research, *24*(1), 24–41. https://doi.org/10.1038/cr.2013.168

Fernández-Fernández, M. R., Gragera, M., Ochoa-Ibarrola, L., Quintana-Gallardo, L., & Valpuesta, J. M. (2017). Hsp70 - a master regulator in protein degradation. *FEBS Letters*, *591*, 2648–2660. https://doi.org/10.1002/1873-3468.12751

Fernández-Fernández, M. R., Sot, B., & Valpuesta, J. M. (2016). Molecular chaperones: Functional mechanisms and nanotechnological applications. *Nanotechnology*, *27*(32). https://doi.org/10.1088/0957-4484/27/32/324004

Fernández-Fernández, M. R., & Valpuesta, J. M. (2018). Hsp70 chaperone: a master player in protein homeostasis. *F1000Research*, *7*(0), 1497. https://doi.org/10.12688/f1000research.15528.1

Fernandez-Fernandez, M. R., Veprintsev, D. B., & Fersht, A. R. (2005). Proteins of the S100 family the regulate the oligomerization of p53 tumor suppressor. *Proceedings of the National Academy of Sciences of the United States of America*, *102*(13), 4735–4740. https://doi.org/10.1073/pnas.0501459102

Fontaine, J. M., Sun, X., Benndorf, R., & Welsh, M. J. (2005). Interactions of HSP22 (HSPB8) with HSP20, αB-crystallin, and HSPB3. *Biochemical and Biophysical Research Communications*, *337*(3), 1006–1011. https://doi.org/10.1016/j.bbrc.2005.09.148

Frydman, J. (2001). *FOLDING OF NEWLY TRANSLATED PROTEINS IN VIVO: The Role of Molecular Chaperones*.

Fuchs, M., Poirier, D. J., Seguin, S. J., Lambert, H., Carra, S., Charette, S. J., Landry, J., Mearini, G., Schlossarek, S., Willis, M. S., Carrier, L., Garrido, C., Brunet, M., Didelot, C., Zermati, Y., Schmitt, E., Kroemer, G., … Gibson, T. J. (2010). Identification of the key structural motifs involved in HspB8/HspB6-Bag3 interaction. *The Biochemical Journal*, *425*(1), 245–255. https://doi.org/10.1042/BJ20090907

Gamerdinger, M., Carra, S., & Behl, C. (2011a). Emerging roles of molecular chaperones and co-chaperones in selective autophagy: Focus on BAG proteins. *Journal of Molecular Medicine*, *89*(12), 1175–1182. https://doi.org/10.1007/s00109-011-0795-6

Gamerdinger, M., Hajieva, P., Kaya, A. M., Wolfrum, U., Hartl, F. U., Behl, C., Arndt, V., Daniel, C., Nastainczyk, W., Alberti, S., Hohfeld, J., Balaban, R., Nemoto, S., Finkel, T., Balch, W., Morimoto, R., Dillin, A., … Hartl, F. (2009). Protein quality control during aging involves recruitment of the macroautophagy pathway by BAG3. *The EMBO Journal*, *28*(7), 889–901. https://doi.org/10.1038/emboj.2009.29

Gamerdinger, M., Kaya, A. M., Wolfrum, U., Clement, A. M., Behl, C., Arndt, V., Gamerdinger, M., Clement, A., Behl, C., Gamerdinger, M., Hajieva, P., Kaya, A., Wolfrum, U., Hartl, F., Behl, C., García-Mata, R., Bebök, Z., … Clement, A. (2011b). BAG3 mediates chaperone-based aggresome-targeting and selective autophagy of misfolded proteins. *EMBO Reports*, *12*(2), 149–156. https://doi.org/10.1038/embor.2010.203

Ganassi, M., Mateju, D., Bigi, I., Mediani, L., Poser, I., Lee, H. O., Seguin, S. J., Morelli, F. F., Vinet, J., Leo, G., Pansarasa, O., Cereda, C., Poletti, A., Alberti, S., & Carra, S. (2016). A Surveillance Function of the HSPB8-BAG3-HSP70 Chaperone Complex Ensures Stress Granule Integrity and Dynamism. *Molecular Cell*, *63*(5). https://doi.org/10.1016/j.molcel.2016.07.021

García-Nafría, J., Lee, Y., Bai, X., Carpenter, B., & Tate, C. G. (2018). Cryo-EM structure of the adenosine A2A receptor coupled to an engineered heterotrimeric G protein. *ELife*, *7*, e35946. https://doi.org/10.7554/eLife.35946

Ghaoui, R., Palmio, J., Brewer, J., Lek, M., Needham, M., Evilä, A., Hackman, P., Jonson, P. H., Penttilä, S., Vihola, A., Huovinen, S., Lindfors, M., Davis, R. L., Waddell, L., Kaur, S., Yiannikas, C., North, K., … Udd, B. (2016). Mutations in HSPB8 causing a new phenotype of distal myopathy and motor neuropathy. *Neurology*, *86*(4), 391–398. https://doi.org/10.1212/WNL.0000000000002324

Gilks, N., Kedersha, N., Ayodele, M., Shen, L., Stoecklin, G., Dember, L. M., & Anderson, P. (2004). Stress Granule Assembly Is Mediated by Prion-like Aggregation of TIA-1. *Molecular Biology of the Cell*, *15*(12), 5383–5398. https://doi.org/10.1091/mbc.e04-08-0715

Glaeser, R. M. (2018). Proteins, interfaces, and cryo-EM grids. *Current Opinion in Colloid and Interface Science*, *34*, 1–8. https://doi.org/10.1016/j.cocis.2017.12.009

Glaeser, R. M., Han, B.-G., Csencsits, R., Killilea, A., Pulk, A., & Cate, J. H. D. (2016). Factors that Influence the Formation and Stability of Thin, Cryo-EM Specimens. *Biophysical Journal*, *110*, 749–755. https://doi.org/10.1016/j.bpj.2015.07.050

Glover, J. R., & Lindquist, S. (1998). Hsp104, Hsp70, and Hsp40: A Novel Chaperone System that Rescues Previously Aggregated Proteins in chaperone-assisted reactivation of unfolded proteins in vitro. Thus, Hsp104's ability to promote the resolubili- zation of heat-damaged proteins in vivo migh. *Cell*, *94*, 73–82. Retrieved from http://lindquistlab.wi.mit.edu/PDFs/Glover1998Cell.pdf

Götze, M., Pettelkau, J., Schaks, S., Bosse, K., Ihling, C. H., Krauth, F., Fritzsche, R., Kühn, U., & Sinz, A. (2012). StavroX-A software for analyzing crosslinked products in protein interaction studies. *Journal of the American Society for Mass Spectrometry*, *23*(1), 76–87. https://doi.org/10.1007/s13361-011-0261-2

Greenfield, N. J. (2006). *Using circular dichroism spectra to estimate protein secondary structure*. https://doi.org/10.1038/nprot.2006.202

Hansen, L. K., O'Leary, J. J., Skubitz, A. P. N., Furcht, L. T., & McCarthy, J. B. (1995). Identification of a homologous heparin binding peptide sequence present in fibronectin and the 70 kDa family of heat-shock proteins. *Biochimica et Biophysica Acta (BBA)/Protein Structure and Molecular*, *1252*(1), 135–145. https://doi.org/10.1016/0167-4838(95)00113-9

Hartl, F. U., Bracher, A., & Hayer-Hartl, M. (2011). Molecular chaperones in protein folding and proteostasis. *Nature*, *475*(7356), 324–332. https://doi.org/10.1038/nature10317

Haslbeck, M., & Vierling, E. (2015). A first line of stress defense: Small heat shock proteins and their function in protein homeostasis. *Journal of Molecular Biology*, *427*(7), 1537–1548. https://doi.org/10.1016/j.jmb.2015.02.002

Herzik, M. A., Wu, M., & Lander, G. C. (2017). Achieving better-than-3-Å resolution by single-particle cryo-EM at 200 keV. *Nature Methods*, *14*(11), 1075–1078. https://doi.org/10.1038/nmeth.4461

Homma, S., Iwasaki, M., Shelton, G. D., Engvall, E., Reed, J. C., & Takayama, S. (2006). BAG3 Deficiency Results in Fulminant Myopathy and Early Lethality. *The American Journal of Pathology*, *169*(3), 761–773. https://doi.org/10.2353/ajpath.2006.060250

Horst, M., Knecht, E. C., & Schu, P. V. (1999). Import into and Degradation of Cytosolic Proteins by Isolated Yeast Vacuoles. *Molecular Biology of the Cell*, *10*(9), 2879–2889. https://doi.org/10.1091/mbc.10.9.2879

Inoue, H., Nojima, H., & Okayma, H. (1990). High efficiency transformation of Escherichia coli with plasmids. *Gene*, *96*, 23–28.

Irobi, J., Impe, K. Van, Seeman, P., Jordanova, A., Dierick, I., Verpoorten, N., Michalik, A., Vriendt, E. De, Jacobs, A., Gerwen, V. Van, Vennekens, K., Mazanec, R., Tournev, I., Hilton-Jones, D., Talbot, K., Kremensky, I., Bosch, L. Van Den, … Timmerman, V. (2004). Hot-spot residue in small heat-shock protein 22 causes distal motor neuropathy. *Nature Genetics*, *36*(6), 597–601. https://doi.org/10.1038/ng1328

Johansen, T., & Lamark, T. (2011). Selective autophagy mediated by autophagic adapter proteins. *Autophagy*, *7*(3), 279–296. https://doi.org/10.4161/auto.7.3.14487

Kabbage, M., & Dickman, M. B. (2008). The BAG proteins: A ubiquitous family of chaperone regulators. *Cellular and Molecular Life Sciences*, *65*(9), 1390–1402. https://doi.org/10.1007/s00018-008-7535-2

Kakkar, V., Meister-Broekema, M., Minoia, M., Carra, S., & Kampinga, H. H. (2014). Barcoding heat shock proteins to human diseases: looking beyond the heat shock response. *Disease Models & Mechanisms*, *7*(4), 421–434. https://doi.org/10.1242/dmm.014563

Kampinga, H. H., Hageman, J., Vos, M. J., Kubota, H., Tanguay, R. M., Bruford, E. A., Cheetham, M. E., Chen, B., & Hightower, L. E. (2009). Guidelines for the nomenclature of the human heat shock proteins. *Cell Stress and Chaperones*, *14*(1), 105–111. https://doi.org/10.1007/s12192-008-0068-7

Kappé, G., Verschuure, P., Philipsen, R. L. ., Staalduinen, A. A., Van de Boogaart, P., Boelens, W. C., & De Jong, W. W. (2001). Characterization of two novel human small heat shock proteins: protein kinase-related HspB8 and testis-specific HspB9. *Biochimica et Biophysica Acta (BBA) - Gene Structure and Expression*, *1520*(1), 1–6. https://doi.org/10.1016/S0167-4781(01)00237-8

Kastner, B., Fischer, N., Golas, M. M., Sander, B., Dube, P., Boehringer, D., Hartmuth, K., Deckert, J., Hauer, F., Wolf, E., Uchtenhagen, H., Urlaub, H., Herzog, F., Peters, J. M., Poerschke, D., Lührmann, R., & Stark, H. (2007). GraFix: sample preparation for single-particle electron cryomicroscopy. *Nature Methods*, *5*(1), 53–55. https://doi.org/10.1038/nmeth1139

Kathage, B., Gehlert, S., Ulbricht, A., Lüdecke, L., Tapia, V. E., Orfanos, Z., Wenzel, D., Bloch, W., Volkmer, R., Fleischmann, B. K., Fürst, D. O., Höhfeld, J., L??decke, L., Tapia, V. E., Orfanos, Z., Wenzel, D., Bloch, W., … H??hfeld, J. (2017). The cochaperone BAG3 coordinates protein synthesis and autophagy under mechanical strain through spatial regulation of mTORC1. *Biochimica et Biophysica Acta - Molecular Cell Research*, *1864*(1), 62–75. https://doi.org/10.1016/j.bbamcr.2016.10.007

Kaushik, S., & Cuervo, A. M. (2012a). Chaperone-mediated autophagy: A unique way to enter the lysosome world. *Trends in Cell Biology*, *22*(8), 407–417. https://doi.org/10.1016/j.tcb.2012.05.006

Kaushik, S., & Cuervo, A. M. (2012b). Chaperones in autophagy. *Pharmacological Research*, *66*(6), 484–493. https://doi.org/10.1016/j.phrs.2012.10.002

Kedersha, N. L., & Anderson, P. (2002). Stress granules: sites of mRNA triage that regulate mRNA stability and translatability. *Biochemical Society Transactions*, *30*(5), A117.1-A117. https://doi.org/10.1042/bst030a117

Kettern, N., Dreiseidler, M., Tawo, R., & Höhfeld, J. (2010). Chaperone-assisted degradation: Multiple paths to destruction. *Biological Chemistry*, *391*(5), 481–489. https://doi.org/10.1515/BC.2010.058

Khoshouei, M., Radjainia, M., Baumeister, W., & Danev, R. (2016). Cryo-EM structure of haemoglobin at 3.2 A determined with the Volta phase plate. *BioRxiv*, *8*(May), 087841. https://doi.org/10.1101/087841

Kim, M. V., Kasakov, A. S., Seit-Nebi, A. S., Marston, S. B., & Gusev, N. B. (2006). Structure and properties of K141E mutant of small heat shock protein HSP22 (HspB8, H11) that is expressed in human neuromuscular disorders. *Archives of Biochemistry and Biophysics*, *454*(1), 32–41. https://doi.org/10.1016/j.abb.2006.07.014

Kim, M. V., Seit-Nebi, A. S., Marston, S. B., & Gusev, N. B. (2004). Some properties of human small heat shock protein Hsp22 (H11 or HspB8). *Biochemical and Biophysical Research Communications*, *315*(4), 796–801. https://doi.org/10.1016/j.bbrc.2004.01.130

Kimanius, D., Forsberg, B. O., Scheres, S. H. W., & Lindahl, E. (2016). Accelerated cryo-EM structure determination with parallelisation using GPUS in RELION-2. *ELife*, *5*, 1–21. https://doi.org/10.7554/eLife.18722

Kityk, R., Kopp, J., & Mayer, M. P. (2018). Molecular Mechanism of J-Domain-Triggered ATP Hydrolysis by Hsp70 Chaperones. *Molecular Cell*, *69*(2), 227-237.e4. https://doi.org/10.1016/j.molcel.2017.12.003

Kityk, R., Kopp, J., Sinning, I., & Mayer, M. P. (2012). Structure and Dynamics of the ATP-Bound Open Conformation of Hsp70 Chaperones. *Molecular Cell*, *48*(6), 863–874. https://doi.org/10.1016/j.molcel.2012.09.023

Klimek, C., Kathage, B., Wördehoff, J., & Höhfeld, J. (2017). BAG3-mediated proteostasis at a glance. *Journal of Cell Science*, (August), jcs.203679. https://doi.org/10.1242/jcs.203679

Knezevic, T., Myers, V. D., Gordon, J., Tilley, D. G., Sharp, T. E., Wang, J. F., Khalili, K., Cheung, J. Y., & Feldman, A. M. (2015). BAG3: a new player in the heart failure paradigm. *Heart Failure Reviews*, *20*(4), 423–434. https://doi.org/10.1007/s10741-015-9487-6

Kremer, J. R., Mastronarde, D. N., & McIntosh, J. R. (1996). *Computer Visualization of Three Dimensional Im.Pdf*. *116*, 71–76.

Kunzt, J. B., Schwarz, H., & Mayer, A. (2004). Determination of Four Sequential Stages during Microautophagy in Vitro. *Journal of Biological Chemistry*, *279*(11), 9987–9996. https://doi.org/10.1074/jbc.M307905200

Laue, T. M. (2000). Analytical Ultracentrifugation. *Current Protocols in Protein Science*, (1996), 1–9.

Li, X., Mooney, P., Zheng, S., Booth, C. R., Braunfeld, M. B., Gubbens, S., Agard, D. A., & Cheng, Y. (2013). Electron counting and beam-induced motion correction enable near-atomic-resolution single-particle cryo-EM. *Nature Methods*, *10*(6). https://doi.org/10.1038/nmeth.2472

Lippai, M., & Low, P. (2014). The role of the selective adaptor p62 and ubiquitin-like proteins in autophagy. *BioMed Research International*, *2014*. https://doi.org/10.1155/2014/832704

Liu, H., Jin, L., Koh, S. B. S., Atanasov, I., Schein, S., Wu, L., & Zhou, Z. H. (2010). Atomic Structure of Human Adenovirus by Cryo-EM Reveals Interactions Among Protein Networks. *Science*, *329*(August), 1038–1043.

Llorca, O., McCormack, E. A., Hynes, G., Grantham, J., Cordell, J., Carrascosa, J. L., Willison, K. R., Fernandez, J. J., & Valpuesta, J. M. (1999). Eukaryotic type II chaperonin CCT interacts with actin through specific subunits. *Nature*, *402*(6762), 693–696. https://doi.org/10.1038/45294

Loveland, A. B., Demo, G., Grigorieff, N., & Korostelev, A. A. (2017). Ensemble cryo-EM elucidates the mechanism of translation fidelity. *Nature Publishing Group*, *546*(7656), 113–117. https://doi.org/10.1038/nature22397

Mandrioli, J., Crippa, V., Cereda, C., Bonetto, V., Zucchi, E., Gessani, A., Ceroni, M., Chio, A., D'Amico, R., Monsurrò, M. R., Riva, N., Sabatelli, M., Silani, V., Simone, I. L., Sorarù, G., Provenzani, A., D'Agostino, V. G., … Poletti, A. (2019). Proteostasis and ALS: Protocol for a phase II, randomised, double-blind, placebo-controlled, multicentre clinical trial for colchicine in ALS (Co-ALS). *BMJ Open*, *9*(5), 1–12. https://doi.org/10.1136/bmjopen-2018-028486

Maniatis, T., Fritsch, E., & Sambrook, J. (1982). *Molecular cloning: a laboratory manual* (Cold Spring Harbor Laboratory Cold Spring Harbor, ed.). Nueva York.

Marzella, L., Ahlberg, J., Glaumann, H., J. Ahlberg, & Glaumann, H. (1981). Autophagy, heterophagy, microautophagy and crinophagy as the means for intracellular degradation. *Virchows Archiv B Cell Pathology Including Molecular Pathology*, *36*(1), 219–234. https://doi.org/10.1007/BF02912068

Masiulis, S., Desai, R., Uchański, T., Serna Martin, I., Laverty, D., Karia, D., Malinauskas, T., Zivanov, J., Pardon, E., Kotecha, A., Steyaert, J., Miller, K. W., & Aricescu, A. R. (2019). GABAA receptor signalling mechanisms revealed by structural pharmacology. *Nature*. https://doi.org/10.1038/s41586-018-0832-5

Mastronarde, D. N. (2005). Automated electron microscope tomography using robust prediction of specimen movements. *Journal of Structural Biology*, *152*(1), 36–51. https://doi.org/10.1016/j.jsb.2005.07.007

Mateju, D., Franzmann, T. M., Patel, A., Kopach, A., Boczek, E. E., Maharana, S., Lee, H. O., Carra, S., Hyman, A. A., & Alberti, S. (2017). An aberrant phase transition of stress granules triggered by misfolded protein and prevented by chaperone function. *The EMBO Journal*, *36*(12), 1669–1687. https://doi.org/10.15252/embj.201695957

McCollum, A. K., Casagrande, G., Kohn, E. C., Doong, H., Vrailas, A., Kohn, E. C., Fuchs, M., Poirier, D. J., Seguin, S., Lambert, H., Carra, S., Charrette, S. J., Landry, J., Doong, H., Price, J., Kim, Y. S., Gasbarre, C., … Engel, A. G. (2010). Caught in the middle: the role of Bag3 in disease. *The Biochemical Journal*, *425*(1), e1-3. https://doi.org/10.1042/BJ20091739

Mchaourab, H. S., Dodson, E. K., & Koteiche, H. A. (2002). Mechanism of chaperone function in small heat shock proteins: Two-mode binding of the excited states of T4 lysozyme mutants by αA-crystallin. *Journal of Biological Chemistry*, *277*(43), 40557–40566. https://doi.org/10.1074/jbc.M206250200

Meister-Broekema, M., Freilich, R., Jagadeesan, C., Rauch, J. N., Bengoechea, R., Motley, W. W., Kuiper, E. F. E., Minoia, M., Furtado, G. V., van Waarde, M. A. W. H., Bird, S. J., Rebelo, A., Zuchner, S., Pytel, P., Scherer, S. S., Morelli, F. F., Carra, S., … Kampinga, H. H. (2018). Myopathy associated BAG3 mutations lead to protein aggregation by stalling Hsp70 networks. *Nature Communications*, *9*(1), 1–14. https://doi.org/10.1038/s41467-018-07718-5

Merkley, E. D., Rysavy, S., Kahraman, A., Hafen, R. P., Daggett, V., & Adkins, J. N. (2014). Distance restraints from crosslinking mass spectrometry: Mining a molecular dynamics simulation database to evaluate lysine-lysine distances. *Protein Science*, *23*(6), 747–759. https://doi.org/10.1002/pro.2458

Minoia, M., Boncoraglio, A., Vinet, J., Morelli, F. F., Brunsting, J. F., Poletti, A., Krom, S., Reits, E., Kampinga, H. H., & Carra, S. (2014). BAG3 induces the sequestration of proteasomal clients into cytoplasmic puncta Implications for a proteasome-to-autophagy switch. *Autophagy*, *10*(9), 1603–1621. https://doi.org/10.4161/auto.29409

Mogk, A., Bukau, B., & Kampinga, H. H. (2018). Cellular Handling of Protein Aggregates by Disaggregation Machines. *Molecular Cell*, *69*(2), 214–226. https://doi.org/10.1016/j.molcel.2018.01.004

Molliex, A., Temirov, J., Lee, J., Coughlin, M., Kanagaraj, A. P., Kim, H. J., Mittag, T., & Taylor, J. P. (2015). Phase Separation by Low Complexity Domains Promotes Stress Granule Assembly and Drives Pathological Fibrillization. *Cell*, *163*(1), 123–133. https://doi.org/10.1016/J.CELL.2015.09.015

Morán Luengo, T., Kityk, R., Mayer, M. P., & Rüdiger, S. G. D. (2018). Hsp90 Breaks the Deadlock of the Hsp70 Chaperone System. *Molecular Cell*, *70*(3), 545-552.e9. https://doi.org/10.1016/j.molcel.2018.03.028

Morozova, K., Clement, C. C., Kaushik, S., Stiller, B., Arias, E., Ahmad, A., Rauch, J. N., Chatterjee, V., Melis, C., Scharf, B., Gestwicki, J. E., Cuervo, A. M., Zuiderweg, E. R. P., & Santambrogio, L. (2016). Structural and biological interaction of HSC-70 protein with phosphatidylserine in endosomal microautophagy. *Journal of Biological Chemistry*, *291*(35), 18096–18106. https://doi.org/10.1074/jbc.M116.736744

Murakami, T., Qamar, S., Lin, J. Q., Schierle, G. S. K., Rees, E., Miyashita, A., Costa, A. R., Dodd, R. B., Chan, F. T. S., Michel, C. H., Kronenberg-Versteeg, D., Li, Y., Yang, S.-P., Wakutani, Y., Meadows, W., Ferry, R. R., Dong, L., … St George-Hyslop, P. (2015). ALS/FTD Mutation-Induced Phase Transition of FUS Liquid Droplets and Reversible Hydrogels into Irreversible Hydrogels Impairs RNP Granule Function. *Neuron*, *88*(4), 678–690. https://doi.org/10.1016/J.NEURON.2015.10.030

Murata, K., & Wolf, M. (2018). Cryo-electron microscopy for structural analysis of dynamic biological macromolecules. *Biochimica et Biophysica Acta - General Subjects*, *1862*(2), 324–334. https://doi.org/10.1016/j.bbagen.2017.07.020

Nakane, T., Kimanius, D., Lindahl, E., & Scheres, S. H. W. (2018). Characterisation of molecular motions in cryo-EM single-particle data by multi-body refinement in RELION. *BioRxiv*, 286856. https://doi.org/10.1101/286856

Nakhro, K., Park, J. M., Kim, Y. J., Yoon, B. R., Yoo, J. H., Koo, H., Choi, B. O., & Chung, K. W. (2013). A novel Lys141Thr mutation in small heat shock protein 22 (HSPB8) gene in Charcot-Marie-Tooth disease type 2L. *Neuromuscular Disorders*, *23*(8), 656–663. https://doi.org/10.1016/j.nmd.2013.05.009

Naydenova, K., Peet, M. J., & Russo, C. J. (2019). Multifunctional graphene supports for electron cryomicroscopy. *Proceedings of the National Academy of Sciences of the United States of America*, *116*(24), 11718–11724. https://doi.org/10.1073/pnas.1904766116

Noble, A. J., Dandey, V. P., Wei, H., Brasch, J., Chase, J., Acharya, P., Tan, Y. Z., Zhang, Z., Kim, L. Y., Scapin, G., Rapp, M., Eng, E. T., Rice, W. J., Cheng, A., Negro, C. J., Shapiro, L., Kwong, P. D., … Carragher, B. (2018a). Routine single particle CryoEM sample and grid characterization by tomography. *ELife*, *7*, e34257. https://doi.org/10.7554/eLife.34257

Noble, A. J., Wei, H., Dandey, V. P., Zhang, Z., Potter, C. S., Electron, S., York, N., Biology, S., States, U., & Biophysics, M. (2018b). Reducing effects of particle adsorption to the air-water interface in cryoEM. *Nature Methods*, *15*, 793–795. https://doi.org/10.1101/288340

Pantelic, R. S., Meyer, J. C., Kaiser, U., Baumeister, W., & Plitzko, J. M. (2010). Graphene oxide: A substrate for optimizing preparations of frozen-hydrated samples. *Journal of Structural Biology*, *170*(1), 152–156. https://doi.org/10.1016/j.jsb.2009.12.020

Pardon, E., Laeremans, T., Triest, S., Rasmussen, S. G. F., Wohlkönig, A., Ruf, A., Muyldermans, S., Hol, W. G. J., Kobilka, B. K., & Steyaert, J. (2014). A general protocol for the generation of Nanobodies for structural biology. *Nature Protocols*, *9*(3), 674–693. https://doi.org/10.1038/nprot.2014.039

Passmore, L. A., & Russo, C. J. (2016). Specimen Preparation for High-Resolution Cryo-EM. In *The Resolution Revolution: Recent Advances In cryoEM* (1st ed., Vol. 579). https://doi.org/10.1016/bs.mie.2016.04.011

Patel, A., Lee, H. O., Jawerth, L., Maharana, S., Jahnel, M., Hein, M. Y., Stoynov, S., Mahamid, J., Saha, S., Franzmann, T. M., Pozniakovski, A., Poser, I., Maghelli, N., Royer, L. A., Weigert, M., Myers, E. W., Grill, S., … Alberti, S. (2015). A Liquid-to-Solid Phase Transition of the ALS Protein FUS Accelerated by Disease Mutation. *Cell*, *162*(5), 1066–1077. https://doi.org/10.1016/J.CELL.2015.07.047

Pettersen, E. F., Goddard, T. D., Huang, C. C., Couch, G. S., Greenblatt, D. M., Meng, E. C., & Ferrin, T. E. (2004). UCSF Chimera - A visualization system for exploratory research and analysis. *Journal of Computational Chemistry*, *25*(13), 1605–1612. https://doi.org/10.1002/jcc.20084

Powers, E. T., Morimoto, R. I., Dillin, A., Kelly, J. W., & Balch, W. E. (2009). Biological and Chemical Approaches to Diseases of Proteostasis Deficiency. *Annual Review of Biochemistry*, *78*(1), 959–991. https://doi.org/10.1146/annurev.biochem.052308.114844

Punjani, A., Rubinstein, J. L., Fleet, D. J., & Brubaker, M. A. (2017). cryoSPARC: algorithms for rapid unsupervised cryo-EM structure determination. *Nature Methods*, *14*(3), 290–296. https://doi.org/10.1038/nmeth.4169

Qi, R., Sarbeng, E. B., Liu, Q., Le, K. Q., Xu, X., Xu, H., Yang, J., Wong, J. L., Vorvis, C., Hendrickson, W. A., Zhou, L., & Liu, Q. (2013). Allosteric opening of the polypeptide-binding site when an Hsp70 binds ATP. *Nature Structural and Molecular Biology*, *20*(7), 900–907. https://doi.org/10.1038/nsmb.2583

Quintana-Gallardo, L., Martín-Benito, J., Marcilla, M., Espadas, G., Sabidó, E., & Valpuesta, J. M. (2019). The cochaperone CHIP marks Hsp70- and Hsp90-bound substrates for degradation through a very flexible mechanism. *Scientific Reports*, *9*(1), 1–16. https://doi.org/10.1038/s41598-019-41060-0

Rauch, J. N., & Gestwicki, J. E. (2014). Binding of human nucleotide exchange factors to heat shock protein 70 (Hsp70) generates functionally distinct complexes in vitro. *Journal of Biological Chemistry*, *289*(3), 1402–1414. https://doi.org/10.1074/jbc.M113.521997

Rauch, J. N., Tse, E., Freilich, R., Mok, S.-A., Makley, L. N., Southworth, D. R., & Gestwicki, J. E. (2016a). BAG3 is a modular, scaffolding protein that physically links heat shock protein 70 (Hsp70) to the small heat shock proteins. *Journal of Molecular Biology*, *70*. https://doi.org/10.1016/j.jmb.2016.11.013

Rauch, J. N., Zuiderweg, E. R. P., & Gestwicki, J. E. (2016b). Non-canonical Interactions between heat shock cognate protein 70 (Hsc70) and Bcl2-associated anthanogene (BAG) Co-chaperones are important for client release. *Journal of Biological Chemistry*, *291*(38), 19848–19857. https://doi.org/10.1074/jbc.M116.742502

Rauhut, R., Fabrizio, P., Dybkov, O., Hartmuth, K., Pena, V., Chari, A., Kumar, V., Lee, C. T., Urlaub, H., Kastner, B., Stark, H., & Lúhrmann, R. (2016). Molecular architecture of the Saccharomyces cerevisiae activated spliceosome. *Science*, *353*(6306), 1399–1405. https://doi.org/10.1126/science.aag1906

Ravikumar, B., Duden, R., & Rubinsztein, D. C. (2002). Aggregate-prone proteins with polyglutamine and polyalanine expansions are degraded by autophagy. *Human Mol Genet*, *11*(9), 1107–1117. https://doi.org/10.1093/hmg/11.9.1107

Razinkov, I., Dandey, V. P., Wei, H., Zhang, Z., Melnekoff, D., Rice, W. J., Wigge, C., Potter, C. S., & Carragher, B. (2016). A new method for vitrifying samples for cryoEM. *Journal of Structural Biology*, *195*(2), 190–198. https://doi.org/10.1016/j.jsb.2016.06.001

Robberecht, W., & Philips, T. (2013). *The changing scene of amyotrophic lateral sclerosis*. https://doi.org/10.1038/nrn3430

Röhl, A., Wengler, D., Madl, T., Lagleder, S., Tippel, F., Herrmann, M., Hendrix, J., Richter, K., Hack, G., Schmid, A. B., Kessler, H., Lamb, D. C., & Buchner, J. (2015). Hsp90 regulates the dynamics of its cochaperone Sti1 and the transfer of Hsp70 between modules. *Nature Communications*, *6*. https://doi.org/10.1038/ncomms7655

Rohou, A., & Grigorieff, N. (2015). CTFFIND4: Fast and accurate defocus estimation from electron micrographs. *Journal of Structural Biology*, *192*(2), 216–221. https://doi.org/10.1016/j.jsb.2015.08.008

Rosati, A., Graziano, V., De Laurenzi, V., Pascale, M., & Turco, M. C. (2011). BAG3: A multifaceted protein that regulates major cell pathways. *Cell Death and Disease*, *2*(4), e141-6. https://doi.org/10.1038/cddis.2011.24

Rosenzweig, R., Moradi, S., Zarrine-Afsar, A., Glover, J. R., & Kay, L. E. (2013). Unraveling the Mechanism of Protein Disaggregation Through a ClpB-DnaK Interaction. *Science*, *1080*(March), 1–4. https://doi.org/10.1126/science.1233066

Rout, A. K., Strub, M. P., Piszczek, G., & Tjandra, N. (2014). Structure of transmembrane domain of lysosome-associated membrane protein type 2a (LAMP-2A) reveals key features for substrate specificity in chaperone-mediated autophagy. *Journal of Biological Chemistry*, *289*(51), 35111–35123. https://doi.org/10.1074/jbc.M114.609446

Rüdiger, S., Germeroth, L., Schneider-Mergener, J., & Bukau, B. (1997). Substrate specificity of the DnaK chaperone determined by screening cellulose-bound peptide libraries respect to the bound folding conformer are only partly. *The EMBO Journal*, *16*(7), 1501–1507. Retrieved from https://www.ncbi.nlm.nih.gov/pmc/articles/PMC1169754/pdf/001501.pdf

Russo, C. J., & Passmore, L. A. (2016). *Ultrastable gold substrates: Properties of a support for high-resolution electron cryomicroscopy of biological specimens*. https://doi.org/10.1016/j.jsb.2015.11.006

Sahu, R., Kaushik, S., Clement, C. C., Cannizzo, E. S., Scharf, B., Follenzi, A., Potolicchio, I., Nieves, E., Cuervo, A. M., & Santambrogio, L. (2011). Microautophagy of Cytosolic Proteins by Late Endosomes. *Developmental Cell*, *20*(1), 131–139. https://doi.org/10.1016/j.devcel.2010.12.003

Savva, C. G., Clark, A. R., Naylor, C. E., Popoff, M. R., Moss, D. S., Basak, A. K., Titball, R. W., & Bokori-Brown, M. (2019). The pore structure of Clostridium perfringens epsilon toxin. *Nature Communications*, *10*(1), 25–28. https://doi.org/10.1038/s41467-019-10645-8

Schägger, H., Cramer, W. A., & von Jagow, G. (1994). Analysis of Molecular Masses and Oligomeric States of Protein Complexes by Blue Native Electrophoresis and Isolation of Membrane Protein Complexes by Two-Dimensional Native Electrophoresis. *Analytical Biochemistry*, *217*, 220–230.

Scheres, S. H. W. (2012). RELION: Implementation of a Bayesian approach to cryo-EM structure determination. *Journal of Structural Biology*, *180*(3), 519–530. https://doi.org/10.1016/j.jsb.2012.09.006

Scheres, S. H. W. (2016). Processing of Structurally Heterogeneous Cryo-EM Data in RELION. In *Methods in Enzymology* (1st ed., Vol. 579). https://doi.org/10.1016/bs.mie.2016.04.012

Schubert, U., Antón, L. C., Gibbs, J., Norbury, C. C., Yewdell, J. W., & Bennink, J. R. (2000). Rapid degradation of a large fraction of newly synthesized proteins by proteasomes. *Nature*, *404*(6779), 770–774. https://doi.org/10.1038/35008096

Schuck, P. (2000). Size-distribution analysis of macromolecules by sedimentation velocity ultracentrifugation and Lamm equation modeling. *Biophysical Journal*, *78*(3), 1606–1619. https://doi.org/10.1016/S0006-3495(00)76713-0

Seguin, S. J., Morelli, F. F., Vinet, J., Amore, D., De Biasi, S., Poletti, A., Rubinsztein, D. C., & Carra, S. (2014). Inhibition of autophagy, lysosome and VCP function impairs stress granule assembly. *Cell Death and Differentiation*, *21*(12), 1838–1851. https://doi.org/10.1038/cdd.2014.103

Seidel, K., Vinet, J., den Dunnen, W. F. A., Brunt, E. R., Meister, M., Boncoraglio, A., Zijlstra, M. P., Boddeke, H. W. G. M., Rüb, U., Kampinga, H. H., & Carra, S. (2012). The HSPB8-BAG3 chaperone complex is upregulated in astrocytes in the human brain affected by protein aggregation diseases. *Neuropathology and Applied Neurobiology*, *38*(1), 39–53. https://doi.org/10.1111/j.1365-2990.2011.01198.x

Selcen, D., Muntoni, F., Burton, B. K., Pegoraro, E., Sewry, C., Bite, A. V., & Engel, A. G. (2009). Mutation in BAG3 causes severe dominant childhood muscular dystrophy. *Annals of Neurology*, *65*(1), 83–89. https://doi.org/10.1002/ana.21553

Semmler, A. L., Sacconi, S., Bach, J. E., Liebe, C., Bürmann, J., Kley, R. A., Ferbert, A., Anderheiden, R., Van Den Bergh, P., Martin, J. J., De Jonghe, P., Neuen-Jacob, E., Müller, O., Deschauer, M., Bergmann, M., Schröder, J. M., Vorgerd, M., … Claeys, K. G. (2014). Unusual multisystemic involvement and a novel BAG3 mutation revealed by NGS screening in a large cohort of myofibrillar myopathies. *Orphanet Journal of Rare Diseases*, *9*(1). https://doi.org/10.1186/s13023-014-0121-9

Shaid, S., Brandts, C. H., Serve, H., & Dikic, I. (2013). Ubiquitination and selective autophagy. *Cell Death and Differentiation*, *20*(1), 21–30. https://doi.org/10.1038/cdd.2012.72

Shemetov, A. A., & Gusev, N. B. (2011). Biochemical characterization of small heat shock protein HspB8 (Hsp22)-Bag3 interaction. *Archives of Biochemistry and Biophysics*, *513*(1), 1–9. https://doi.org/10.1016/j.abb.2011.06.014

Shemetov, A. A., Seit-Nebi, A. S., Bukach, O. V., & Gusev, N. B. (2008a). Phosphorylation by cyclic AMP-dependent protein kinase inhibits chaperone-like activity of human HSP22 in vitro. *Biochemistry (Moscow)*, *73*(2), 200–208. https://doi.org/10.1007/s10541-008-2012-y

Shemetov, A. A., Seit-Nebi, A. S., & Gusev, N. B. (2008b). Structure, properties, and functions of the human small heat-shock protein HSP22 (HspB8, H11, E2IG1): A critical review. *Journal of Neuroscience Research*, *86*(2), 264–269. https://doi.org/10.1002/jnr.21441

Shemetov, A. A., Seit-Nebi, A. S., & Gusev, N. B. (2011). Phosphorylation of human small heat shock protein HspB8 (Hsp22) by ERK1 protein kinase. *Molecular and Cellular Biochemistry*, *355*(1–2), 47–55. https://doi.org/10.1007/s11010-011-0837-y

Shy, M., Rebelo, A. P., Feely, S. M., Abreu, L. A., Tao, F., Swenson, A., Bacon, C., & Zuchner, S. (2017). *Mutations in BAG3 cause adult- onset Charcot-Marie-Tooth disease*. *0*(0), 1–5.

Sondermann, H., Scheufler, C., & Schneider, C. (2001). Structure of a Bag / Hsc70 Complex : Convergent Functional Evolution of Hsp70 Nucleotide Exchange Factors. *Science*, *291*(2001), 1553–1558. https://doi.org/10.1126/science.1057268

Sousa, R., & Lafer, E. M. (2015). The role of molecular chaperones in clathrin mediated vesicular trafficking. *Frontiers in Molecular Biosciences*, *2*(May). https://doi.org/10.3389/fmolb.2015.00026

Stark, H. (2010). GraFix: Stabilization of fragile macromolecular complexes for single particle Cryo-EM. In *Methods in Enzymology* (1st ed., Vol. 481). https://doi.org/10.1016/S0076-6879(10)81005-5

Stricher, F., Macri, C., Ruff, M., & Muller, S. (2013). HSPA8/HSC70 chaperone protein: Structure, function, and chemical targeting. *Autophagy*, *9*(12), 1937–1954. https://doi.org/10.4161/auto.26448

Studier, F. W. (2005). Protein production by auto-induction in high density shaking cultures. *Protein Expression and Purification*, *41*(1), 207–234. https://doi.org/10.1016/j.pep.2005.01.016

Sugita, Y., Matsunami, H., Kawaoka, Y., Noda, T., & Wolf, M. (2018). Cryo-EM structure of the Ebola virus nucleoprotein–RNA complex at 3.6 Å resolution. *Nature*. https://doi.org/10.1038/s41586-018-0630-0

Sun, X., Fontaine, J. M., Rest, J. S., Shelden, E. A., Welsh, M. J., & Benndorf, R. (2004). Interaction of Human HSP22 (HSPB8) with Other Small Heat Shock Proteins. *Journal of Biological Chemistry*, *279*(4), 2394–2402. https://doi.org/10.1074/jbc.M311324200

Tang, B. S., Zhao, G. hua, Luo, W., Xia, K., Cai, F., Pan, Q., Zhang, R. xu, Zhang, F. feng, Liu, X. min, Chen, B., Zhang, C., Shen, L., Jiang, H., Long, Z. gao, & Dai, H. ping. (2005). Small heat-shock protein 22 mutated in autosomal dominant Charcot-Marie-Tooth disease type 2L. *Human Genetics*, *116*(3), 222–224. https://doi.org/10.1007/s00439-004-1218-3

Tang, G., Peng, L., Baldwin, P. R., Mann, D. S., Jiang, W., Rees, I., & Ludtke, S. J. (2007). EMAN2: An extensible image processing suite for electron microscopy. *Journal of Structural Biology*, *157*(1), 38–46. https://doi.org/10.1016/j.jsb.2006.05.009

Thompson, A. D., Bernard, S. M., Skiniotis, G., & Gestwicki, J. E. (2012). Visualization and functional analysis of the oligomeric states of Escherichia coli heat shock protein 70 (Hsp70/DnaK). *Cell Stress and Chaperones*, *17*(3), 313–327. https://doi.org/10.1007/s12192-011-0307-1

Trurnit, H. J. (1960). A theory and method for the spreading of protein monolayers. *Journal of Colloid Science*, *15*(1), 1–13. https://doi.org/10.1016/0095-8522(60)90002-7

Ulbricht, A., Eppler, F. J., Tapia, V. E., Van Der Ven, P. F. M., Hampe, N., Hersch, N., Vakeel, P., Stadel, D., Haas, A., Saftig, P., Behrends, C., Fürst, D. O., Volkmer, R., Hoffmann, B., Kolanus, W., & Höhfeld, J. (2013). Cellular mechanotransduction relies on tension-induced and chaperone-assisted autophagy. *Current Biology*, *23*(5), 430–435. https://doi.org/10.1016/j.cub.2013.01.064

Ulbricht, A., Gehlert, S., Leciejewski, B., Schiffer, T., Bloch, W., & Höhfeld, J. (2015). Induction and adaptation of chaperone-assisted selective autophagy CASA in response to resistance exercise in human skeletal muscle. *Autophagy*, *11*(3), 538–546. https://doi.org/10.1080/15548627.2015.1017186

Uytterhoeven, V., Lauwers, E., Maes, I., Miskiewicz, K., Melo, M. N., Swerts, J., Kuenen, S., Wittocx, R., Corthout, N., Marrink, S. J., Munck, S., & Verstreken, P. (2015). Hsc70-4 Deforms Membranes to Promote Synaptic Protein Turnover by Endosomal Microautophagy. *Neuron*, *88*(4), 735–748. https://doi.org/10.1016/j.neuron.2015.10.012

Varlet, A. A., Fuchs, M., Luthold, C., Lambert, H., Landry, J., & Lavoie, J. N. (2017). Fine-tuning of actin dynamics by the HSPB8-BAG3 chaperone complex facilitates cytokinesis and contributes to its impact on cell division. *Cell Stress and Chaperones*, *22*(4), 553–567. https://doi.org/10.1007/s12192-017-0780-2

Waterhouse, A., Bertoni, M., Bienert, S., Studer, G., Tauriello, G., Gumienny, R., Heer, F. T., De Beer, T. A. P., Rempfer, C., Bordoli, L., Lepore, R., & Schwede, T. (2018). SWISS-MODEL: Homology modelling of protein structures and complexes. *Nucleic Acids Research*, *46*(W1), W296–W303. https://doi.org/10.1093/nar/gky427

Wegele, H., Müller, L., & Buchner, J. (2004). Hsp70 and Hsp90--a relay team for protein folding. *Reviews of Physiology, Biochemistry and Pharmacology*, *151*(January), 1–44. https://doi.org/10.1007/s10254-003-0021-1

Wu, S., Avila-sakar, A., Kim, J., Booth, D. S., Greenberg, C. H., Rossi, A., Liao, M., Li, X., Alian, A., Griner, S. L., Juge, N., Yu, Y., Mergel, C. M., Edwards, R. H., Stroud, R. M., Craik, C. S., Chaparro-riggers, J., … Tampe, R. (2012). *Fabs Enable Single Particle cryoEM Studies of Small Proteins*. 582–592. https://doi.org/10.1016/j.str.2012.02.017

Xu, Z., Graham, K., Foote, M., Liang, F., Rizkallah, R., Hurt, M., Wang, Y., Wu, Y., & Zhou, Y. (2013). 14-3-3 Protein Targets Misfolded Chaperone-Associated Proteins To Aggresomes. *Journal of Cell Science*, *126*(18), 4173–4186. https://doi.org/10.1242/jcs.126102

Xu, Z., Page, R. C., Gomes, M. M., Kohli, E., Nix, J. C., Herr, A. B., Patterson, C., & Misra, S. (2008). Structural basis of nucleotide exchange and client binding by the Hsp70 cochaperone Bag2. *Nature Structural & Molecular Biology*, *15*(12), 1309–1317. https://doi.org/10.1038/nsmb.1518

Yewdell, J. (2002). To DRiP or not to DRiP: generating peptide ligands for MHC class I molecules from biosynthesized proteins. *Molecular Immunology*, *39*(3–4), 139–146. https://doi.org/10.1016/S0161-5890(02)00097-4

Zhang, H., Amick, J., Chakravarti, R., Santarriaga, S., Schlanger, S., McGlone, C., Dare, M., Nix, J. C., Scaglione, K. M., Stuehr, D. J., Misra, S., & Page, R. C. (2015). A Bipartite Interaction between Hsp70 and CHIP Regulates Ubiquitination of Chaperoned Client Proteins. *Structure*, *23*(3), 472–482. https://doi.org/10.1016/j.str.2015.01.003

Zhang, K. (2016). Gctf: Real-time CTF determination and correction. *Journal of Structural Biology*, *193*(1), 1–12. https://doi.org/10.1016/j.jsb.2015.11.003

Zhang, X., & Qian, S. B. (2011). Chaperone-mediated hierarchical control in targeting misfolded proteins to aggresomes. *Mol Biol Cell*, *22*(18), 3277–3288. https://doi.org/10.1091/mbc.E11-05-0388

Zhao, J., Benlekbir, S., & Rubinstein, J. (2015). Electron cryomicroscopy observation of rotational states in a eukaryotic V-ATPase. *Nature*, *521*(7551), 241–245.

https://doi.org/10.1038/nature14365

Zheng, S. Q., Palovcak, E., Armache, J.-P., Verba, K. A., Cheng, Y., & Agard, D. A. (2017). MotionCor2: anisotropic correction of beam-induced motion for improved cryo-electron microscopy. *Nature Methods*, *14*(4). https://doi.org/10.1038/nmeth.4193

Zuiderweg, E. R. P., Hightower, L. E., & Gestwicki, J. E. (2017). The remarkable multivalency of the Hsp70 chaperones. *Cell Stress and Chaperones*, *22*(2), 173–189. https://doi.org/10.1007/s12192-017-0776-y

ANNEXES

ANNEXES

- Publication:

Fernández-Fernández, M. R., **Gragera, M.**, Ochoa-Ibarrola, L., Quintana-Gallardo, L., & Valpuesta, J. M. (2017). Hsp70 - a master regulator in protein degradation. *FEBS Letters*, *591*, 2648–2660. **https://doi.org/10.1002/1873-3468.12751**